UNIVERSITÀ DEGLI STUDI DI TORINO

SCUOLA DI DOTTORATO

DOTTORATO IN
SCIENZE AGRARIE, FORESTALI E ALIMENTARI

CICLO: XXXV

WILDFIRE IMPACTS ON SOILS: INTERACTION BETWEEN MINERAL AND ORGANIC PHASES

Sara Negri

Docente guida:
Prof.ssa Eleonora Bonifacio

Coordinatore del Ciclo:
Prof.ssa Eleonora Bonifacio

ANNI
2020; 2021; 2022

CONTENTS

CHAPTER 1

Introduction

1.1 Wildfire-affected soils: a general framework

Wildfires are recognized as fundamental ecosystem shapers (Pickett and White, 2013), which have been impacting landscapes worldwide since the late Devonian (Glasspool et al., 2015). They cause the redistribution of light and nutrients by altering canopy and litter cover (Mataix-Solera and Cerdà, 2009), and can affect the physical, chemical and biological properties of soils (Neary et al., 1999). The degree of transformations borne by soil properties are mainly dictated by fire-events duration, fuel type (Robichaud, 2000), maximum reached temperature (T), heating rate, O_2 availability (DeBano, 2000), soil and fuel moisture (Badía-Villas et al., 2014; Merino et al., 2018). To mimic the behavior of different fire typologies or intensities on soils, laboratory heating experiments are widely adopted. Both combustion tunnels (Badía-Villas et al., 2014; Merino et al., 2018) and muffle furnaces (Araya et al., 2017) have been extensively used.

Temperatures as high as 300-700 °C have been recorded at the soil surface for burning of shrubland vegetation (Gimeno-García et al ., 2004). In forest fires, the extent of soil heating can vary depending on the severity of the event, with Ts below 250 °C (low severity), around 450 °C (moderate severity) or up to 650 °C (high severity fires) (Janzen and Tobin-Janzen, 2008). Typically, only the topsoil experiences consistent heat transfer due to the low thermal conductivity of the soil matrix (DeBano et al., 1998; Hartford and Frandsen, 1992). Ts rarely exceed 100 °C below the first 2 cm (Badía-Villas et al., 2014; Humphreys, 1981) or 5 cm (Merino et al., 2018) from the soil surface and, still, areas affected by the impacts of fires can be extremely vast.

1.2 Soil organic matter transformations

Intense heating can induce relevant changes in soil **organic carbon** (OC) content and **organic matter** (OM) composition (Knicker, 2011; Merino et al., 2018). The biochemical composition of soil OM starts undergoing significant transformations at 150-200 °C (Merino et al., 2018). A decrease in carbohydrates, O-alkyl and alkyl compounds occurs in parallel with an enrichment in the aromatic domain (Knicker et al., 2008). Aliphatic hydrocarbons transform into polycyclic aromatic hydrocarbons (PAH) (Knicker, 2011), with increasing aromaticity at increasing heat severity (Baldock and Smernik, 2002; Santín et al., 2016), in dependence of starting OM composition (González-Pérez et al., 2004; Hilscher et al., 2009). Lipids experience breakdown of long (odd-numbered) chains, with production of smaller-sized alkanes ($<C_{25}$) and fatty acids ($<C_{20}$) (González-Pérez et al., 2008). The fragmentation can be severe also in case of alkenes (Badía-Villas et al., 2014). Lignin residues, highly resistant towards thermal oxidation, are

usually affected only with Ts above 450 °C (Sharma et al., 2004) and, yet, charring at 350 °C was found to induce the loss of O-alkyl C, with dehydroxylation reactions and cleavage of aryl ethers (Knicker et al., 2008).
Partly-combusted OM, often referred to as pyrogenic carbon (PyC) (Abney et al., 2019; DeLuca et al., 2020), comprises charred organic compounds highly resistant towards microbial degradation (Singh et al., 2014). This OM pool can contribute to C sequestration in soils (Knicker, 2007) and its presence may alter the source-sink functioning of various ecosystems (Santín et al., 2016).
Other than partial combustion, increasing heating can trigger intense OM volatilization (Knicker et al., 2006) and, as a widely accepted notion, pH increase is often observed in fire affected soils as a consequence of OM oxidation and base-cations release (Glaser et al., 2002). Some scientists consider fire-induced OM mineralization (by direct combustion) and indirect losses by after-fire erosion dynamics as one of the dominant mechanisms inducing OC losses on the surface of the Earth (Schmidt et al., 2011). A remarkable decrease in OC content has frequently been reported in burnt superficial soil horizons (Mataix-Solera et al., 2002) for Ts greater than 200-250 °C (Badìa and Martì, 2003; Santín and Doerr, 2016) and, notwithstanding the time of exposure, consistent OM oxidation is expected for Ts equal or higher than 300 °C (Merino et al., 2018). However, literature does not always agree on the decrease of soil OC as a consequence of fire. New C inputs may derive from necromass incorporation, with deposition of new (and partly charred) material from the above-ground vegetation (González-Pérez et al., 2004; Johnson and Curtis, 2001). Furthermore, as some have righteously pointed out (Mastrolonardo et al., 2015), an improper soil sampling may lead to inconsistency in determination.

1.3 Heat effects on soil minerals

Aside from modifications in OM, fires and heating treatments have also been documented to alter soil **mineralogy** (Araya et al., 2016; Reynard-Callanan et al., 2010). The collapse of kaolinite has largely been observed with temperatures higher than 550 °C due to the loss of hydroxyl groups (Burton et al., 2019; Ulery et al., 1996). The decomposition of minerals like chlorite and chlorite-vermiculite has also been reported at similar heat-intensities (Reynard-Callanan et al., 2010; Ulery et al., 1996), while the structure of gibbsite can be affected already at 200 °C (Rooksby, 1972). For low-moderate fire-induced heating, significant thermal alterations can also occur to soil iron (Fe) oxyhydroxides (hereafter referred to as Fe oxides) (Koch et al., 2005; Norouzi and Ramezanpour, 2013).
The most widespread **Fe oxides** include pedogenic ferrihydrite ($Fe_{10}O_{14}(OH)_2$), goethite (α-FeOOH), lepidocrocite (γ-FeOOH) and hematite (α-Fe_2O_3), while pedogenic maghemite (γ-Fe_2O_3) and its lithogenic precursor magnetite (Fe_3O_4) can also locally occur (Schwertmann, 1988). Thermal alteration of isolated soil Fe oxides has been studied since the 80s, revealing a multiplicity of possible speciation dynamics according to composition, grain size and morphology of the starting mineral particles or, conversely, the convergence of many Fe phases

to the same final product. For example, engineered mineral mixtures of ferrihydrite and goethite experienced minor changes until 200 °C (Johnston et al., 2019), with transition to maghemite at 400 °C (Cornell and Schwertmann, 2003). Magnetite formation, on the other hand, has been documented upon heating of lepidocrocite, hematite or ferrihydrite (Cornell and Schwertmann, 2003), with diffusion of Fe(II) and Fe(III) ions within the oxygen sub-lattice and electron transfer between iron ions of different valence (Hyeon et al., 2001). Mineralogy in heat/fire-impacted soils has gained much attention as a promising marker of soil burn severity, since wildfire-affected areas have been found to display a notable enhancement in surface magnetism (Löhr et al., 2017). Still, the nature of this phenomenon is debated. Some authors explain it as a heat-mediated increase in low-coercitivity components (Clement et al., 2011), while others attribute it mainly to a combustion-induced mass-loss effect (with concentration of magnetic phases rather than neo-formation of magnetic minerals) (Jordanova et al., 2019; Till et al., 2021).

The uncertainty related to Fe speciation dynamics in fire-affected soils is favored by the complex nature of these systems, where pedogenic Fe oxides of multiple crystalline degrees appear in association with a wide spectrum of organic compounds and mineral phases. To study them, specific Fe pools are generally isolated by selective extractions (Campbell and Schwertmann, 1984), while scanning electron and transmission electron microscopy (SEM and TEM) are used to observe crystal habitus and dimensions of iron particles (LaGrow et al., 2019). X-ray diffraction (XRD) is applied for phase identification and assessment of metal substitution degree (Brindley and Brown, 1980). Sample purity and Fe nano crystals size can be inspected by exposing soil samples to a cycling magnetic field (Coey, 1988). Raman and Mössbauer spectroscopy have been respectively applied for identification of Fe species and determination of coordination form (De Faria et al., 1997; De Grave et al., 2002). Synchrotron-light based X-ray absorption spectroscopy (XAS) can be used to assess oxidation state, local bonding environment and electronic structure of atoms (Espinosa et al., 2011; Kawai, 2010), and has allowed to perform identification of Fe species and associated OM even in matrixes as inhomogeneous as soils (Giannetta et al., 2022).

Without the employment of multiple techniques, the small variations induced in Fe species by a moderate heating treatment (corresponding to the Ts realistically triggered by forest fires) are likely to go unnoticed.

1.4 Changes in soil physical properties: water repellency and aggregation

Consistent fire-induced heating can impact soil **physical properties,** like aggregate size and stability (Andreu et al., 2001; Mataix-Solera et al., 2011) and soil water repellency (WR) (Varela et al., 2010). As a consequence, wildfires can be followed by runoff, high erosion yields, sediment transfer and nutrients depletion (Certini, 2005; Moody et al., 2013; Varela et al., 2010), primarily depending on topography (Smith et al., 2011), frequency and severity of the disturbance (Shakesby and Doerr, 2006).

The loss of the protective litter layer and organic horizon, and the detrimental effects on soil structure, might be mitigated by the presence of a char and ash layer at the soil level (Vega et al., 2014). Due to high Ts, a decrease in microbial biomass is expected in fire-affected areas (Mataix-Solera et al., 2011), especially in severely burnt stands (Fernández-García et al., 2019), also with remarkable changes in the structure of soil microbial communities (Greene et al., 2010; Treseder et al., 2014) and detectable modifications in ectomycorrhizal-fungi composition even years after fire passage (Kipfer et al., 2011; Orumaa et al., 2022).

Water repellent soils are characterized by a limited water infiltration capacity, and may be so even at their natural state (unheated condition) (Bisdom et al., 1993). Water infiltration occurs when the cohesive forces present within a water drop are overcome by the adhesive forces between the water molecules and the soil surface (Parker, 1987). When this condition is met, the contact angle (CA) of the liquid phase (internal to the water drop, between the air surrounding the drop itself and the planar soil surface) becomes equal to or lower than 90° (Letey, 1969).

Soil **water repellency** (WR) can be evaluated with multiple methods, in addition to CA direct measurement. Among them, the Water Drop Penetration Time (WDPT) test is appreciated for its simplicity and straightforwardness. This method requires the placement of a water drop onto the soil flattened surface, and the recording of the time needed for the drop to penetrate into the soil (Letey, 1969). WDPT has been considered as a metric of persistence of WR, rather than as an estimation of the actual degree of hydrophobicity itself (Diehl, 2013). To be consistent, this analysis should be carried out at constant relative humidity and room temperature (RT) (Bisdom et al., 1993), using multiple water drops of the same size (Diehl, 2013; Papierowska et al., 2018). A widely adopted alternative to WDPT is the molarity of an ethanol droplet (MED) test, also addressed as ethanol percentage (EP) test (Badía et al., 2013). This analysis consists in the application different solutions (with increasing ethanol:water concentrations) to the soil surface, until when drop penetration occurs within 3 s (Doerr, 1998).

The extent of soil WR depends primarily on OM content and composition (Arcenegui et al., 2008). For example, amphiphilic compounds, if present, can cluster as micelle (Wandruszka et al., 1999) and, while hydrophilic heads are bound to mineral hydroxylated surfaces by means of ligand-exchange reactions, hydrophobic moieties are exposed to the exterior, shielding the inner region from direct contact with water molecules (Tiberg et al., 1999). Soil hydrophobicity can increase as a consequence of heating (Malkinson and Wittenberg, 2011), as testified by the extreme WR displayed by soils experiencing high-severity wildfires (Ferreira et al., 2005) or in laboratory heating experiments (Atanassova and Doerr, 2011). In heated soils, incomplete OM combustion leads to the volatilization of hydrophobic substances (Shakesby and Doerr, 2006; Zavala et al., 2010) that may condense as coatings on mineral particles, boosting WR (DeBano, 2000). The characteristics of the mineral

phase are then also fundamental in determining soil WR as, for once, coarse-textured soils experience a more efficient OM coating (Scott, 2000). A high WR can arise also in clay-rich soils, if OM loads are sufficient to cover the greater surface of smaller-sized particles (Doerr et al., 2000, 1996). In heated soils, the thermal-induced cementation of small aggregates into bigger ones may also trigger an increase in WR (Bisdom et al., 1993).

The degree of soil WR is associated to the presence of certain minerals. Kaolinite has been deemed as an inhibitor of WR (Mataix-Solera et al., 2008), likely because of the presence of the hydrophilic octahedral sheet (**Figure 1.1**) (Šolc et al., 2011). Soil Fe oxides of great surface area, such as ferrihydrite (Cornell and Schwertmann, 2003), could directly trigger either a higher or lower wettability depending on the balance between the large surface area and the high affinity for OM sorption (Newcomb et al., 2017).

In heated soils, the relationship between rising Ts and WR is not linear. Over a certain threshold, identified at 280-400 °C (Doerr et al., 2005), 270-300 °C (Atanassova and Doerr, 2011; García-Corona et al., 2004; Zavala et al., 2010) or at 225 °C (after 5 h heating) (Simkovic et al., 2008), WR is lost. The high-T loss of hydrophobicity is explained with the destruction of the organic compounds responsible for the coating of mineral surfaces (DeBano, 2000). Still, as these coatings have not been univocally observed, the mechanisms ruling such dynamics are up-to-now widely obscure.

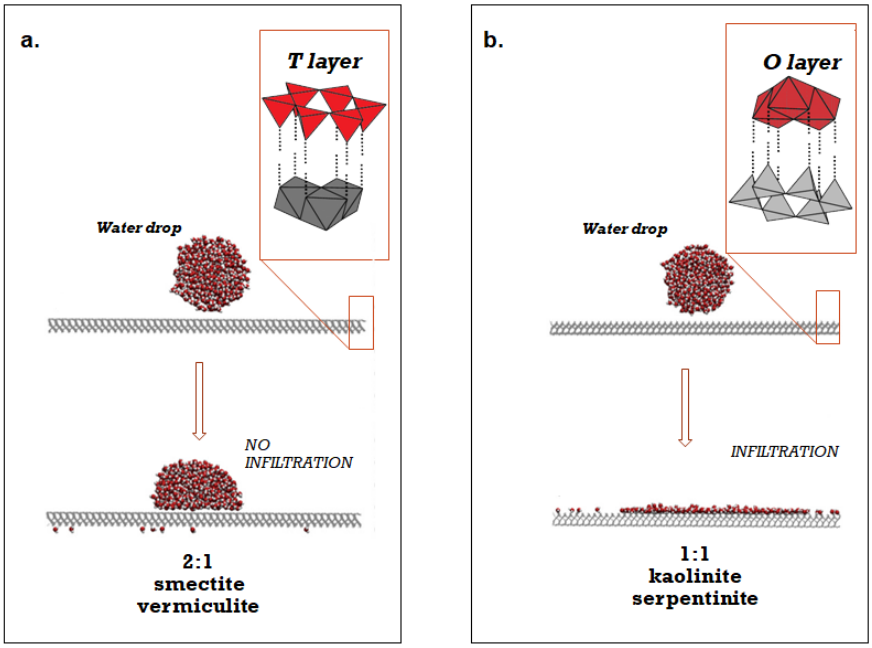

Figure 1.1: Water drop behaviour according to mineral surface exposed. Modified after Šolc et al. (2011).

Soil **aggregates** are identified as inhomogeneous and autonomous elements of soil structure (Fedotov et al., 2006), recognizable and mechanically separable from adjacent particles (Certini and Ugolini, 2010). Alternatively, aggregation refers to a stable association of individual particles resulting from physico-chemical-biological processes with co-existence of mineral and organic phases (Tisdall and Oades, 1982).

In soil, a wide spectrum of aggregate size-classes exists but, generally, aggregates are divided into micro- (<250 µm) and macro-aggregates (>250 µm). Different methods can be used to assess the distribution of aggregates (Mataix-Solera et al., 2010), and aggregate stability (AS), implying resistance against external forces (Mataix-Solera et al., 2011). The strength of aggregates can be tested by dry or wet sieving, rainfall simulations, drop impacts, or ultrasonic dispersion (Kemper and Koch, 1966; Roldán et al., 1996; Yoder, 1936). Recently, the wet sieving method has been used on macro-aggregates in the range of 1-2 mm (Badía-Villas et al., 2014) and on multiple sieve fractions (0.25-05, 0.5-1, 1-2, 2-4, 4-10 mm) (Girona-García et al., 2018) in the study of fire and heat-affected soils.

Aggregation is a complex phenomenon. Stable-aggregates formation is ruled by factors like concentration and composition of electrolyte in soil solution, with flocculation promoted by cations like Ca, Fe and Al (Porta Casanellas et al.,

1994). Abundance of OM and carbonates (Campo et al., 2008; Tisdall and Oades, 1982), gypsum (Badìa and Martì, 2003), Fe and aluminum (Al) oxides (Amézketa, 1999; Tisdall and Oades, 1982) can increase soil aggregation. In parallel, macro-aggregates formation is favored by roots (Roldán et al., 1996) and fungal iphae (O'dea, 2007), and by the presence of mosses and lichens (Bowker et al., 2004)

Fire and laboratory heating can either cause an increase or a decrease in soil AS (Arcenegui et al., 2008; Badìa and Martì, 2003; García-Corona et al., 2004; Terefe et al., 2008; Zavala et al., 2010), while some studies have reported no variation (Llovet et al., 2009; Mataix-Solera et al., 2002). This non-unique behaviour depends, primarily, on the influence of rising Ts on the main soil binding agents. Some studies have deemed OM as the dominant soil binding factor in many soils (Badía and Martí, 2003; Soto et al., 1991; Zavala et al., 2010), which are then expected to lose cohesiveness at high Ts. At the same time, heat-induced re-crystallization phenomena of Fe-Al oxides and presence of abundant clay contents may alternatively lead to greater AS at higher Ts (Giovannini and Lucchesi, 1997; Guerrero et al., 2001; Mataix-Solera et al., 2011; Terefe et al., 2008).

1.5 Aim and structure of the work

Nowadays, fire regimes are changing due to direct and indirect human actions. Widespread land abandonment has caused shrub encroachment and forest spread in once-populated rural areas (Komac et al., 2013; Mantero et al., 2020), inducing great flammability risks (Caballero et al., 2011). Additionally, climate change is acting at a global scale (Pachauri and Meyer, 2014), leading to an increase in wildfires size, frequency and intensity (Bowman et al., 2009). Projections for future years forecast even more frequent and disruptive events (Jolly et al., 2015).

In the Mediterranean basin, after-fire dynamics are widely studied in areas characterized by a Mediterranean climate (Arcenegui et al., 2008; Badìa and Martì, 2003; Girona-García et al., 2018; Mataix-Solera et al., 2008; Merino et al., 2018; Varela et al., 2010), where wildfire has been recognized as a dominant factor in shaping the landscape (Keeley et al., 2011). Other extensively studied realities exist in North America (Araya et al., 2017; Santos et al., 2016; Zhang and Biswas, 2017), where 5 Mha of forests are annually affected by fires (van Lierop et al., 2015). Yet, soils developed in other biomes might not unequivocally respond to fire-induced heating (Pellegrini et al., 2022). In Italy, research on fire affected areas has been mostly conducted in the Islands (Capra et al., 2018; Mastrolonardo et al., 2013; Tinebra et al., 2019) and in the Southern and Central regions of the Country (Bonanomi et al., 2022; De Marco et al., 2023; Mastrolonardo et al., 2015). The impact of heating on the soils of Northern Italian mountains is vastly unknown, and existing literature usually dealt with after-fire forest regeneration dynamics (Vacchiano et al., 2014) and shifts in soil microbial communities as a result of fire occurrence (Kipfer et al., 2011). Yet, these soils belong to an ecological region that has

recently suffered from uncommonly disruptive fire seasons (Bovio, 2011; Rita et al., 2020). Steep slopes and exposure to large precipitation events might exacerbate the intrinsic fragility of mountain soils, with after-fire loss of physical integrity (Smith et al., 2011).

For all these reasons, in **Chapter 2** we addressed the impacts of an environmentally realistic heating treatment (fire-induced) on soils of the Western Italian Alps, aiming at unveiling the modifications occurring in the physical properties (WR), in OM and in its interaction with the mineral phase. We elucidated the main mechanisms involved in WR occurrence and evolution with increasing Ts. In **Chapter 3**, we focused on the transformations of soil Fe oxides. We systematically addressed Fe speciation pathways as ruled by native Fe species and OM, in a T-range reasonable to mimic fire-induced soil heating. In **Chapter 4**, we assessed the heating response patterns of soils belonging to highly diverse natural forested ecosystems. The alterations occurring in WR and AS have been linked to modifications induced in OM and Fe phases, as changes borne by organic compounds and mineral phases at the nano-scale can reflect into modifications at the macro-scale, impacting entire ecosystems.
The results obtained in this thesis have been the object of several scientific publications.

- Chapter 2:
  Negri S., Stanchi S., Celi L., Bonifacio E. (2021). Simulating wildfires with lab-heating experiments: Drivers and mechanisms of water repellency in alpine soils. Geoderma (402).
- Chapter 3:
  Negri S., Giannetta B., Till J., Said-Pullicino D., Bonifacio E. (2022). Fire simulations effects on the transformation of iron minerals in alpine soils. Geoderma, ***under review***.
- Chapter 4:
  Negri S., Arcenegui V., Giannetta B., Jiménez-Morillo N.T., Zaccone C., Mataix-Solera J., Bonifacio E. (2023). Divergent heating response patterns in soils belonging to various natural ecosystems. ***In preparation***.

CHAPTER 2

Simulating wildfires with lab-heating experiments: drivers and mechanisms of water repellency in alpine soils

2.1 Introduction

Water repellency may be hindered by the presence of kaolinite, as mentioned in the Introduction. This T-O phyllosilicate is common in areas where an intense degree of soil development has occurred. The soils of the Alps are mostly lacking kaolinite and, yet, may contain serpentine, an analogue mineral (1:1 Mg layer silicate) with low surface area and hydrophilic surfaces (Dixon et al., 1989). The occurrence of serpentine is tightly related to the distribution of serpentinite rocks (Legros, 1992). This family of metamorphic rocks is mostly composed of serpentine, with accessory chlorites, talc, olivine, pyroxenes, magnetite and chromite (Moody, 1976).

Alpine soils developing on these rocks are poor in plant nutrients but contain high levels of Fe, Mg and heavy metals like Ni and Cr (D'Amico et al., 2014). Due to the presence of Mg in the octahedral sheet, the hydrophilicity of serpentine could be even higher than that of kaolinite. To clarify whether serpentine can act as a WR inhibitor (wettable tendency) or a booster (low surface area), we collected, heated and characterized a set of soils that presented the typical features of alpine soils in terms of OM and mineralogy.

Thus the aims of this chapter are: i) to elucidate the occurrence and evolution of heating-induced WR in alpine soils, and ii) to unravel the role of soil OM and mineral phases on natural and heating-induced WR.

2.2 Materials and methods

2.2.1 Study area, soil sampling and heating treatment

The study was conducted on a set of soils collected in two neighboring valleys located in Piedmont, North-Western Italy (**Figure 2.1**) at elevations ranging from 1004 to 2037 m a.s.l. The whole area is characterized by a pre-alpine climate with average mean temperatures of about 6 °C, and annual precipitation that used to be 800 mm (IPLA, 2001; IPLA, 2000). A shift towards drier conditions was however observed by averaging the mean monthly climatic data of the last twenty years, with 630 mm of annual precipitation (http://webgis.arpa.piemonte.it/geoportale/).

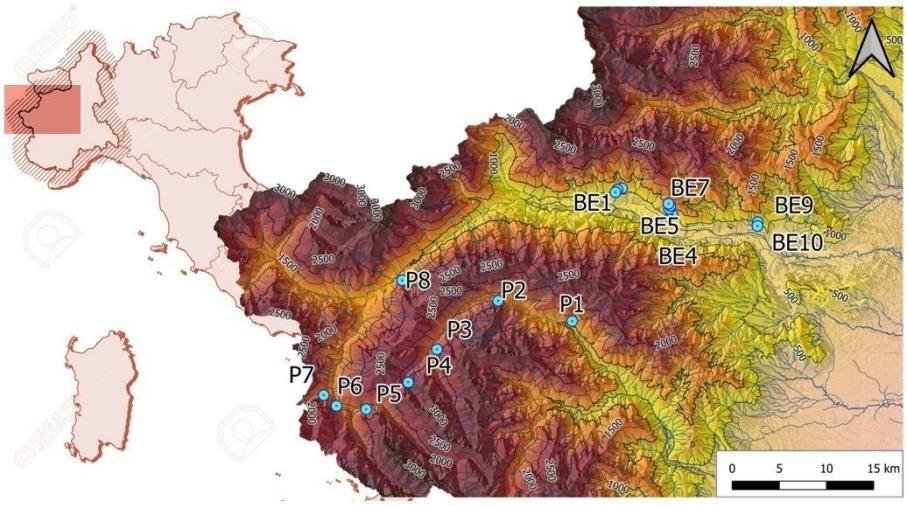

Figure 2.1: Localization of sampling points.

Both valleys belong to the geological Complex of Schists and Green stones, with the presence of different lithological formations like ophiolitic outcrops (amphibolites and serpentinites), calcschists and acid metamorphic rocks (micaceous schists and gneiss) (Servizio Geologico d'Italia, 2009). The samples were collected below two dominant forest types: European beech (BE series, 10 samples) and Scots pine (PI series, 8 samples) (**Table 2.1**). Soils of this area are mostly little developed and can thus be classified as Colluvic Regosols and Skeletic Cambisols, according to the WRB (IUSS Working Group WRB, 2014). The sampling sites were chosen to specifically fall in areas that did not experience burning in the last 10 years.

Table 2.1: Main site characteristics of the selected soils. X and Y coordinates are in ED50/UTM Zone 32N format.

ID	X	Y	Elevation (m a.s.l.)	Forest type	Forest structure and cover	Dominant lithology
BE1	355856	5000989	1310	*Fagus sylvatica* L.	Coppice, presence of *Pinus sylvestris* L.	Gneiss
BE2	356071	5001254	1300	*Fagus sylvatica* L.	High forest, presence of *Pinus sylvestris* L. and *Betula pendula* Roth.	Serpentinite

BE3	356552	5001406	1100	*Fagus sylvatica* L.	High forest	Micaschist
BE4	361810	4998612	1350	*Fagus sylvatica* L.	Coppice, mixed with other broadleaves	Micaschist
BE5	361898	4998600	1350	*Fagus sylvatica* L.	Coppice, mixed with other broadleaves	Micaschist
BE6	361557	4999206	1180	*Fagus sylvatica* L.	Coppice	Serpentinite
BE7	361481	4999762	1250	*Fagus sylvatica* L.	Coppice, mixed with other broadleaves	Serpentinite
BE8	361671	4999535	1300	*Fagus sylvatica* L.	High Forest	Chloritoidschist
BE9	370948	4997803	1300	*Fagus sylvatica* L.	Coppice, presence of *Pinus sylvestris* L.	Serpentinite
BE10	370923	4997399	1300	*Fagus sylvatica* L.	High Forest	Serpentinite
PI1	351268	4987287	1004	*Pinus sylvestris* L.	Mixed with *Quercus spp*. and *Castanea sativa* Mill.	Gneiss and metagranite
PI2	343419	4989449	1336	*Pinus sylvestris* L.	Mixed with *Larix decidua* Mill.	Calcschist
PI3	336948	4984292	1570	*Pinus sylvestris* L.	Mixed with *Larix decidua* Mill.	Micaschist
PI4	333889	4980778	2037	*Pinus sylvestris* L.	Mixed with *Larix decidua* Mill.	Mica schist

PI5	329440	4977921	1560	*Pinus sylvestris* L.	Mixed with *Larix decidua* Mill.	Serpentinite
PI6	326280	4978275	1360	*Pinus sylvestris* L.	Pure, sparse	Serpentinite
PI7	324940	4979413	1510	*Pinus sylvestris* L.	Mixed with *Larix decidua* Mill.	Micaschist
PI8	333257	4991623	1031	*Pinus sylvestris* L.	Pure, dense	Colluvium – mixed lithology

Soil sampling was performed by removing litter and organic horizons until the mineral soil surface was exposed, then the upper A horizon was collected. Soil samples were air-dried, sieved (2 mm) and stored at room temperature until laboratory analysis. Each sample was divided into six homogeneous subsamples. Ten g of each subsample were placed in aluminum cups with a base of 20 cm^2, resulting in samples with a thickness of less than 0.5 cm. One cup was kept at room temperature, while each of the others was oven heated for 30 minutes in a furnace equipped with a thermocouple at a specific temperature (T): 100, 150, 200, 250 and 300 °C. A heating time of 30 minutes was selected in accordance with recent studies (Araya et al., 2017, 2016; Varela et al., 2010). Existing literature reported that loss of WR is generally experienced close to 250 °C, therefore we selected such T values in order to mimic low-moderate fire intensities (Janzen and Tobin-Janzen, 2008) and be able to observe changes in WR.

2.2.2 Soil analyses

Soil WR was evaluated by using both the Water Drop Penetration Time (WDPT) and the Sessile drop Contact Angle (CA) determination methods. The former was adopted for unheated and heated samples (at all T) to monitor the persistence of WR, while the latter was employed only in the case of unheated samples to estimate the initial and maximum natural hydrophobicity.

To ensure comparability of results, WDPT was evaluated after keeping the samples in a vacuum chamber for 30 minutes. Room relative humidity was verified to be always around 30-50 % during WDPT testing (Beatty and Smith, 2010; Diehl et al., 2010; Papierowska et al., 2018). We employed a standard 0.1 mL dropper and recorded WDPT up to 4000 s. Ten drops of distilled water were placed on the soil flattened surface in a short interval of time (less than 30 s).

The CA was determined on 2 mm sieved soil samples (Bachmann et al., 2000; Papierowska et al., 2018). The soil was spread over a glass slide, pressed with a 100 g weight for about 5 s, and a drop of water (20 µL) was placed on the soil flattened surface. Measurements were performed in triplicate (Diehl et al., 2010). The placing of the water drops onto the soil surface was recorded with a 25x digital camera and the frame taken at the exact moment of water-soil contact was used for CA measurement. As CA tends to reduce with time (from contact, at time zero, to water penetration into the soil), we considered the maximum observable value (Beatty and Smith, 2010). A semi-automated procedure was implemented for CA determination. Each image was processed with MATLAB 2020a to highlight the boundaries of the drop. The Processing Toolbox was used for edge detection after gray scaling. The images were then imported in ImageJ and the Contact Angle Tool was employed. CA was calculated on the base of the ellipse-derived drop fitting (Diehl and Schaumann, 2007). **Figure 2.2** displays two images of drops set on two different samples, with edge enhancement and ellipse-derived CA.

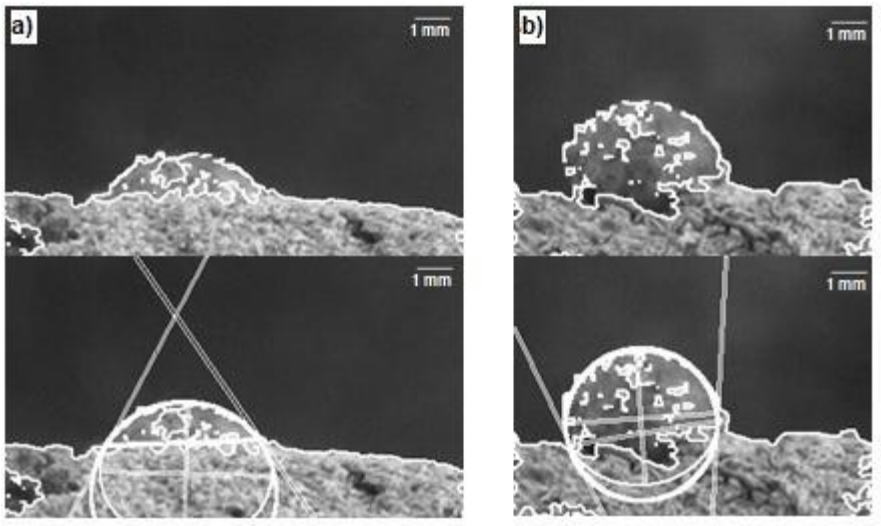

Figure 2.2: Hydrophylic and hydrophobic soil surfaces. a) Soil sample BE6 with ellipse-derived contact angle of 58.90° ; b) Soil sample BE7 with ellipse-derived contact angle of 104.40°.

Soil particle size distribution (PSD) was determined using the pipette method after dispersion with Na-hexametaphosphate (Gee and Bauder, 1986). Size classes were classified as: coarse sand (2000-200 µm), fine sand (200-50 µm), coarse silt (50-20 µm), fine silt (20-2 µm) and clay (<2 µm). Soil pH was evaluated in a 1:2.5 soil:deionized water suspension after 2 h shaking (Gee and Or, 2002). Total C and N were analyzed by dry combustion using a Unicube CHNS Analyzer (Elementar, Langenselbold, Hesse, Germany). Carbonate content was determined volumetrically after HCl treatment (Nelson, 1982) and inorganic C content was subtracted from total C to obtain organic carbon (OC)

content. As a proxy for total serpentine content (Bonifacio et al., 2010), pseudo-total Ni was extracted with concentrated hot HNO3-HCl digestion (Soil Survey Staff, 2014), followed by element determination by atomic absorption spectrometry, AAS (PerkinElmer AAnalyst 400, Norwalk, CT, USA). Total Fe oxides were extracted using a sodium dithionite-citrate-bicarbonate (DCB) solution (Mehra and Jackson, 1960) and Fe content was determined by AAS. Specific Surface Area (SSA, m^2 g^{-1}) was quantified by performing the methylene blue stain test (Chiappone et al., 2004).

Clay was separated by sedimentation after dispersion with Na-hexametaphosphate, flocculated with $MgCl_2$, washed until free of chloride and freeze-dried. The abundance of serpentine was assessed on air-dried oriented mounts by X-ray diffraction (XRD), using a Philips PW 1710 diffractometer (40 kV, 20 mA, CoKα radiation and graphite monochromator). Scans were made from 3 to 35° 2θ at a speed of 1° 2θ min^{-1}, the background was subtracted and the peak intensities and positions were obtained using PowderX software. An index of abundance of serpentine (SRPH, from 0 to 1) was obtained as the ratio of the height of the 001 serpentine peak at 0.73 nm to the sum of the heights of all identified layer silicates, as fully described elsewhere (Bonifacio et al., 2010).

The determination of pH, OC, N were performed not only at room temperature, but also on lab heated samples at all temperatures.

Soil OM composition of samples BE4, BE10, PI5 and PI7 was investigated by means of Fourier Transform-Infrared (FT-IR) spectroscopy. These samples were selected to represent the variability of the dataset in terms of canopy cover (BE and PI), lithology (BE4 and PI7 on schist, BE 10 and PI5 on serpentinite) and WR behavior. Potassium bromide (KBr) pellets were prepared by adding 4 mg of soil sample to 400 mg of KBr, thoroughly ground and mixed. KBr was oven-dried prior to use so as to avoid water absorption. FT-IR spectra were acquired (PerkinElmer Spectrum 100, Norwalk, CT, USA) in the 4000–450 cm^{-1} region, with a resolution of 4 cm^{-1}. Sixteen scans per sample were obtained, with KBr pellet as background. PerkinElmer IR WinLab Spectrum software was used to process the spectra, performing baseline correction and normalization. The same software was also employed to perform semi-quantitative analysis, calculating the intensity and area corresponding to some selected bands.

2.2.3 Statistical analyses

RStudio (R version 4.0.2) was used for all the statistical analyses. Normality and homoscedasticity of the data were checked before comparisons between groups by, respectively, Shapiro-Wilk's and Levene's tests. Non-normal data were log-scaled. One-way ANOVA was used to detect differences in mean values between groups, setting the threshold for statistical significance at the level of 0.05. Tukey-HSD test was applied for post hoc pairwise comparisons.

Linear mixed models (LMM) were implemented when investigating trends, so as to verify the role played by selected covariates along a T-controlled kinetic (25-300 °C). Autocorrelation, when present, was considered within the model structure and the best fitting model was chosen on the basis of Akaike's information criterion (AIC). Correlation matrices were computed with the use of the non-parametric rank-based Spearman method as part of the data was non-linear. Clustering was operated by building an Euclidean distance matrix, selecting Ward's agglomeration method and then performing dendrogram pruning. The validity of the parameters related to height (y-axis) and number of desired clusters was verified by the application of PERMANOVA test to the obtained clusters. When a p-value lower than 0.05 was obtained, the clustering was assumed as optimal. Principal Component Analysis (PCA) was applied to investigate the relationship between relevant variables. Matrices adopted for PCA were scaled and centered prior to performing the analysis and generating biplots.

2.3 Results

2.3.1 Soil properties at natural state and WR

All samples fell in the textural classes of loamy sand and sandy loam soils, with a mean total sand content of 71 % (st. dev=6 %) (**Table 2.2**). Coarse sand (mean=45 %, st. dev=10 %) always prevailed over fine sand (mean=26 %, st. dev=9 %). The abundance of coarse fractions was reflected by relatively low SSA values (mean=11.7 m^2 g^{-1}, st. dev=5.8 m^2 g^{-1}). Only one sample (PI7) displayed SSA values over 20 m^2 g^{-1}, probably due to its higher clay content. SSA resulted slightly but significantly correlated with clay ($R=0.501$, $p<0.05$), OC ($R=0.540$, $p<0.05$) and N ($R=0.640$, $p<0.01$) contents. The horizons of the BE series were generally characterized by a greater acidity ($p<0.001$) than the soils of the PI subset. Nickel content and SRPH were consistent and in agreement ($R=0.659$, $p<0.05$) in highlighting those horizons with opposite bedrock-derived nature, despite Ni contents were not homogeneously distributed among the samples. The PI subset, in fact, presented overall lower Ni values with respect to the BE series ($p<0.05$), probably due to a lithological inheritance. Nevertheless, samples BE2, BE6, BE7, BE9, BE10, PI5 and PI6 presented extremely high SRPH values and considerable Ni contents and could be unequivocally addressed as serpentine-dominated soils. OC and N values were lower in BE samples with respect to PI samples ($p<0.01$ and $p<0.05$, respectively). The lowest OC contents were found in samples BE5 and BE6 (less than 20 g kg^{-1} OC). C/N ratio was slightly, but not significantly, higher in the PI series with respect to the BE series. DCB-extractable Fe (mean=15.2 g kg^{-1}, st. dev=4.9 g kg^{-1}) was overall but not significantly ($p>0.05$) higher in the BE subset.

Table 2.2: Main soil properties of the analyzed soil samples. Letters for statistically significant mean values (group series, BE vs PI) are reported below.

ID	C. Sand (%)	F. Sand (%)	C. Silt(%)	F. Silt (%)	Clay (%)	SSA (m^2g^{-1})	SRPH	pH	OC ($g\ kg^{-1}$)	N ($g\ kg^{-1}$)	C/N	Ni ($mg\ kg^{-1}$)	Fe DCB ($g\ kg^{-1}$)
BE1	42	26	12	16	4	5.9	0.12	4.4	40.5	2.8	14.5	560	16.5
BE2	43	34	8	12	3	11.8	0.52	4.8	34.7	2.3	15.1	1468	16.6
BE3	26	44	9	17	5	8.0	0.24	6.8	41.2	2.6	15.8	456	19.4
BE4	38	33	11	15	4	9.2	0.13	5.7	31.3	2.8	11.2	258	13.8
BE5	41	36	7	12	5	8.0	0.08	5.1	14.2	1.6	8.9	207	16.4
BE6	40	24	9	21	6	8.4	0.46	6.0	13.2	1.8	7.3	974	17.8
BE7	54	21	7	15	4	5.9	0.63	4.0	42.3	3.7	11.4	1718	21.0
BE8	33	38	14	13	3	19.3	0.17	4.9	42.0	3.4	12.4	358	18.3
BE9	35	29	13	19	4	16.8	0.60	5.5	67.5	4.8	14.1	1285	19.0
BE10	57	17	8	14	3	10.5	0.78	4.5	39.7	3.3	12.0	1704	9.7
PI1	54	23	9	9	5	13.4	0.28	6.6	64.3	4.0	16.1	279	25.6
PI2	50	23	6	16	6	5.0	0.19	7.9	30.9	2.3	13.5	116	9.7
PI3	54	19	9	13	5	15.1	0.14	6.2	97.1	7.0	13.9	96	12.9
PI4	41	22	11	22	5	16.4	0.27	5.9	53.8	4.5	12.0	120	18.2
PI5	59	19	7	11	4	15.5	0.89	6.5	76.2	6.4	11.9	571	10.0
PI6	63	10	5	16	7	14.3	0.57	7.1	54.7	3.4	16.1	583	9.6
PI7	41	18	9	22	10	24.8	0.24	7.1	69.3	5.0	13.9	337	9.1
PI8	41	36	15	7	1	2.1	0.34	7.7	54.2	2.3	23.6	37	9.5
BE mean	41^{b}	30^{a}	10	15	4	10.4	0.37	5.2^{b}	36.7^{b}	2.9^{b}	12.3	899^{a}	16.8
BE std	9	8	2	3	1	4.5	0.25	0.8	15.4	0.9	2.7	605	3.2
PI mean	50^{a}	21^{b}	9	14	5	13.3	0.37	6.9^{a}	62.6^{a}	4.4^{a}	15.1	267^{b}	13.1
PI std	9	7	3	6	2	7.0	0.25	0.7	19.4	1.7	3.8	215	5.9

Figure 2.3 displays the FT-IR spectra at 25 °C of the selected soil samples. The spectra of both BE and PI samples displayed a large band in the 3700-3000 cm^{-1} region mainly due to O-H/N-H stretching of OM compounds, although also O-H from hydration water and octahedral layer of serpentine can contribute to the intensity of that band, especially close to 3700-3600 cm^{-1} (Russell, 1987). C-H stretching of aliphatic compounds (2940 cm^{-1}) was little visible and did not vary much among the samples. In the 1650-1500 cm^{-1} region, the most pronounced

bands due to C-C stretching of aromatic structures were observed in soils of the PI series. This mirrors the difference in OM composition that distinguishes the two forest cover types (tree species). The large band observed in the 1000 cm^{-1} region (lowest in BE10), generally attributed to C-O stretching of alcoholic groups, is here masked by Si-O and Me-O groups.

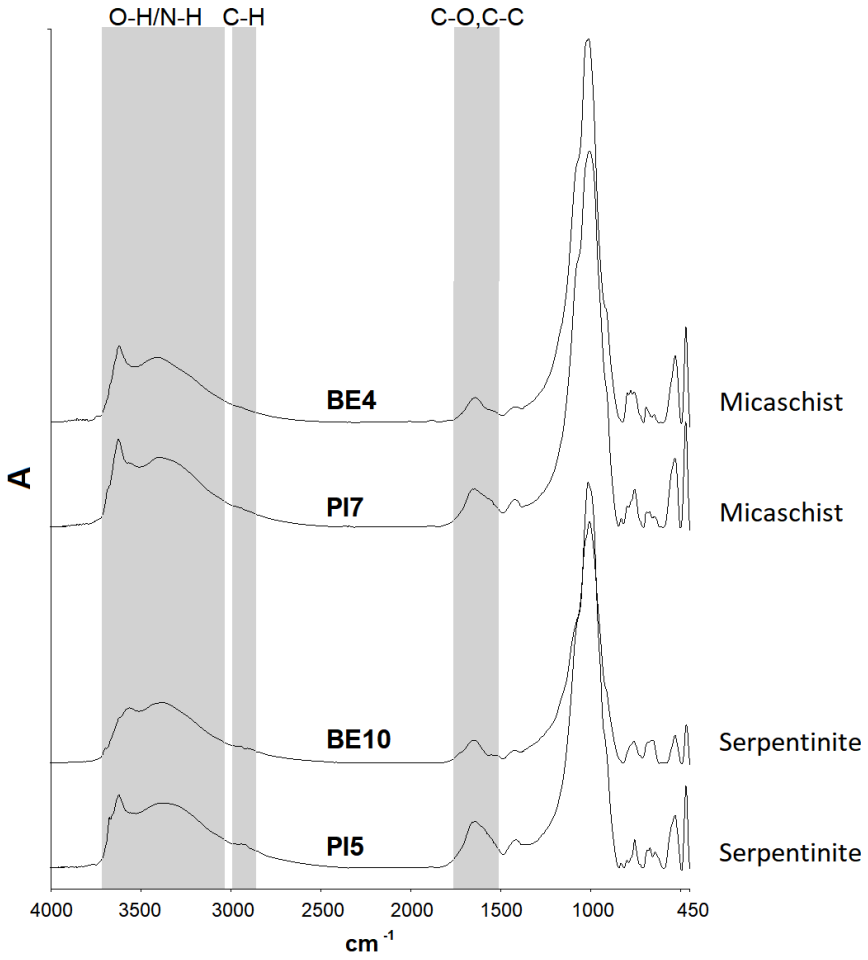

Figura 2.3: FT-IR spectra of bulk soil samples BE4, BE10, PI7 and PI5.

Water repellency measured by WDPT and CA on unheated samples is visible in **Figure 2.4**. The complete infiltration time ranged from <1 to 9 s in the BE subset and from 4 to over 120 s in the PI soil series. The analyzed soil samples thus displayed a WR behavior ascribable to the categories of wettable (0-5 s), slightly hydrophobic (5-60 s) and moderately hydrophobic (60-600 s) (Bisdom et al., 1993). CA values did not exceed 120° in both sets, the maximum CA value obtainable for a sphere placed on a planar surface. In comparison, the BE subset displayed less variations in WDPT than in CA. Above 90°, which is the

CA threshold value assumed for the occurrence of water infiltration, soil samples clearly displayed two different behaviors. A linear trend could be observed when measuring wettability (WDPT vs CA) in the BE subset ($R=0.922$ $p<0.001$), while an exponential trend emerged for the PI subset ($R=0.894$, $p<0.001$) (**Figure 2.4**).

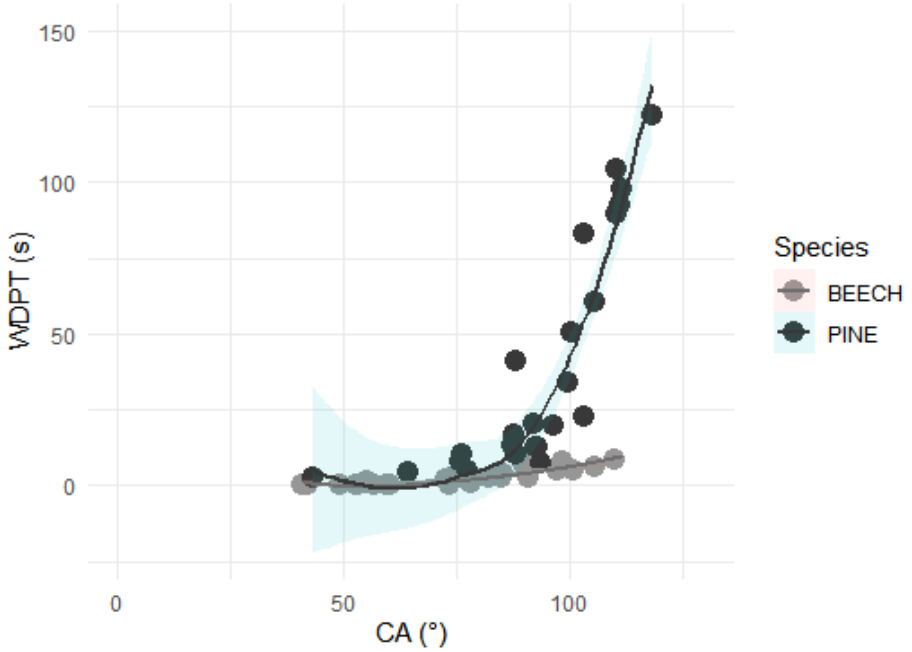

Figure 2.4: Scatterplot with WDPT (s) and CA (°) in the two datasets. Shaded area indicates standard deviation.

Infiltration time (WDPT) was found to be directly related to OC ($R=0.839$, $p<0.0001$) and N ($R=0.706$, $p<0.001$) contents. Similar relationships were obtained considering CA as WR estimator ($R=0.789$, $p<0.0001$ and $R=0.767$, $p<0.001$, respectively). No other strong and straightforward relationship emerged between WR measurements and soil properties.

2.3.2. Heating-induced changes in soil properties and WR

After heating, the soils displayed a large variability in WDPT, both in the BE and in the PI subsets (**Figure 2.5**).

Regardless of the species of belonging, not all samples showed an increase in WR upon burning. In the horizons showing greater infiltration times with increasing heat intensities, WDPT peaked in correspondence of 200 °C. The highest WDPT values of the BE subset were lower than those of the PI series, as here extremely high infiltration times were recorded (e.g. over 3500 s in PI1). A drastic drop in infiltration times occurred with temperatures higher than 200 °C (**Figure 2.5**), regardless of the behavior displayed by the samples at lower temperatures.

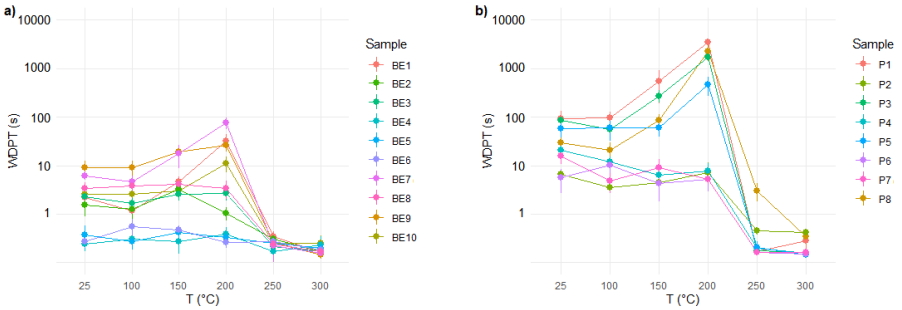

Figure 2.5: Average WDPT (s) measurements and standard deviation in a) BE subset and b) PI subset. Y axis in log scale.

Samples were clustered according to their T-dependent WR behavior (WDPT at all T) within each subset (**Figure 2.6**). In the BE subset (**Figure 2.6a**) the clustering originated three significantly different groups ($p<0.001$) while the PI subset (**Figure 2.6b**) resulted evidently divided into two groups ($p<0.05$). In the BE subset (**Figure 2.6a**), the clustering procedure well isolated the most wettable samples (BE4, BE5, BE6; cluster BE III), which displayed significantly lower infiltration times already at room-temperature ($p<0.001$). The clustering further divided the samples displaying an increase in burning induced WR (BE1, BE7 and BE9; cluster BE I), from those with stationary WR values (cluster BE II). In the PI subset (**Figure 2.6b**), this tendency was even more expressed. Cluster PI I included only the soils with extreme WR at 200 °C. Already at room-temperature, WDPT values of these samples were significantly higher than those of cluster PI II ($p<0.01$).

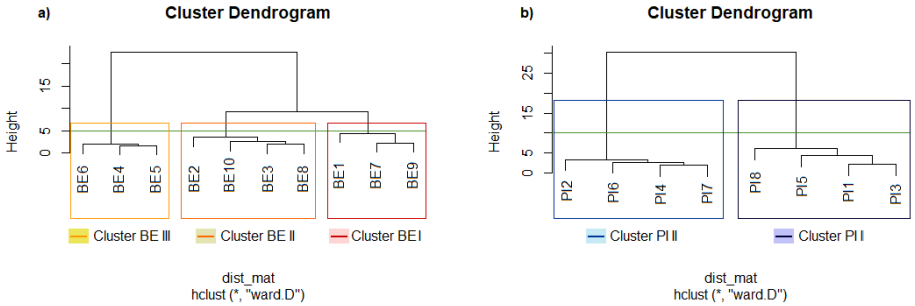

Figure2. 6: Normalized WDPT values with deriving dendrograms, pruning lines and clusters for a) BE subset, b) PI subset.

The pH (**Figure 2.7a**) was, within each species-specific series (BE and PI), significantly lower in more repellent soil clusters ($p<0.001$) while OC and N contents (**Figure 2.7b & 7c**) were, at the same time, significantly higher ($p<0.001$ for both). In all the samples, pH remained stationary until 200 °C (**Figure 2.7a**) then it systematically increased. A similar stationary trend was visible also in organic C contents, which drastically dropped above 200 °C

(**Figure 2.7b**). Total N contents displayed only small variations, occurring mostly in the PI subset (**Figure 2.7c**). Differences in C and pH trends were found to be statistically significant in terms of T ($p<0.001$ for both). At 300 °C, OC content was significantly lower than at less intense Ts, while pH was significantly higher. The combined effect of T and cluster of belonging (T:cluster interaction) was not significant ($p>0.05$ for both). The percentage of OC loss at 300 °C, with respect to the initial OC value, was not significantly greater in different species or clusters ($p>0.05$). Below 250 °C, WR dependency upon OC and N contents was found to be altered by temperature. A strong positive correlation remained between WDPT and OC contents, but the strength of the relationship systematically decreased upon heating ($R=0.913$, $p<0.001$ at 100 °C, $R=0.891$, $p<0.001$ at 150 °C, $R=0.713$, $p<0.001$ at 200 °C). The same happened in the case of WDPT and N, with a less pronounced magnitude ($R=0.691$, $p<0.01$ at 100 °C, $R=0.624$, $p<0.01$ at 150 °C, $R=0.463$, $p<0.05$ at 200 °C). No direct link between the C/N ratio and WDPT could be evinced, as the cluster with less hydrophobic soils had a lower C/N value, but without any statistical significance ($p>0.05$).

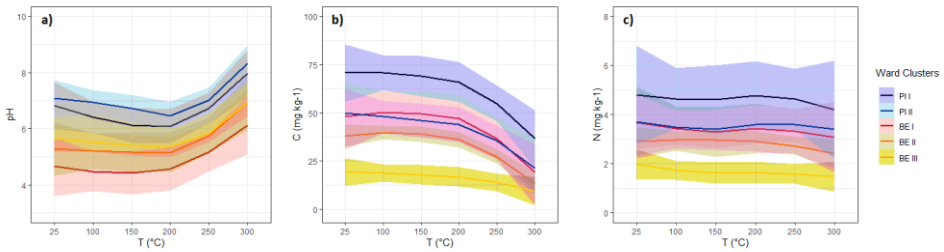

Figure 2.7: Heating-induced changes in a) pH, b) OC (g kg^{-1}) and c) N (g kg^{-1}). Samples are colored by cluster (mean and st. dev.).

Upon increasing temperature, the FT-IR spectra became more and more featureless (**Figure 2.8a**). The greatest changes in intensity were appreciated in the regions corresponding to O-H/N-H and C-H groups (3500 to 2900 cm^{-1}) and C-C, C-O (1650-1500 cm^{-1}) of OM. No heat-mediated variation occurred in correspondence of 3700-3600 cm^{-1}, which suggests that O-H groups visible in that region mostly belong to soil minerals and became more visible with growing T (especially in BE4, PI7 and PI5). **Figure 2.8b** shows the ratio between the peak area at 3500-2900 cm^{-1} to the peak area at 3700-3600 cm^{-1} (that did not change upon heating). No evident modifications occurred in the 3500-2900 cm^{-1} band up to 200 °C, if not a slight reduction in samples BE4 and PI5. A sharp reduction took place at 300° C in all the samples, indicating that most of O-H and C-H groups of OM were affected at this temperature. **Figure 2.8c** displays the ratio between the peak area at 1650-1500 cm^{-1} to the peak area at 3700-3600 cm^{-1}. Also in this case heating up to 200 °C did not cause significant changes, if not a slight increase in the 1650-1500 cm^{-1} region in BE10 and PI7, likely due to an enrichment of aromatic moieties. When reaching

300 °C, all the soils lost the greatest part of functional groups in this region (C-C, C-O of aromatic compounds). The greatest loss can be observed in the BE subset, especially in the case of the least hydrophobic and OM poorest of the selected samples (BE4). PI soil samples were slightly less affected, especially the most WR and OM richest (PI5).

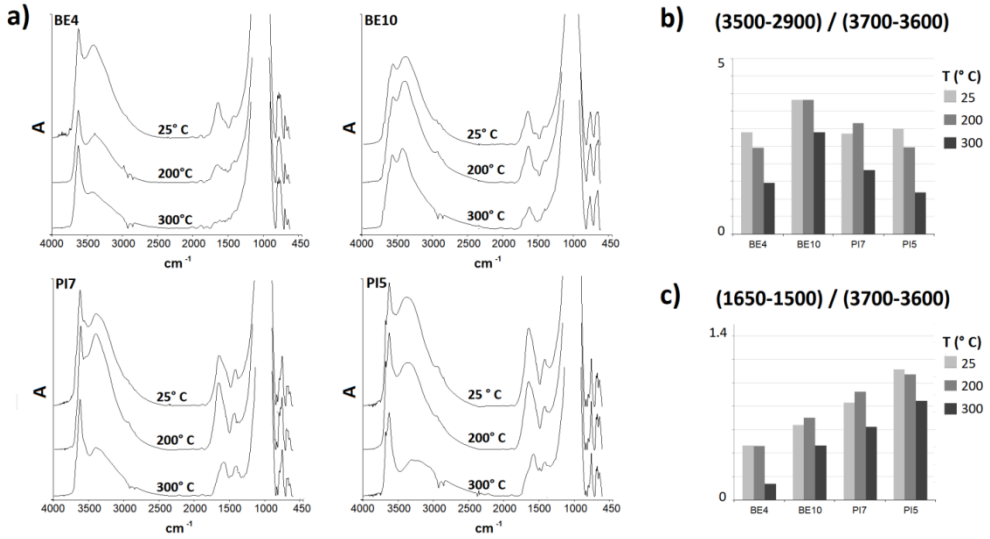

Figure 2.8: a) FT-IR spectra of the selected samples (BE4, BE10, PI7 and PI5) with increasing T (25-200-300 °C). Absorbance at 1200-1000 cm^{-1} was cut to better focus on the bands at 3500-2900 cm^{-1} and 1650-1500 cm^{-1}; b) Ratio of band areas (3500-2900) / (3700-3600) cm^{-1} for all the selected samples at all T; c) Ratio of band areas (1650-1500) / (3700-3600) cm^{-1} for all the selected samples at all T.

Soil clusters containing samples with a greater WR tendency, within each species-specific subset (namely cl. BE I and cl. PI I), were enriched in serpentine (**Figure 2.9a**) and DCB-extractable Fe (**Figure 2.9b**), but the differences were not statistically significant (p>0.05 for both).

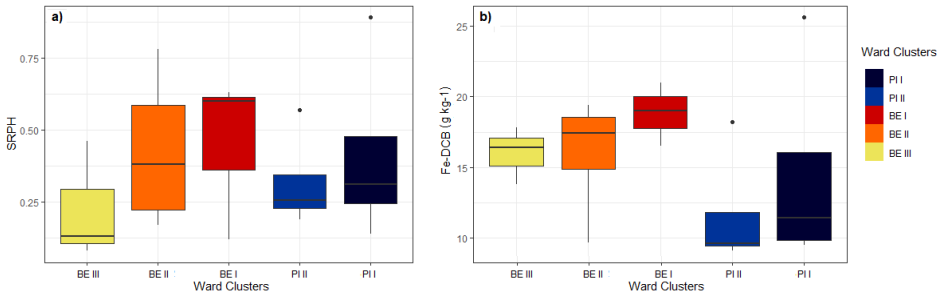

Figura 2.9: Boxplots with a) SRPH and b) DCB-extractable Fe. Data are grouped according to cluster of belonging (least to most WR, from cl. BE III to cl. PI I).

The main soil parameters involved in WR formation at 200 °C, T at which hydrophobic behavior was maximum, were employed to depict two PCA objects, one for each soil series (BE and PI, **Figure 2.10a & 2.10b**). The explained variance accounted for more than 60 % in both cases (71 % BE series, 68 % PI series). In **Figure 2.10a**, BE subset, PC1 was intimately tied to the abundance of either sand or silt and DCB-extractable Fe. PC2 was instead related on one extreme to higher contents of clay and on the other extreme to greater contributions of OC and SRPH. In **Figure 2.10b**, PI soil series, PC1 was mostly ruled by PSD (sand on one side, silt and clay on the other), while PC2 was tied to DCB-extractable Fe and OC contents. The difference existing between clusters PI II and PI I seems to be related to the abundance of fine fractions, whereas, for BE samples, cluster BE III (most wettable behavior) was oriented towards lower C and greater clay contents.

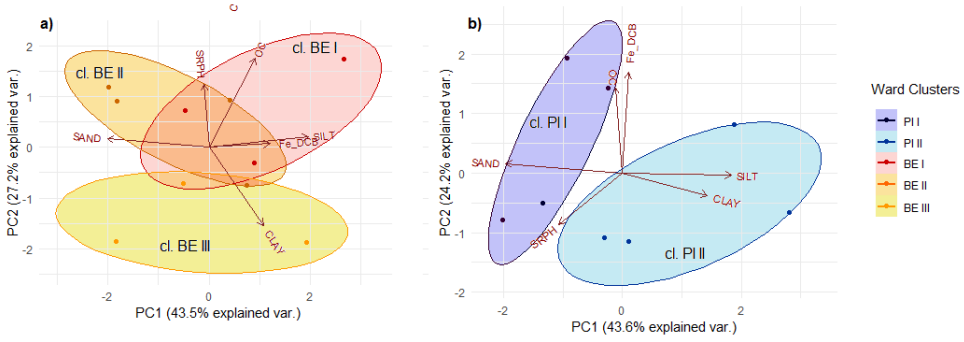

Figure 2.10: PCA with selected soil properties at 200 °C with samples colored according to WR cluster in a) BE subset and b) PI subset.

2.4 Discussion

Heating-induced WR was found to be significantly tied to natural WR in A horizons of alpine soils. Regardless of the vegetation cover type (pine or beech forests), T-mediated hydrophobicity build-up occurred in soils that displayed the least wettable behavior already at 25 °C, in agreement with the literature (Atanassova and Doerr, 2011). These samples maximized WR at 200 °C. Conversely, other samples did not exhibit any increase in WR with growing temperatures, with low and stationary infiltration times. Regardless of the WR behavior displayed until 200 °C, WR was always lost above that temperature.

2.4.1 What regulates room-temperature soil WR?

Unheated samples of the PI subset resulted moderately hydrophobic, while the majority of soils in the BE subset were wettable, according to the classification by Bisdom et al. (1993). The two methods employed for WR estimation (WDPT and CA) were in agreement with each other, as found by Papierowska et al. (2018), but the relationship existing between them differed in the two soil series (BE vs PI, **Figure 2.4**). WDPT and CA were linearly related in the BE subset, while the relationship was exponential in the PI soil series. CA

addresses the initial repellency of a soil, while WDPT does not give an estimate of the actual degree of hydrophobicity but rather deals with the persistence of WR (Diehl, 2013). Thus, samples of the PI subset, despite falling in the same CA range of beech specimens, exhibited a far greater persistence of repellency.

Organic carbon content (significantly higher in the PI series) was found to be the dominant factor regulating room-temperature WR in the analyzed poorly developed alpine soils. The relationship between the degree of soil WR and OM abundance was sometimes found to be positive (Mao et al., 2014), sometimes negative (Teramura, 1980) and sometimes nonexistent (de Blas et al., 2010). Some authors mention the existence of an OC saturation threshold in correspondence of which the addition of extra OM does not induce a greater hydrophobicity in soil (Doerr et al., 2000). In our case, no evidence suggesting OM surface saturation was observable, despite the high OC contents (up to 97 g kg^{-1}). Not only WR was found to be strongly related to the amounts of organic C, but its dependency upon OM composition stood out as well. Considering the two species separately, in fact, the relationship between WR and OC resulted stronger in the BE subset ($R=0.867$, $p<0.001$ for CA, $R=0.927$, $p<0.001$ for WDPT) with respect to the PI subset ($R=0.643$, $p<0.05$ for CA, $R=0.548$, $p<0.05$ for WDPT). This implies that in presence of more hydrophobic OM, testified by the greater amount of aromatic compounds in the PI samples (**Figure 2.8c**), a weaker correlation between WR and OC contents exists. Conversely, when OM is characterized by a lower degree of intrinsic hydrophobicity (BE series, with less predominance of aromatic compounds), a greater dependency upon OC loadings occurs. Aromatic compounds might easily interact with uncharged mineral surfaces (like those of quartz and other primary minerals) via hydrophobic forces (Oudou and Hansen, 2002). The coarsest soil fractions, mainly composed of inherited minerals in alpine soils, could therefore not only trigger a greater WR because of a low surface area but they could also potentially offer surfaces with a high affinity for hydrophobic organic molecules. The relationship between WR and soil properties may therefore result as highly complex and multifaceted, especially in the case of pine.

2.4.2 What regulates heating-induced WR evolution?

The heat-induced increase in WR in the analyzed soil samples was not linear and not homogeneous alongside the T kinetic, and the highest WDPT values were recorded at 200 °C (**Figure 2.5**). The soil clusters (three in the BE subset, two in the PI subset) differed in several soil characteristics that may actually explain their wettability tendencies. Soils with the most repellent behavior (those that experienced heat-induced WR build-up) presented higher OC contents (**Figure 2.7**) and, within their species-specific subset, they were also enriched in DCB-extractable Fe and serpentine in the clay fraction (**Figure 2.9a & 2.9b, Figure 2.10a & 2.10b**). OM tends to bind weakly with serpentine surfaces (Falsone et al., 2016) but their coating could nonetheless enhance WR, as this phyllosilicate has a low surface area. Furthermore, even hydrophilic

mineral surfaces can develop hydrophobic properties when covered with low O/C humic acids (Murphy et al., 1990). As we analyzed A horizons, the soil mineral surfaces were certainly already partially coated by organic compounds at different degrees of transformation. On the other hand, DCB-extractable Fe abundance in more repellent samples might imply a larger extent of high-affinity surfaces that, once experiencing OM coating, could induce a greater WR. A preferential adsorption of reactive aromatic compounds was reported on Fe oxy-hydroxides (Chassé et al ., 2015; Newcomb et al., 2017). It seems therefore plausible to hypothesize that an extremely, if not the most, hydrophobic fraction of OM tends to adhere on the surface of oxides. As framed by the PCAs at 200 °C, nevertheless, factors regulating WR did not act in the same way in the two analyzed soil series. The BE subset (**Figure 2.10a**) presented the least repellent soil cluster in correspondence of greater amounts of clay together with low OC and SRPH contents. In the PI soil subset (**Figure 2.10b**) DCB-extractable Fe and OC were oriented in the same direction, but the two WR clusters mainly differed in terms of PSD (sand vs silt and clay abundance). The relatively hydrophilic PI7, for example, was not actually poor in OM (OC=69 g kg^{-1}) but presented the highest amount of clay in the whole dataset (**Table 2.2**). As expected, a greater WR is generally experienced by coarse-textured soils (DeBano, 1991; Doerr et al., 2000; Scott, 2000), with low clay contents (Harper et al., 2000). In this context, anyway, not all factors controlling WR remained unaltered in the investigated T range. The change in the relationship between WR and OC from 25 to 200 °C (decreasing strength of the correlations WDPT vs OC and CA vs OC) could imply that, with growing temperatures, not only OM quantity but also T-induced changes in OM quality determine the degree of WR experienced by a soil. Burning has different effects on OM, primarily depending on the nature of the source material, together with charring intensity and oxygen availability (Knicker, 2007). The frequently reported increase in OM aromaticity (Baldock and Smernik, 2002; Knicker, 2011) seems to be the key factor inducing a more efficient coating of mineral particles, thus promoting a greater WR. The observation of functional groups by FT-IR spectroscopy revealed that a small reduction in surface hydroxyl groups and aliphatic compounds (3500-2900 cm^{-1}) occurred already at 200 °C (**Figure 2.8b**). Conversely, aromatic compounds (C-C, C-O stretching at 1650-1500 cm^{-1}, **Figure 2.8c**) were well represented and even slightly more present. The wide variety of WR behaviors displayed by these soils could ultimately be linked also to OM patchy distribution on mineral surfaces (Kaiser and Guggenberger, 2003).

Up to 200 °C, the pH remained mostly unchanged (**Figure 2.7a**). WR is reported to be maximum when soils remain in the range of their natural pH (Graber et al., 2009). In addition, a greater repellency is usually observed for soils with low pH values. As the pKa of carboxylic acids falls in the pH range of 3-5 (Diehl et al., 2010), a reduction in repulsion forces between these groups may cause micelle-like aggregation with outward-oriented hydrophobic moieties (Duval et al., 2005; Terashima et al., 2004). **Figure 2.7a** in fact

displays that, within each species-specific subset, the most repellent group had lower pH values.

2.4.3 What causes WR loss above 200 °C?

Literature usually reports WR to be lost above T-thresholds of more than 250 °C (DeBano, 2000). In some studies (e.g. Mataix-Solera et al., 2008), Mediterranean soils heated up to 350 °C for 20 minutes still displayed a distinctive WR behavior (more than 2000 s of infiltration time). In our case, for alpine soils, WR disappeared already just above 200 °C, when a sharp reduction in OC was visible (**Figure 2.7b**). A decrease in OC is generally observed starting from 220 °C (Giovannini et al., 1988), but the greatest OC losses are usually experienced between 250 and 450 °C (Araya et al., 2017, 2016) for a greater volatilization triggered by intense heating (Knicker, 2011). A larger sensitivity towards thermal alteration of OM in high elevation forest soils was observed also in other environments, even in case of moderate heating temperatures (Santos et al., 2016). Burning soils above 200 °C caused here a neat flattening of the FT-IR spectra (**Figure 2.8**). However, not all the organic compounds were affected to the same extent. The areas corresponding to stretching of O-H/N-H and C-H (**Figure 2.8b**) and C-C,C-O (**Figure 2.8c**) groups decreased in all the analyzed samples from 200 to 300 °C. Other studies observed a reduction in C-H stretching (2950-2850 cm^{-1}), corresponding to aliphatic groups (Šimkovic et al., 2008) and a significant decrease in O-H stretching peaks (3700-3000 cm^{-1}) occurring around 250 °C (Araya et al., 2017). The persisting peak in correspondence of 3700-3600 cm^{-1} (**Figure 2.8**) was attributed to O-H of soil 1:1 clay minerals like serpentine (Russell, 1987). Nitrogen, on the contrary, did not show any systematically decreasing trend (**Figure 2.5c**), but indeed N greatest loss, for combustion and volatilization, generally occurs only above 350 °C (Araya et al., 2017).

However, OC loss is not likely the sole responsible for the dramatic decrease of WR observed in the transition from 200 to 250 °C, as the samples of the most hydrophobic cluster, cl. PI I, were still rich in OM at 250 °C (more than 50 g kg^{-1} OC, **Figure 2.7b**). Thus, in order to understand what is inducing a hydrophilic behavior in soil, we need to consider the alterations occurring in the mineral phase and how these modifications influence bonds with OM. The layer silicate structure is generally not affected by temperatures around 250-300 °C, while hematite formation from goethite is reported to occur close to 250 °C (Brown, 1980). Also, thermal transformations of ferrihydrite typically require temperatures of at least 300 °C, depending on the amounts of incorporated Si or metals (Jambor and Dutrizac, 1998). The surface area of hematite is generally much lower than that of ferrihydrite (32 vs 245 m^2 g^{-1}) (Kaiser and Guggenberger, 2003; Celi et al., 2020), therefore these thermal modifications should induce a more efficient OM coating of mineral surfaces, giving rise to a greater WR. Nevertheless, the sorption capacity of mineral surfaces and the interactions with the organic compounds may experience changes by the increase in pH visible above 200 °C (**Figure 2.7a**). This phenomenon could be attributed to proton consuming decarboxylation reactions and release of base

cations from organic matter (Badìa and Martì, 2003). As aforementioned, outward orienting of hydrophobic moieties in amphiphilic micelles occurs only at relatively low pH values (Duval et al., 2005; Terashima et al., 2004). As pH increases, a change in OM conformation may lead to more charged and elongated structures. A systematic increase in pH can in parallel trigger a more negative surface charge of soil mineral surfaces, especially where 1:1 phyllosilicates dominate (Dixon et al., 1990). OM sorption to mineral phases would thus be heavily affected because of the increased electrostatic repulsion between highly negatively charged surfaces (Mayer and Xing, 2001). It is indeed likely that, above 200 °C, the remaining OM could be partially desorbed due to the increased negative charges. This would increase the fraction of mineral surfaces that become OM-free and available for interaction with water molecules, leading to the complete loss of WR.

CHAPTER 3

Fire simulations effects on the transformation of iron minerals in alpine soils

3.1 Introduction

The extent of organo-mineral associations is tightly related to the amount and type of surfaces involved in the interaction (as demonstrated in Chapter 2) and, in soil, a leading role is played by the surface of Fe oxides.

As mentioned in the Introduction, different Fe speciation pathways may arise according to native soil Fe species at rising Ts. Also, content and composition of soil OM may direct the heat-induced transformations of Fe oxides. In soil, high-T induced electron shuttling from OM to electron acceptors may not always involve O_2 (Schwertmann, 1988; Yang et al., 2016), due to a fast consumption of this gas with respect to its limited diffusion, further hindered by consistent heat-induced water evaporation (Jeleńska et al., 2010). Consequently, Fe(III) species may be involved as electron acceptors.

In quantitative terms, increasing organic carbon (OC) loads have been documented to promote formation of more ferromagnetic minerals in heated mixtures of Fe oxides and sugars (Till and Nowaczyk, 2018). In qualitative terms, OM compounds derived from coniferous vegetation could release considerable amounts of pyrolysis by-products, like carbon monoxide and other reduced gases (Liu et al., 2017), whose potential as an electron transfer source to Fe species has been verified (Jozwiak et al., 2007), even in the case of soil heating experiments performed in air (Johnston et al., 2019).

We accounted for Fe speciation in forest topsoils heated at temperatures of 200 and 300 °C, choosing samples that differed in starting mineralogical composition and OM. To cope with the complexity posed by the soil matrix, we employed (among others) an advanced spectroscopic technique, synchrotron-light based X-ray absorption spectroscopy (XAS), which has been successfully applied to assess oxidation state, local bonding environment and electronic structure of atoms (Espinosa et al., 2011; Kawai, 2010) even in matrixes as heterogeneous as soils (Giannetta et al., 2022).

Therefore, the aims of this chapter are: i) to follow the thermal transformations of Fe oxides in soils and verify whether they are primarily driven by starting mineralogy and OM content and composition; ii) to detect the evolution of the OM pool towards which Fe phases display the highest affinity at environmentally realistic heating conditions (Ts).

3.2 Materials and methods

3.2.1 Soil samples and heating treatment

We employed the same set of samples already described (**Figure 2.1, Table 2.1**) as, for the present experiment, we wanted to test our hypothesis on samples differing in mineralogy and OM content and composition. These soils developed on different lithology, i.e. ophiolitic outcrops and calcschists, under contrasting canopy cover, i.e. *Fagus sylvatica* L. (BEECH subset, 10 samples) and *Pinus sylvetsris* L. (PINE subset, 8 samples), with variable OC contents (**Table 2.2**).

We compared samples kept at RT condition with samples heated at Ts of 200 and 300 °C. Such T-thresholds were selected according to three main criteria: 1) these Ts correspond to low-moderate fire intensities widely experienced in fire-affected soils (Janzen and Tobin-Janzen, 2008); 2) Fe speciation, as above mentioned (Chapter 1), is expected to start occurring in this T-range; 2) we observed major variations in organo-mineral associations exactly at 200 and 300 °C in our previous investigation on these soils (Chapter 2).

3.2.2 Wet chemistry

Na-Dithionite-citrate-bicarbonate (DCB) was used to quantify total Fe oxides (Mehra and Jackson, 1958), while ammonium oxalate solution in the dark (OXA) was employed to assess the contribution of poorly ordered Fe oxides (Schwertmann, 1964). The OM-bound Fe pool was isolated with a sodium pyrophosphate solution (PYRO) (Loeppert R.H., 1996). Fe concentrations in the extracts were quantified by atomic absorption spectrometry, AAS (PerkinElmer AAnalyst 400, Norwalk, CT, USA). The different Fe pools are henceforth addressed as Fe_{DCB}, Fe_{OXA} and Fe_{PYRO}, respectively.

The OC concentrations in the 0.45 µm filtered PYRO extractants (OC_{PYRO}) were determined by Pt-catalyzed high T combustion (650 °C) followed by infrared CO2 detection (VarioTOC, Elementar, Hanau, Germany).The OM extracted by Na-pyrophosphate solution was further characterized. Optical properties were inspected by recording absorbance at characteristic wavelengths: 254 (A_{254}), 250 and 365 nm (Helios UV-Vis spectrophotometer, Thermo Electron, Massachusetts, USA). Specific UV absorbance (SUVA) of the PYRO extraction, proxy for dissolved OM aromaticity, was calculated as A254 normalized by OC_{PYRO} concentration (Weishaar et al., 2003). As larger OM compounds absorb the light more strongly at longer wavelengths, the E2:E3 ratio was calculated as the absorbance at 250 nm divided by that at 365 nm (Peuravuori and Pihlaja, 1997). Method blanks were analyzed in parallel with the samples.

The extractions were carried out on all the samples (18 samples x 3 T), while refined instrumental techniques were applied for selected specimens only. To meet the objective of this work, we chose samples BE4, BE10, PI5 and PI7. These soils differed in parent material (BE4 and PI7 developed on schist, while

BE10 and PI5 developed on serpentinite), forest cover (BEECH vs. PINE), and presented a wide variability in OC contents (**Table 2.2**). These soils were further characterized, both at RT condition and at 200 and 300 °C..

3.2.3 Microscopy and X-ray Diffraction

The morphology and composition of soil particles were inspected via field-emission scanning electron microscopy (FE-SEM, TESCAN S9000G) with energy dispersive spectrometer (EDS, Oxford detector). A small amount (~30 mg) of powdered sample was mounted on stubs with carbon conductive tape. Sample sputtering was performed in Ar atmosphere with 60 mA current for 50 seconds, obtaining a 25 nm film of gold over the samples. The samples were examined both in back-scattered electron (BSE) and secondary electrons (SE) emission mode to investigate heavy-elements distribution and topographic features, respectively. Elemental maps were derived by the EDS probe.

Soil mineralogy of finely ground powder samples -randomly oriented mounts- was characterized by XRD using a Philips PW 1710 diffractometer (40 kV, 20 mA, Co-Kα radiation and graphite monochromator). Scans were acquired from 2° to 50° 2θ at a speed of 1° 2θ min^{-1}. Background subtraction and data smoothing was performed with PowderX software (Dong, 1999). Phase identification was carried out using the International Centre for Diffraction Data (ICDD) database.

3.2.4 Magnetic measurements

Loss-on-ignition (LOI) values (**Table 3.1**) were determined by measuring sample mass before and after heating at 200 and 300 °C.

Table 1.1: LOI values as mass difference (ambient - higher T) to initial sample mass (g $100g^{-1}$).

ID	LOI 200 °C (g $100g^{-1}$)	LOI 300 °C (g $100g^{-1}$)
BE4	0.248	0.825
BE10	0.138	0.506
PI5	0.151	0.643
PI7	0.259	0.811

Small amounts (100 mg) of finely ground soil samples were packed into gelatin capsules with quartz wool for hysteresis and low-T magnetic measurements and were precisely weighed. Hysteresis loops were measured on a vibrating sample magnetometer at RT up to a maximum field of 1 T to account for saturation magnetization (M_S), saturation remanent magnetization (M_R) and coercitivity (H_C), after applying an appropriate fitting method for high-field slope correction (Jackson and Solheid, 2010). Low-T magnetic properties were measured on two selected samples (BE4 and PI5), and additional information on phase transitions

were derived by low-T magnetization using a SQUID magnetometer (MPMS, Quantum Design, San Diego, CA, United states). Low-T procedures included measuring a saturation isothermal remanence (SIRM) imparted at 20 °K on warming to 300 °K after either field-cooling (FC) or zero-field-cooling (ZFC), as well as low-T cycling of RT SIRM, known as the FC-ZFC-LTSIRM-RTSIRM-LTD protocol (Bilardello D. and Jackson, 2013). All remanence and susceptibility values were normalized by the sample masses.

3.2.5 X-ray Absorption Spectroscopy

Both unheated and heated bulk soil samples were analyzed for Fe K-edge XAS. Spectra were collected at the XAFS beamline at Elettra Sincrotrone (Trieste, Italy) (Aquilanti et al., 2017). Powdered soil samples (~50 mg) were pressed into pellets with the addition of PVP, sealed with Kapton tape and mounted onto a sample holder at RT. Spectra were collected in transmission mode, accounting for beam attenuation as a function of incoming photon energy (Mobilio, 2015) using a Si (111) monochromator calibrated to the first-derivative maximum of the K-edge absorption spectrum of metallic Fe foil (7112 eV). The foil was continuously monitored to account for small energy shifts during sample measurements. Higher harmonics in the beam were eliminated by detuning the monochromator by 30 % of its maximal intensity. Multiple scans per sample were acquired.

Full X-ray absorption near-edge spectroscopy (XANES) and Extended X-ray absorption fine-structure (EXAFS) were targeted. Data processing (i.e., reference alignment, background subtraction, normalization, de-glitching and spectra merging) was performed using the Athena software (Ravel and Newville, 2005).

The contribution of different Fe species was assessed by comparing our spectra with atomic structures of reference Fe-bearing compounds (O'Day et al., 2004) (**Figure 3.1**): ferrihydrite, goethite, hematite, maghemite, magnetite, smectite, chlorite and Fe(III)-citrate, the latter of which is widely used as a model compound for Fe(III)-OM complexes (Giannetta et al., 2022). Linear combination fitting (LCF) was performed both in the XANES and EXAFS region, without constraining the sum of the fitted fractions to reach 100 %. We focused on the -20 to 40 μ(E) energy range for XANES and on the 2.5−12 $Å^{-1}$ range for the EXAFS region (k^3-weighted spectra).

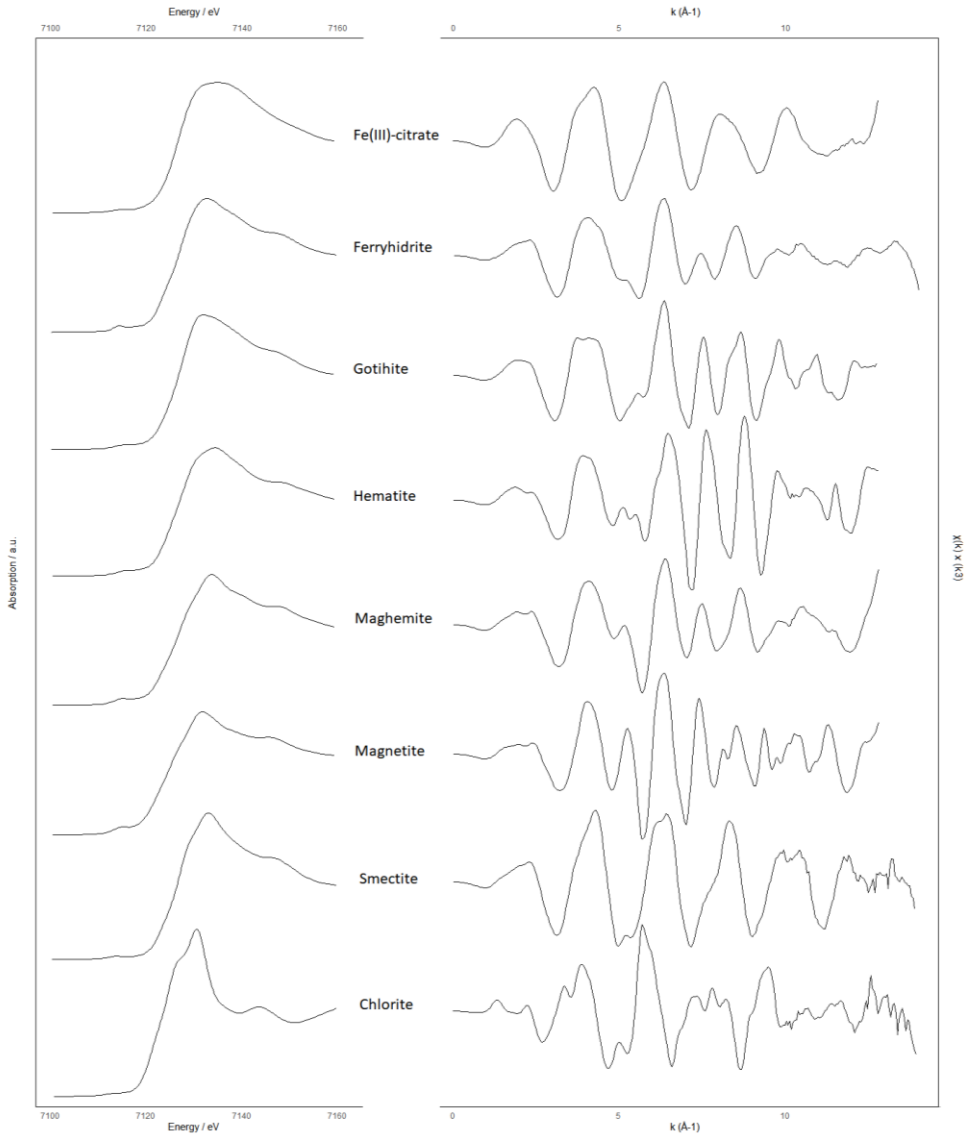

Figure 3.1: XANES and EXAFS spectra of reference compounds.

3.2.5 Statistical analyses

RStudio (R version 4.0.2) was used for the statistical analyses. Data normality and homoscedasticity were inspected by Shapiro-Wilk's and Levene's tests, respectively, before group comparisons. One-way ANOVA (level of statistical significance set at 0.05) was used to detect differences in mean values between groups, with Tukey-HSD test as post hoc for pairwise comparisons. Linear mixed models (LMM) were implemented when investigating trends, so as to verify the role played by selected covariates alongside the T-kinetic (25-200-300 °C). Autocorrelation, when present, was considered within the model

structure and the best fitting model was chosen based on Akaike's information criterion (AIC). Correlation coefficients were extracted from correlation matrixes computed with the Pearson parametric method.

Regarding LCF outputs, we are aware of the most recent and validated statistical method in use in this field (Giannetta et al., 2020). The high complexity and multi-faceted nature of our soil samples (reflected in the XAS spectra) prompted us to opt for a more conservative approach, avoiding an expert-driven choice of the best LCF output. To consolidate our findings, we systematically isolated the results that recurred with consistency alongside the T-kinetic.

For each sample at each T, we extracted the first 10 combinational fits both in XANES and EXAFS, and performed Principal Component Analysis (PCA) to observe how the two spectral regions depicted Fe species distribution. As partially expected, the two techniques did not display an identical abundance of reference compounds due a different sensitivity towards crystalline structure and dimension of target-element neighboring atoms (Kawai, 2010) (**Figure 3.2**). The LCF results were thus treated separately (EXAFS vs. XANES).

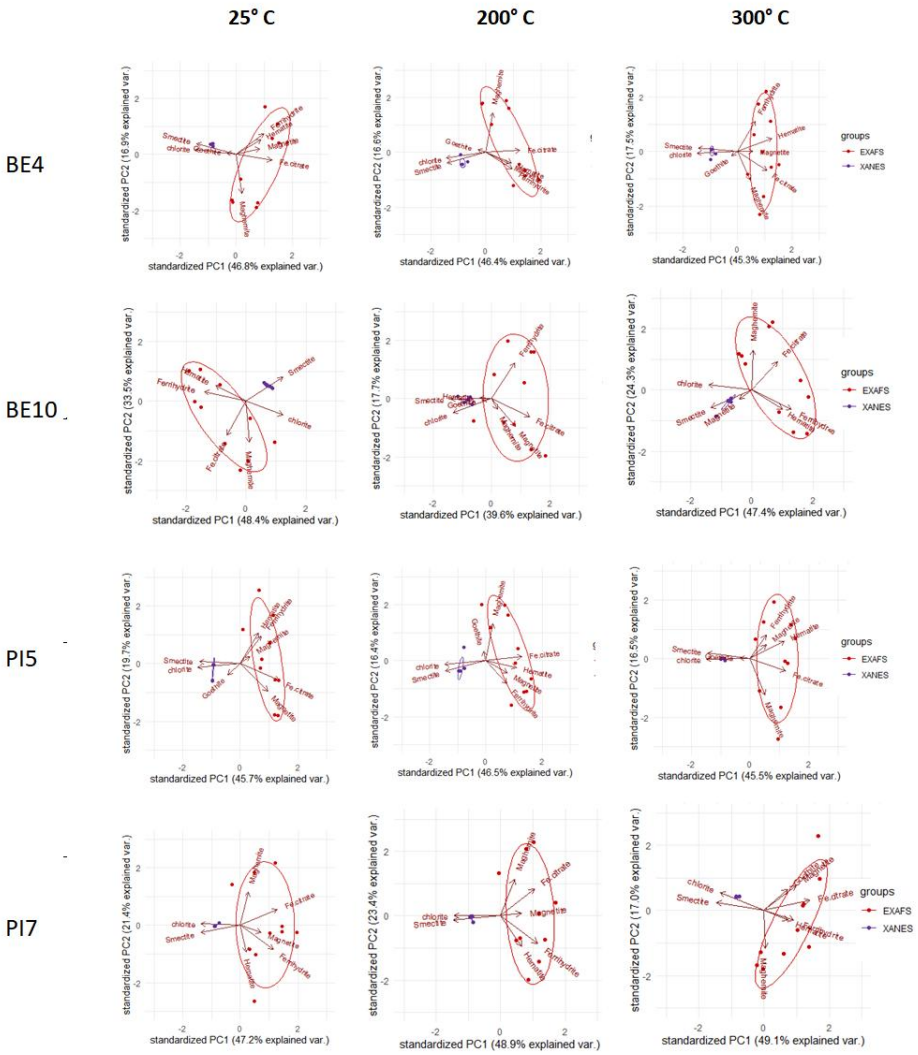

Figure 3.2: PCA biplots depicting distribution of Fe species contributions as LCF outputs in the EXAFS (red) and XANES (purple) regions.

XANES-derived LCF outputs consistently displayed the contributions of mainly 2 (3) reference compounds, so the final Fe species contribution was, in this region, calculated as an average of the identified species.

EXAFS-derived LCF fits, on the contrary, comprised a wide variety of possible species contributions, and further data processing was implemented. We clustered the first 10 LCF outputs obtained at 25, 200 and 300 °C (10 fits x 3 T) for each single sample. After Euclidean distance matrix building, Ward's agglomeration method was selected (Hubert and D indexes were used to

estimate the optimal number of clusters), validating the dendrogram pruning by PERMANOVA (**Figure 3.3**).

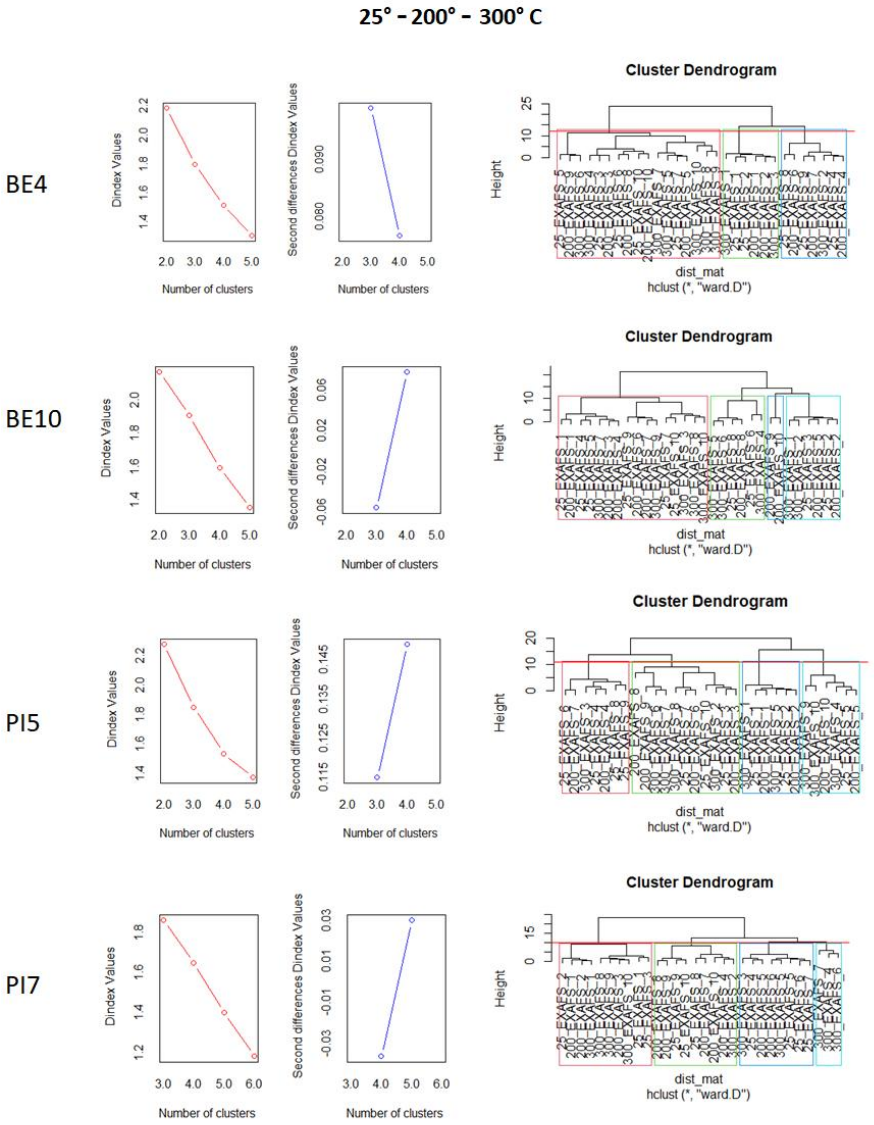

Figure 3.3: EXAFS LCF outputs (10 fits x 3 T) as clustered for each sample.

Choice of the best cluster was performed considering the orientation of clusters in PCA biplots (**Figure 3.4**) and maximizing the goodness of fitting parameters (Chi-squared, AIC, Relative Likelihood and Final Prediction Error). Additionally, we checked the agreement between LCF-derived species abundances and the evidence derived from the other analytical techniques (selective extractions, XRD, microscopy and magnetic data), to validate the

reliability of the data. The final Fe species contributions were calculated as the average abundance of reference compounds within the chosen cluster, separately for each T. Fe species abundances were then normalized to reach 100 %..

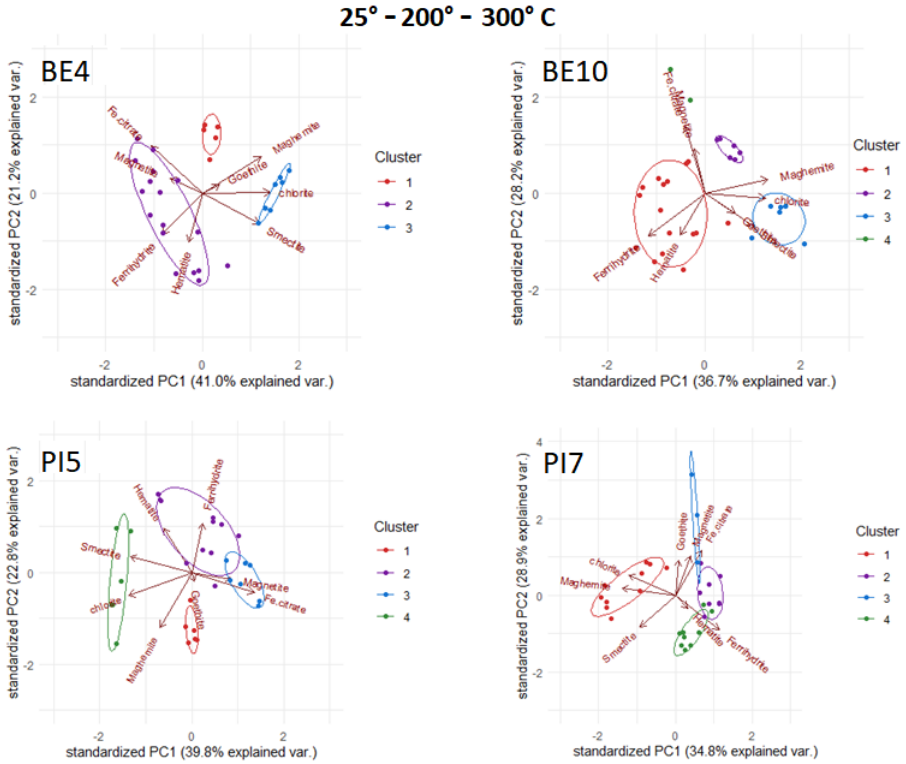

Figure 3.4: PCA biplots depicting distribution of Fe species contributions as EXAFS LCF outputs (10 fits x 3 T). Grouping according to cluster of belonging.

3.3 Results and discussion

3.3.1 Fe pools and crystalline degree

Increasing Ts did not induce any differences in Fe_{DCB} contents ($p>0.05$, Table 1), that were generally higher in BEECH with respect to PINE samples ($p<0.05$). Concentrations of Fe_{OXA} (ranging from 1.3 to 5.0 g kg^{-1}), which is known to mainly comprise Fe in ferrihydrite and -in minor amounts- goethite and magnetite (Campbell and Schwertmann, 1984), were similar in the two soil series (average of 2.7 g kg^{-1} for BEECH and 2.8 g kg^{-1} for PINE). Higher Fe_{OXA} values were detected with increasing heating Ts, with a statistically significant trend only in the BEECH series ($p<0.05$). The Fe_{OXA}:Fe_{DCB} ratio is widely employed as an indicator of phase crystallinity (Hall et al., 2018) and, for our samples at RT condition, it underlined the remarkable contribution of poorly

ordered Fe phases (mean=17.4 %; st.dev=8.9 %). This feature is consistent with the scarce degree of development expected in alpine soils, and the inhibitory effects of OM on oxide crystallization (Borggaard, 1985). It is especially true for the PINE samples, that had a significantly higher OC content when compared to BEECH (49.7 g kg^{-1} vs. 27.5 g kg^{-1}, $p<0.01$) and displayed significantly greater Fe_{OXA}:Fe_{DCB} values (24.1 % vs. 15.6 %, $p<0.01$).

No significant decrease in Fe_{OXA}:Fe_{DCB} was detected upon increasing Ts in BEECH and PINE soils (**Table 3.2**), suggesting that the heating treatment at 200 and 300 °C did not promote the formation of more crystalline species. Regarding organo-mineral complexes, the soil samples exhibited a consistent decrease in this pool upon increasing T, in line with existing studies (Norouzi and Ramezanpour, 2013). The downtrend detected in Fe_{PYRO}:Fe_{DCB} with increasing T was, however, more pronounced and significant only in the BEECH subset ($p<0.05$).

Table 3.2. Fe concentration in solution in DCB, OXA and PYRO extractions. Samples at 25-200-300 °C.

Sample	T (°C)	Fe_{DCB} (g kg^{-1})	Fe_{OXA} (g kg^{-1})	Fe_{PYRO} (g kg^{-1})	Fe_{OXA} : Fe_{DCB} (%)	Fe_{PYRO} : Fe_{DCB} (%)
BE1	25	16.5	3.2	3.0	19.4	18.2
	200	17.5	3.3	2.6	18.9	14.9
	300	18.7	4.1	1.1	21.9	5.9
BE2	25	16.6	2.6	1.6	15.7	9.6
	200	16.8	4.9	1.2	29.2	7.1
	300	17.1	4.9	0.7	28.7	4.1
BE3	25	19.4	1.9	0.7	9.8	3.6
	200	20.0	2.7	0.6	13.5	3.0
	300	20.9	2.9	0.5	13.9	2.4
BE4	25	13.8	2.1	0.9	15.2	6.5
	200	13.7	2.3	0.7	16.8	5.1
	300	13.9	3.0	0.4	21.6	2.9
BE5	25	16.4	2.3	1.0	14.0	6.1
	200	15.5	2.3	0.9	14.8	5.8
	300	16.7	2.7	0.4	16.2	2.4
BE6	25	17.8	1.3	0.7	7.3	3.9
	200	17.5	1.4	0.6	8.0	3.4
	300	21.4	1.7	0.3	7.9	1.4
BE7	25	21.0	1.5	1.3	7.1	6.2
	200	21.1	1.4	0.9	6.6	4.3
	300	24.4	1.7	0.4	7.0	1.6
BE8	25	18.3	3.0	1.4	16.4	7.7
	200	19.6	3.8	1.1	19.4	5.6
	300	21.7	3.8	0.7	17.5	3.2

	25	19.0	2.1	1.3	11.1	6.8
BE9	200	19.5	4.8	1.1	24.6	5.6
	300	23.3	3.5	0.8	15.0	3.4
	25	9.7	1.3	0.8	13.4	8.2
BE10	200	8.7	1.6	0.7	18.4	8.0
	300	9.6	1.8	0.5	18.8	5.2
	25	25.6	1.4	2.3	5.5	9.0
PI1	200	20.8	2.0	0.9	9.6	4.3
	300	21.8	2.4	0.9	11.0	4.1
	25	9.7	1.7	0.7	17.5	7.2
PI2	200	9.8	1.3	0.7	13.3	7.1
	300	10.1	1.7	0.5	16.8	5.0
	25	12.9	3.1	1.3	24.0	10.1
PI3	200	12.5	2.4	1.2	19.2	9.6
	300	14.5	3.4	1.1	23.4	7.6
	25	18.2	4.0	2.0	22.0	11.0
PI4	200	18.6	4.1	1.5	22.0	8.1
	300	19.8	5.0	0.7	25.3	3.5
	25	10.0	2.5	1.1	25.0	11.0
PI5	200	10.4	3.9	1.1	37.5	10.6
	300	10.5	2.9	0.9	27.6	8.6
	25	9.6	3.2	0.7	33.3	7.3
PI6	200	9.2	3.4	0.9	37.0	9.8
	300	10.0	3.3	0.8	33.0	8.0
	25	9.1	3.6	1.2	39.6	13.2
PI7	200	8.9	3.9	1.2	43.8	13.5
	300	9.9	3.8	1.0	38.4	10.1
	25	9.5	1.6	0.2	16.8	2.1
PI8	200	9.4	1.4	0.2	14.9	2.1
	300	10.1	2.1	0.3	20.8	3.0

Soil specimens were characterized by a high level of complexity and intimate interconnection of multiple phases. The presence of Fe oxides was corroborated by elemental maps, revealing that the main constituents of the inspected particles were Fe, O, Si, Al and C (**Figures 3.5** and **3.6**). Fe phases were often found to encrust soil particles (**Figure 3.5**, lower panel). Infrequently, they appeared as spherical structures (**Figure 3.6**, lower panel), likely derived from a heat-induced synthesis process, leading to the minimization of surface energy (Bora et al., 2012). Analogous, although smaller, C-rich Fe oxides spherules have also been observed in soils affected by natural fires (Jordanova et al., 2019).

In addition, Fe oxides occurred in the shape of husks (**Figure 3.5**, zoom a), disordered spherical features (**Figure 3.5**, zoom b), rods (**Figure 3.5**, zoom c) and flakes (**Figure 3.6**, zoom a).

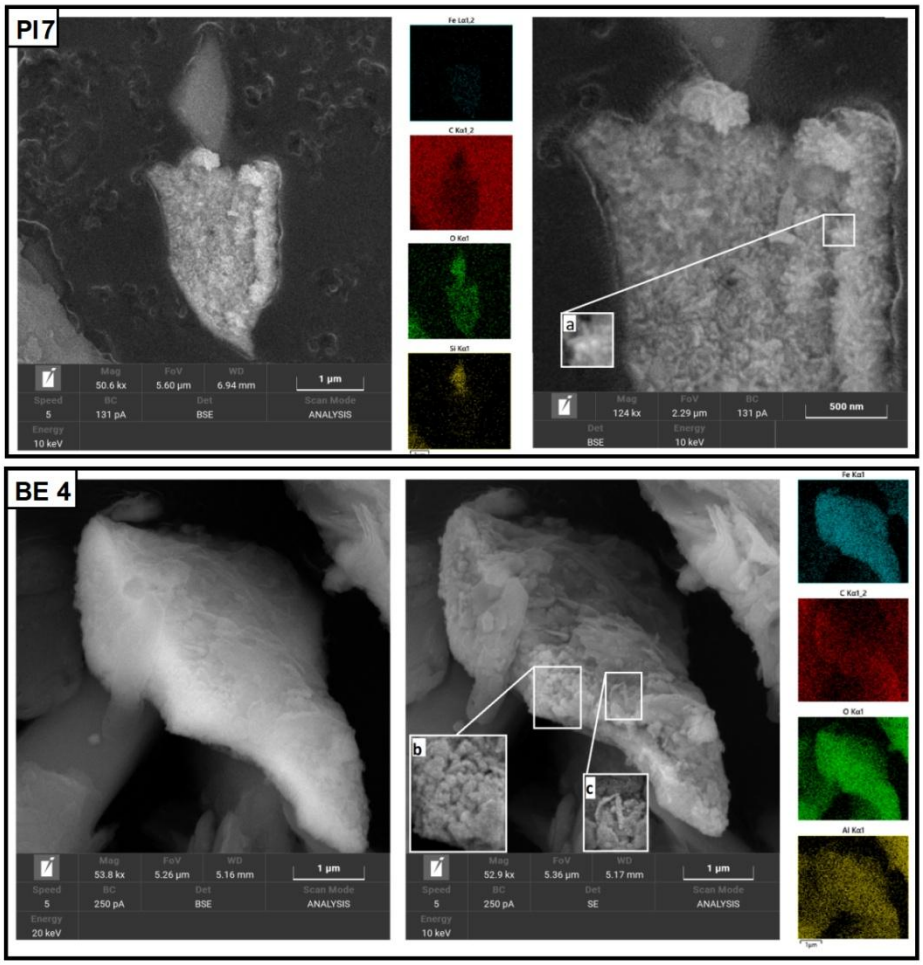

Figure 3.5. FE-SEM images of sample PI7 at 200 °C (upper panel) and sample BE4 at 200 °C (lower panel). Elemental maps and zooms on selected morphological details (a, b, c) are displayed.

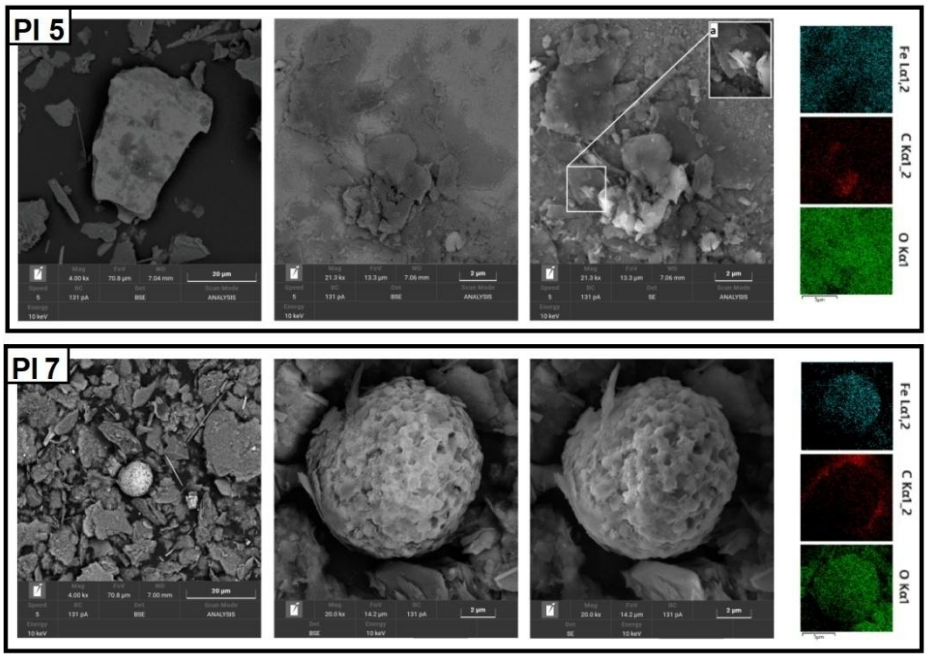

Figure 3.6. FE-SEM images of sample PI5 at 300 °C (upper panel) and sample PI7 at 300 °C (lower panel). Elemental maps and a zoom on a selected morphological detail (a) are displayed.

3.3.2 Identification of Fe oxides and magnetic properties

As expected from the site selection, the soils differed in terms of starting mineralogical composition (**Figure 3.7**). Chlorite was identified by the presence of all its basal reflections: 0.141 (*001*), 0.706 (*002*), 0.471 (*003*), 0.354 (*004*) and 0.284 (*005*) nm. Other detectable minerals were micas (0.992, 0.959, 0.490 and 0.333 nm), feldspars (0.321 and 0.290 nm), amphiboles (0.840 nm) and talc (0.935, 0.271 nm). The peak in correspondence of 0.730 nm, characteristic of serpentine, presented the highest intensity in sample PI5.

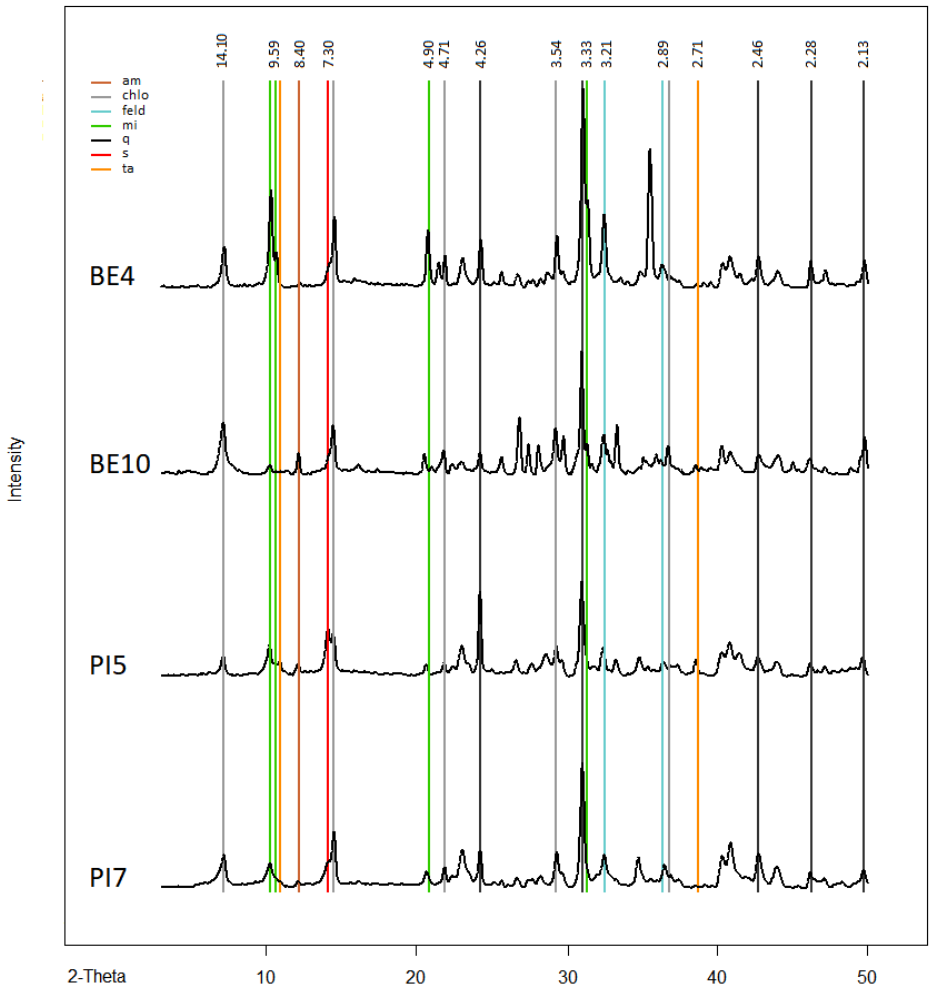

Figura 3.7: Complete XRD spectra of the selected samples at room-T in black solid line. Vertical lines correspond to characteristic reflections, in Å, of amphiboles (am), chlorite (chlo), feldspars (feld), mica (mi), quartz (q), serpentine (s) and talc (ta).

For chlorite, the low intensity of the *003* (0.471 nm) respect to the *002* (0.706 nm) and the *004* (0.354 nm) reflections indicates the presence of a Fe-enriched mineral. Estimation of Fe atoms symmetry in octahedral *vs*. silicate layers (D) and Fe content in the octahedral layer (Y) was performed according to existing literature (Moore and Reynolds Jr., 1989) by considering the intensities of *002*, *003*, *004* and *005* reflections (**Table 3.3**).

Table 3.3: Values corresponding to symmetry of Fe distribution in octahedral vs. silicate layers (D) and number of Fe atoms in six octahedral sites (Y).

ID	*002*	*003*	*004*	*005*	I (*003*) / I (*005*)	D	I (*003*)'	(I(*002*)+ I(*004*)) /I(*003*)'	Y
BE4	173	78	126	28	2.79	0.5	86.90	3.44	1.05
BE10	120	61	114	34	1.79	0.9	75.19	3.11	0.86
PI5	104	35	74	26	1.35	1.2	46.22	3.85	1.28
PI7	135	50	87	31	1.61	1.0	63.21	3.51	1.09

At RT, goethite was not detected in the XRD patterns (no peaks at 0.418 nm, the highest intensity reflection of goethite) (**Figure 3.8**). Small amounts of ferrihydrite were potentially indicated in BE4 and PI7 by the broad reflection at 0.224 nm. The presence of either maghemite or magnetite was evident in reflections at 0.251-0.253 nm in BE4, BE10, and PI5 (with a stronger signal in the latter than in the other samples).

Increasing Ts induced only small variations in reflections attributed to Fe oxides, with a minor increase in maghemite or magnetite in BE10 at 300 °C (peak at 0.251 nm, possibly overlapping with hematite) and hematite formation in PI5 at 300 °C (reflection at 0.269 nm). Sharper reflections ascribable to Fe oxides with increasing Ts were not detected, confirming that the tested Ts did not cause a complete transition to Fe species with a long-range structural order, as already suggested by the results of the chemical extractions.

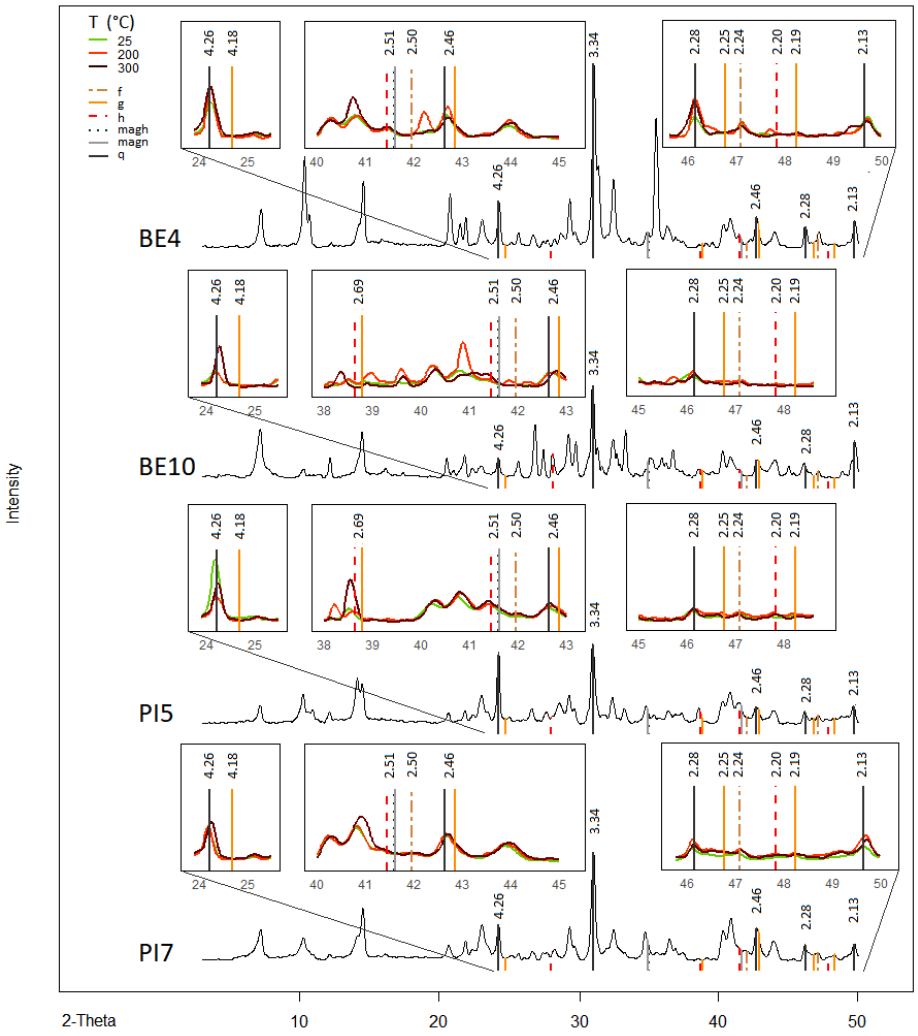

Figure 3.8. Complete XRD spectra of the selected samples in black solid line, with panels focusing on selected region. Colour code assigned according to sample T (green: 25 °C, orange: 200 °C, brown: 300 °C). Vertical lines correspond to characteristic reflections, in Å, of ferrihydrite (f), goethite (g), hematite (h), maghemite (magh), magnetite (magn) and quartz (q).

Low-T remanence measurements revealed the presence of ferromagnetic minerals in samples BE4 and PI5 at RT (**Figures 3.9a** and **3.9b**). The Verwey transition (hump at 120 °K), characteristic of magnetite, was more prominent in sample PI5 than in BE4, especially at 300 °C. The slightly suppressed Verwey transition in BE4 likely represents a composition with more maghemite or partially oxidized magnetite. Sample PI5 also exhibits higher ZFC curves than FC curves below 120 °K, which indicates a greater proportion of multi-domain, coarser-grained magnetite than single-domain magnetite (Carter-Stiglitz et al.,

2006). In contrast, BE4 displays higher FC values than ZFC, which is typical in samples dominated by single-domain size particles. MS values (**Figures 3.9c**) were notably higher in PI5 with respect to the other samples, pointing to a greater concentration of magnetic minerals (a measurement that is independent of grain size) (Liu et al., 2012). This agrees with the peak representing either maghemite or magnetite in the XRD spectra of PI5 (**Figure 3.8**), and may reflect the presence of lithogenic magnetite in the serpentinite soil parent material (Oze et al., 2004).
The hysteresis squareness plot (**Figures 3.9d**) did not show any systematic change in domain state with higher heating Ts.

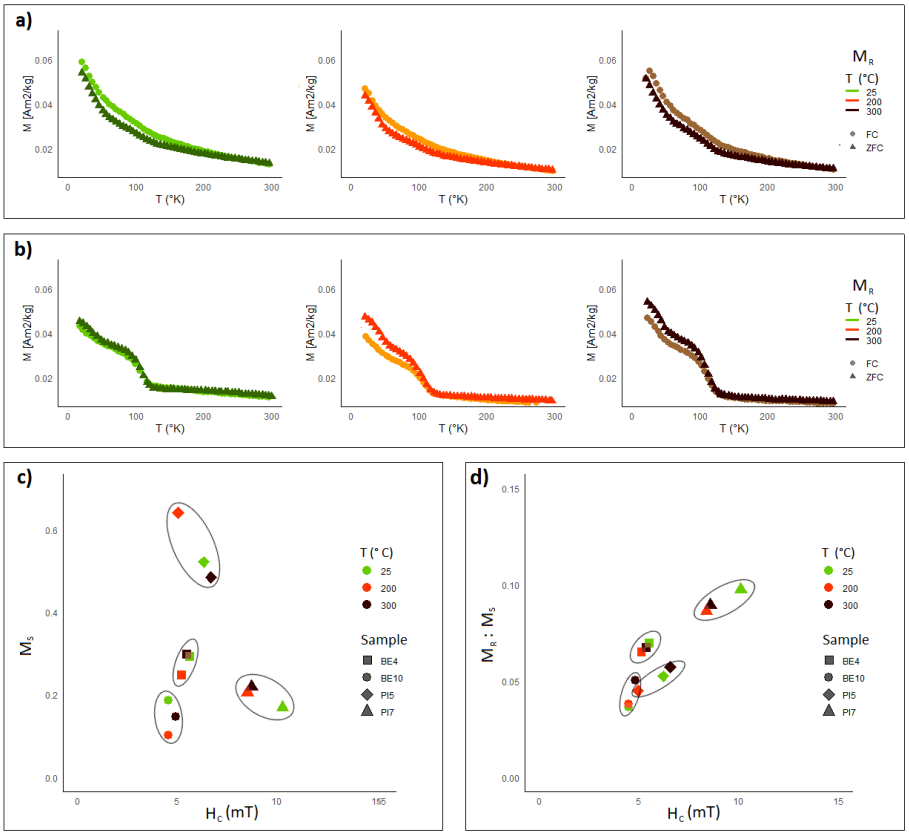

Figure 3.9. Low-T remanence measurements after field-cooling (FC) and zero-field cooling (ZFC) of a) sample BE4 at 25-200-300 °C; b) sample PI5 at 25-200-300 °C; c) saturation magnetization measurements *vs.* HC; d) hysteresis squareness plot (M_R:M_S *vs.* H_C). Colour code assigned according to T (green: 25 °C, orange: 200 °C, brown: 300 °C), marker shape assigned according to sample type.

Hysteresis parameters in the range observed here (M_R:M_S<0.1, H_C>5mT) are characteristic of superparamagnetic particles, likely mixed with single-domain grains (Till et al., 2010). Also, H_C and M_R:M_S values did not unequivocally increase, a trend that would have suggested growth of nano-particles. PI7 exhibited a shift towards lower values upon higher T, while the opposite trend

was displayed by sample BE10. The duality in particle-size transition trends (moderate in entity) is not totally unexpected. On one side, pyrogenic ferromagnetic phases have been documented to be finer-grained than typical pedogenic mineral assemblages (Oldfield and Crowther, 2007; Schwertmann, 1988). At the same time, Ts close to 300 °C are known to promote particle aggregation, with an increase in the size distribution and a modification of particle morphology (Redl et al., 2004). There was little observable difference in low-T susceptibility for heated and unheated samples of BE4 (**Figure 3.10**). Specifically, the frequency dependence varied little, revealing an overall stable mean nano-particle size (a slight decrease at 200°, followed by values similar to RT conditions at 300 °C).

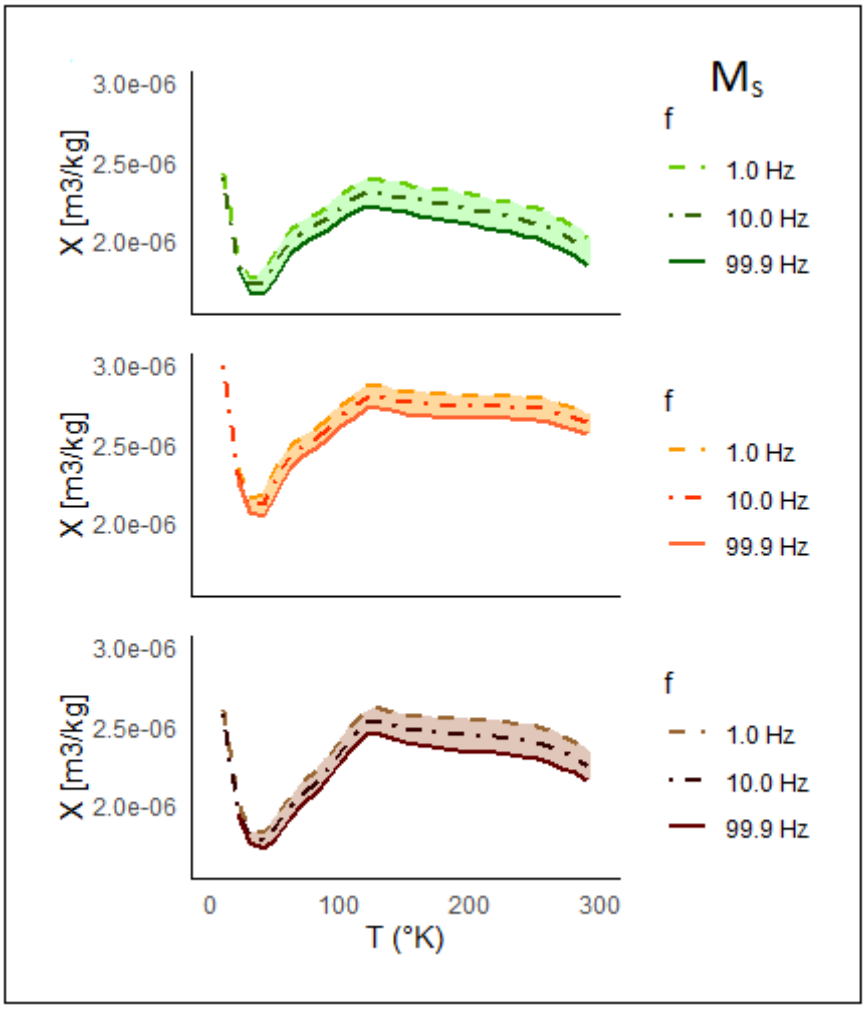

Figure 3.10: Low-T susceptibility measurements on sample BE4 at 25-200-300 °C. Shaded areas depict the difference between 1-Hz and 99.9-Hz alternating fields.

XANES indicated the occurrence of, mainly, chlorite, smectite and, occasionally, goethite (**Table 3.4**), with hardly any difference in Fe speciation for unheated *vs.* heated samples. The contribution of other compounds -Fe(III)-citrate- was minimum. Although chlorite and smectite were the most abundant, their relative contributions differed between the soils (slightly more smectite in BE10 and more chlorite in PI7). The signal from Fe-rich chlorite detected in diffraction patterns (**Figure 3.7**, **Table 3.3**) agrees with the spectroscopic analysis. Smectite was not visible in the XRD spectra of bulk samples, because of the lack of glycerol treatment, but the presence of swelling minerals in these soils was already documented in a previous work (Bonifacio et al., 2010).

EXAFS proved to be more sensitive to Fe(III)-citrate and oxides rather than Fe-bearing phyllosilicates (**Table 3.4**). Still, an abundance of chlorite in PI7 was evident also in EXAFS data. Maghemite was identified as the dominant Fe oxide, with a rather homogeneous content in the samples (mean=28 %; st.dev=3 %). Ferrihydrite was identified in negligible amounts in sample PI7, despite its presence was expected in soils as little developed as these are.

Given the highly different magnetic signatures of the soils (**Figure 3.9**), we also expected a diversity in starting Fe species composition. Still, as XRD showed the reflections characteristics of either magnetite or maghemite in three out of four cases (BE4, BE10, PI5), it is reasonable to hypothesize a varying degree of magnetic mineral oxidation.

.

Table 3.4. Fe species percentages as obtained by LCF after the clustering procedure, operated separately in the XANES and in the EXAFS region. Data have been normalized to reach 100 %.

Region	ID	T (°C)	Chlorite	Fe(III)-citrate	Ferrihydrite	Goethite	Hematite	Maghemite	Magnetite	Smectite
XANES	BE4	25	45			2				53
		200	47	1		2				50
		300	48	1		1				50
	BE10	25	34							66
		200	38	1		2				59
		300	42							58
	PI5	25	52			4				44
		200	52	1		2				45
		300	48			2				50
	PI7	25	80							20
		200	77							23
		300	78							22

EXAFS	BE4	25	34	33			1	32	
		200	36	30			2	32	
		300	35	28			5	32	
	BE10	25	34	29				33	4
		200	37	32				26	5
		300	39	29				30	2
	PI5	25	42	31			1	26	
		200	42	29			3	26	
		300	41	27			6	26	
	PI7	25	50	13	1			25	11
		200	52	13				27	8
		300	55	5		1		29	10

3.3.3 Thermal transformation of Fe species

According to XAS, increasing Ts hardly induced any changes in Fe speciation in two of the four samples (BE10, PI7), while the other two displayed a small but evident phase transition (**Table 3.4**).

The occurrence of oxidative processes was testified by the appearance of hematite in samples BE4 and PI5 (more than 5 % at 300 °C). These contents are relatively small and close to the detection limit of the instrument, but the tendency in increasing values is well expressed and consistent in both samples. We hypothesize involvement of organo-mineral complexes in hematite formation, as EXAFS exhibited decreasing Fe(III)-citrate abundance with increasing T (in BE4, PI5, and PI7, Table 2), and the same occurred for the Fe_{PYRO}:Fe_{DCB} ratio (**Table 3.2**). Possibly, this T-induced trend appeared more marked in the wet chemistry results because, in EXAFS, the signal of metal species forming inner-sphere complexes within mineral particles tends to be amplified (Martínez et al., 2006).

Also, conversion of maghemite into hematite has not to be excluded. This transformation is a structural T-driven inversion, involving the (*111*) and (*100*) axes of maghemite and (*001*) and (*100*) of hematite (Bora et al., 2012), resulting in a mineral species with a lower enthalpy under aerobic surface conditions (Johnston et al., 2019).

The Morin transition (characteristic of hematite) was not observed in low-T remanence measurements of heated/unheated BE4 and PI5 (no hump at 260 °K in **Figures 3.9a** and **3.9b**). The lack of this trait could be ascribed to vacancies and impurities or, alternatively, could be due to the presence of very small particles (Coey, 1988) (plausible, as derived by the squareness plot, **Figure 3.9c**). The presence of small hematite particles would also explain why there was no noticeable increase in coercitivity with heating in these samples. Additionally, it is consistent with the increase in Fe_{OXA} upon heating, as fine

grained oxides, albeit crystalline, are more sensitive to this chemical extraction (Lanzl et al., 2012). We hence tend to consider maghemite as an intermediate form that would, eventually, lose stability starting from 200 °C.
The transitional nature of maghemite and the T corresponding to its full hematite conversion are still debated as this process in soils is highly dependent on grain size and impurities (Till et al., 2021). The crystalline degree of maghemite, which is usually poor at these Ts (Jeleńska et al., 2010), would agree with the unaltered Fe_{OXA}:Fe_{DCB} ratio observed upon soil heating (**Table 3.2**). This mineral assumes prismatic features over 600 °C (Bora et al., 2012), remaining in the form of husk-like structures up to 250 °C (Sayed and Polshettiwar, 2015). We witnessed the presence of Fe-rich particles composed of superimposed husks in PI7 (**Figure 3.5**, zoom a), so it is likely that those crystals comprised maghemite formations (maintaining such a shape up to 200 °C).
XANES also evidenced the presence of goethite in samples BE4 and PI5 (Table 2). We did not detect this mineral in the XRD spectra (**Figure 3.8**). Still, the presence of potential goethite could be inferred by direct inspection of sample BE4 (**Figure 3.5**, zoom c), as goethite has often been observed as nano-rods (Penn et al., 2006) and lath-shaped crystals in soils heated at 250-300 °C (Dionísio et al., 2009). We are then prone to hypothesize that conversion of goethite into hematite also presumably occurred. This transformation, attributed to the well documented dehydroxylation reaction (Schwertmann and Fechter, 1984), usually begins at 150 °C in isolated minerals (Cudennec and Lecerf, 2005) and was previously observed at 250 °C in heated soils (Dionísio et al., 2009). Mild-T conversion of goethite into hematite would produce a highly disordered mineral structure, with excessive OH^- and Fe-deficiency, rich in nano-pores due to shrinking occurring during dehydration (Gualtieri and Venturelli, 1999). Thus, proto-hematite formation seems a plausible result of the heating treatment in our soils, and the poor crystalline degree of this mineral would also explain the lack of decreasing Fe_{OXA}:Fe_{DCB} values (that would mirror an increase in crystalline order) for greater heat intensities (**Table 3.2**).

3.3.4 Organo-mineral association – interactions and affinity

Reducing conditions, required for magnetite formation, were plausibly established within the soil matrix at high T. A great concentration of magnetic minerals emerged for PI5 (**Figure 3.9b**, pronounced hump in low-T remanence measurements at 300 °C), which contained greater amounts of OC with respect to BE4 (**Table 2.2**). We did not observe a clear decreasing trend in coercitivity values with increasing Ts (**Figure 3.9c** and **3.9d**) and, thus, the formation of pure magnetite has to be excluded (also, XAS did not detect magnetite). Rather, we could ascribe the oscillating coercitivity values to the presence of maghemite along with magnetite. Interfaces between antiferromagnetic and ferromagnetic phases could in fact induce magnetic exchange coupling, with intergrowth of partially oxidized titanomagnetite (Evans and Heller, 2003) and incorporation of magnetite seeds within iron nano-phases (Redl et al., 2004). The reducing conditions were probably not strong enough to lead to detectable

magnetite formation, or to prevent the partial transition of maghemite to hematite.
Considering OM quality, samples PI5 and PI7 have exhibited a clear OM aromatic character, with abundant C=C and C=O functional groups, as testified by bulk soil FT-IR spectroscopy (**Figure 2.8**). This feature might concur in explaining the magnetic mineral enrichment in sample PI5, which did not occur for BE4 (due to less OM and more labile compounds).

A systematic decrease in soil OC at T > 200 °C, occurring in concomitance with an increase in pH, was observed in our previous investigation (**Figure 2.7**). OC_{PYRO}, conversely to Fe_{PYRO}:Fe_{DCB}, did not display a systematic decrease upon increasing T (**Figure 3.11a**). The pyrophosphate solution is not strictly selective for the extraction of Fe-bound OM as it targets all the dispersible OM pools, i.e. free, water soluble, in organo-metallic complexes and bound to polymeric metal phases and small sized minerals (Kögel-Knabner et al., 2008).
The OC_{PYRO}:OC contents at RT (**Figure 3.11b**) are in line with existing data of forest soils (Ohno et al., 2017), and a relative enrichment in the PYRO-dispersible OM pool emerged at the highest tested T. The anticorrelation between OC_{PYRO}:OC *vs.* OC ($R=-0.651$, $p<0.001$) occurred in parallel with a relatively weak and yet significant positive relationship between OC_{PYRO}:OC and pH in PINE samples ($R=0.569$, $p<0.01$). Decreasing E2:E3 values of PYRO-extracted OM were detected for PINE samples at greater Ts (**Figure 3.11c**), a downtrend that mirrors a slight increase in molecular size of the extracted OM, consistent with the heat-induced formation of large polycondensed compounds (Knicker, 2011). Trends in PYRO-extracted OM SUVA, proxy for aromaticity (Weishaar et al., 2003), were contrasting in the two datasets (BEECH *vs.* PINE, **Figure 3.11d**). The highest recorded values, for PINE at 300 °C, express the great aromatic character of the isolated OM, as expected from the thermal alteration of its starting OM composition (Knicker, 2011; Negri et al., 2021). The PINE subset exhibited the presence of large aromatic compounds at high-T (slight but significant anticorrelation between SUVA *vs.* E2:E3; $R=-0.512$, $p<0.05$), while more labile compounds emerged in BEECH for increasing Ts (anticorrelation OC_{PYRO}:OC *vs.* SUVA, $R=-0.522$, $p<0.001$).

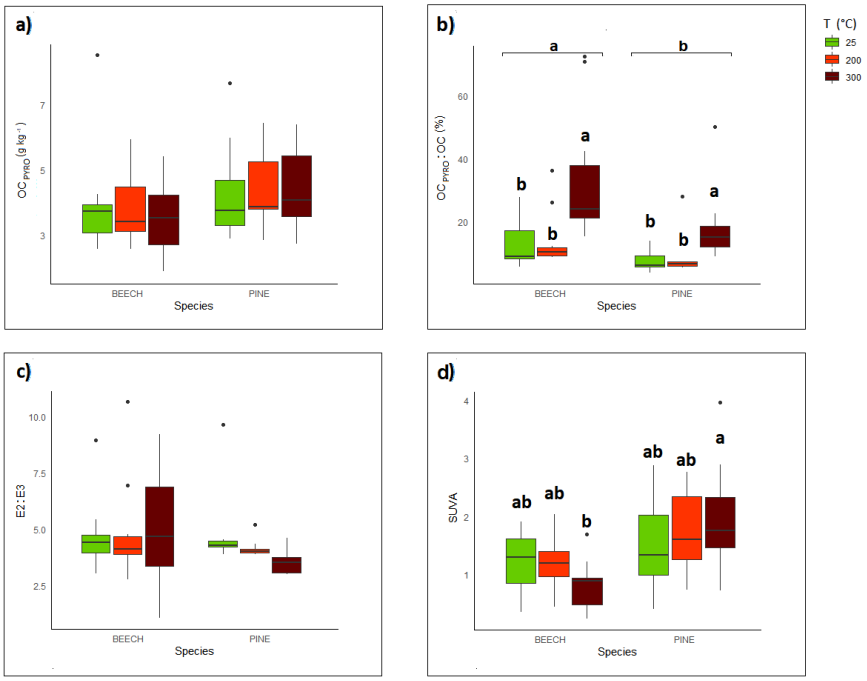

Figura 3.11: Boxplots depicting a) OC_{PYRO}:OC (%), b) E2:E3, c) SUVA of the PYRO extraction. Colour code assigned according to T (green: 25 °C, orange: 200 °C, brown: 300 °C).

Regarding OM stabilization dynamics, a greater mineral-bound OM fraction (the non-dispersible pool) was found in PINE rather than in BEECH samples ($p<0.01$, **Figure 3.11 a**). This could be ascribed to a strikingly different OM composition, resulting in the preferential association of large (Ohno et al., 2017) aromatic (Chassé et al ., 2015) compounds with Fe oxides. Still, at 300 °C we observed a higher fraction of dispersible OM in both the subsets. This suggests that, despite the abundance of aromatic compounds at least in heated PINE samples (**Figure 3.11 c**), OM adhesion to mineral surfaces was not favored by high Ts.

On this point, we should consider that large organic clods and bulky OM agglomerations are known to be more easily extractable (because of a less intimate adhesion) (Kaiser and Guggenberger, 2007). Also, the abrupt increase in pH caused by OM combustion and the consequent increase in the negative surface charge of most soil mineral particles (Diehl et al., 2010) may have favoured a more pronounced electrostatic repulsion (Mayer and Xing, 2001), eventually leading to weaker organo-mineral associations.

CHAPTER 4

Divergent heating response patterns in soils belonging to various natural ecosystems

4.1 Introduction

Soil WR and aggregate stability (AS) are expected to change at rising Ts due to organic and mineral phases transformations, as shown in the previous chapters. The abundance and composition of both minerals and OM are highly dependent on the factors of soil formation, and their interaction is likely to differ according to soil variability.

The role played by OM in ruling soil WR is a complex one: other than content, composition is highly relevant. In addition to the features illustrated in Chapters 1 and 2, lipid involvement in WR formation has been observed (Lozano et al., 2013), with distinct WR tendencies according to lipid distribution among soil size fractions (Ellerbrock and Gerke, 2004; Jiménez-Morillo et al., 2016; Zheng et al., 2016). Yet, it hasn't been established if heat-induced WR increase (and loss) occurs due to a mere structural re-arrangement or due to shifts in OM composition. Nor it has been clarified how the amount of mineral surfaces available for OM sorption directs soil wettability, despite extensive literature (Chapter 1) has deemed this parameter as fundamental.

Regarding soil AS, some authors hypothesize that, rather than total OC content, only a fraction of OM actually reflects into modifications in AS (Badía-Villas et al., 2014), especially in presence of specific OM compounds (Kavdir et al., 2005). When soil OM contents are lower than 5-6 % (Boix-Fayos et al., 2001), the cementing effect of crystalline and poorly-ordered Fe and Al oxides might dominate over OM (Six et al., 2002), and changes in Fe oxides occurring at moderate heating Ts (below 300 °C) could possibly impact AS (Guerrero et al., 2001; Terefe et al., 2008).

Thus, the mineralogical composition of soil parent material, and the soil development degree proper of different environments (Dixon et al., 1990; Wilson, 2004), might be fundamental in ruling ecosystem response to soil heating. Some authors hypothesize that soils belonging to strikingly different biomes may not univocally respond to a thermal treatment (Pellegrini et al., 2022) and, still, literature is lacking of comprehensive studies investigating this matter (Seaton et al., 2019).

This chapter aims at elucidating heating response patterns in highly diverse forest topsoils by addressing factors responsible for thermal modifications in: i) WR and ii) aggregate composition and stability, in a T-range realistically triggered in soil by forest fires.

4.2 Materials and methods

4.2.1 Samples origin and heating treatment

A set of soil samples belonging to highly different environments around the globe was employed (**Figure 4.1**).

Figure 4.1: Distribution of samples across the globe.

The considered samples were surface horizons (A or E horizons) belonging to different climates (Kottek et al., 2006) and soil types (Soil Survey Staff, 1999) (**Table 4.1**), representative of a wide range of biomes and developed under various forest covers.

Table 4.1: Characterization of soil samples employed for the study. *

ID	Region	Climate	Vegetation	Biome	Horizon	Soil type
1	Italy	Cfb	*Castanea sativa* Mill, *Quercus sp*	Temperate forest	A	Typic Udorthent
2	Italy	Dfc	*Pinus sylvestris*, *Sorbus spp*	Boreal forest	A	Lithic Udorthent
3	Italy	Cfb	*Castanea sativa* Mill	Temperate forest	A	Typic Dystrudept
4	Italy	Cfc	*Fagus sylvatica* L.	Temperate forest	A	Typic Calciudoll
5	Italy	Csb	*Fagus sylvatica* L.	Temperate forest	A	Typic Eutrustept
6	Italy	Csb	*Fagus sylvatica* L.	Temperate forest	Ah	Lithic Ustorthent

7	Italy	Csb	*Fagus sylvatica* L.	Temperate forest	Ah	Typic Ustorthent
8	Russia	Dfb	*Picea obovata* Ledeb.	Boreal forest	EA	Typic Glossocryalf
9	Russia	Dfc	*Picea obovata* Ledeb.	Boreal forest	E	Typic Palecryalf
10	Russia	Dfc	*Picea obovata* Ledeb.	Boreal forest	E	Typic Cryaqualf
11	Russia	Dfb	*Picea abies* (L.) Karst	Boreal forest	E/ A	Typic Glossocryalf
12	Russia	Dfb	*Picea abies* (L.) Karst	Boreal forest	E	Typic Glossocryalf
13	Czech Republic	Dfb	*Picea abies* (L.) Karst	Boreal forest	A	Typic Haplocryod
14	Botswana	BSh	*Vangueria infausta* Burch.	Savannah	A	Typic Quartzipsamment
15	Botswana	BSh	*Ricinodendron rautanenii* Schinz	Savannah	A	Typic Quartzipsamment
16	Botswana	BSh	*Vangueria infausta* Burch.	Savannah	A	Typic Quartzipsamment
17	Botswana	BSh	*Strychnos cocculoides* Baker	Savannah	A	Typic Quartzipsamment
18	Mali	Aw	*Burkea Africana* Hook., *Vitellaria paradoxa* C.F.Gaertn.	Savannah	A	Plinthitic Kanhaplustult
19	Mali	Aw	*Guiera senegalensis* J.F. Gmel, *Terminalia macroptera* Guill. & Perr.	Savannah	A	Petroferric Haplustult
20	Mali	Aw	*Butyrospermum parkii*, *Burkea africana* Hook.	Savannah	A	Plinthitic Kanaplustult
21	Chile	ET	*Anarthrophyllum desiderátum* (DC.) *Benth, Berberis microphylla* G.	Steppe	A	Typic Cryorthent
22	Chile	ET	*Berberis microphylla* G., *Ribes magellanicum* Poir.	Magellanic forest	A	Typic Cryorthent
23	Spain	Csa	*Pinus halepensis* Mill, *Quercus*	Mediterranean forest	A	Typic Xerorthent

			coccifera L.			
24	Spain	Csa	*Pinus halepensis* Mill, *Quercus coccifera* L.	Mediterranean forest	A	Typic Rhodoxeralf
25	Spain	Csa	*Pinus halepensis* Mill, *Quercus coccifera* L.,	Mediterranean forest	A	Typic Xerorthent
26	Brazil	Cfa	*Baccharis* spp., *Byrsonima brachybotrys*	Tropical forest	A	Typic Haplustox
27	Brazil	Cfa	*Aristida pallens* Cav, *Allagoptera campestris*	Tropical forest	A	Typic Dystrustept
28	Peru	ET	*Berberis lutea* Ruiz & Pav.	Scrub desert	A	Typic Torriorthent
29	Peru	ET	*Parastrephia quadrangularis* (Meyen) Cabrera	Scrub desert	A	Typic Torriorthent
30	Spain	Csa	*Pinus halepensis* Mill, *Quercus coccifera* L.	Mediterranean forest	A	Typic Xerorthent

* the classification version employed corresponds to the one in use when the soils were first sampled (2nd edition, 1999).

The dataset embodies a good (although not exhaustive) variability of soils at the world scale, as 7 of the 12 USDA soil orders are present. The soils of alpine/polar climates (ET, in the southern hemisphere) were Entisols belonging to transition zones close to cold deserts and tundra-like vegetation, with dominance of steppe grasslands and shrubs. The Magellanic forest shared the same climate and presented a similarly poorly-developed soil. The soils from continental D climates (Dfb and Dfc) of boreal forests were often Alfisols with a cryic soil temperature regime developed on fine glacial sediments, where podzolization was impeded despite presence of conifers. In those cases, a non-diagnostic Bs horizon was often found and the soils were bisequal. Spodosols were instead found in Central Europe, developing on granite and granodiorite with no limitation to water movements. The soils of temperate climates (Cfb, Csb, Cfc) were divided among Entisols, Inceptisols and Mollisols. The occurrence of the Mollisol under beech vegetation could be linked to the calcareous parent material that, along with a seepage position, allowed the precipitation of secondary carbonates. In the Mediterranean environment (Csa), non-zonal Entisols were collected in erosion-prone sites, and a typic Terra Rossa (Rhodoxeralf) was also chosen. The soils of savannah (Aw and BSh climates) covered a wide range of pedogenic evolution, from the sandy Entisols of Sothern African desert borders to the Ultisols of Mali (collected on a toposequence with plinthite, petroplinthite and kandic horizons). The soils belonging to the Tropical formation (Cfa, humid subtropical climate) are represented by an Oxisol as well as by a non-zonal Inceptisol. Overall, conifers

dominated both in boreal and Mediterranean soils, while broad-leaved trees characterized savannahs and temperate forests.

As Boreal forest, Magellanic forest, Scrub desert and Steppe samples shared a common origin in either high elevation or high latitude environments (climates E and D), those samples are -in the following elaborations- presented together in the category of High elevation/latitudes ecosystems (HEL). The other samples belong to Temperate (TEM), Mediterranean (MED), Tropical (TRO) and Savannah (SAV) environments.

Soil samples (collected in previous campaigns carried out by the University of Torino, Miguel Hernández University of Elche, and State University of Londrina) were air-dried, sieved (2 mm) and stored at room temperature (RT) until laboratory analysis. Each sample was divided into four homogeneous subsamples. One was kept at RT, while 10 g of each subsample were placed in large ceramic crucibles (resulting thickness of ca. 1 cm) and heated for 30 min in a muffle furnace at a specific T: 200, 250 and 300 °C. We selected a 30 minutes heating time in agreement with recent studies (Araya et al., 2017, 2016; Varela et al., 2010). We focused on these Ts as existing literature reports the occurrence of major variations in soil physical properties in this range (DeBano, 2000; Negri et al., 2021).

4.2.2 Soil water repellency and aggregates characterization

Soil WR was evaluated by the Water Drop Penetration Time (WDPT) test on unheated and heated samples. To ensure comparability of results, WDPT was measured after keeping the samples in a vacuum chamber for 24 h. Room relative humidity was verified to be always around 30-50 % during WDPT testing (Beatty and Smith, 2010; Diehl et al., 2010; Papierowska et al., 2018). We employed a standard 0.1 mL dropper and recorded WDPT up to 4000 s. Four drops of distilled water were placed on the soil flattened surface.

Each soil sample (BULK at RT, 200 °C and 300 °C) was dry sieved so as to divide it in micro (<250 µm) and macro (>250 µm) size fractions. The relative contributions of the two fractions to the BULK soil was then calculated (MICRO and MACRO contents, %). Following Roldán et al. (1996), the MACRO fraction was placed on a 250 sieve and subjected to a rainfall simulation (height of 1 m, impact energy of 270 J rn^{-2}), which caused the loss of weak aggregates (WA). The soil remaining on the sieve was oven-dried, weighed and the amounts of coarse particles (> 250 µm) was determined to assess the proportion of resistant aggregates (RA, %) and deriving AS, as follows:

$$AS = \frac{RA}{(RA + WA)} \times 100\ (\%)$$

To account for the variability of the dataset in terms of WR and aggregation, and focus on T-induced variations (increments, instead of mere absolute values), we also employed normalized ratios (**Table 4.2**).

Table 4.2: Normalized ratios at rising Ts for WR, AS and RA.

Ratio	Calculation
WR 200/25	WR value at 200 °C / WR at RT condition
WR 300/200	WR value at 300 °C / WR value at 200 °C
WR 300/25	WR value at 300 °C / WR at RT condition
AS 200/25	AS value at 200 °C / AS at RT condition
AS 300/200	AS value at 300 °C / AS value at 200 °C
AS 300/25	AS value at 300 °C / AS at RT condition
RA 200/25	RA value at 200 °C / RA at RT condition
RA 300/200	RA value at 300 °C / RA value at 200 °C
RA 300/25	RA value at 300 °C / RA at RT condition

4.2.3 Soil physical and chemical analyses

Soil particle size distribution (PSD) was analyzed by the pipette method after dispersion with Na-hexametaphosphate (Gee and Bauder, 1986). Size classes were classified as: coarse sand (2000–200 μm), fine sand (200–50 μm), coarse silt (50–20 μm), fine silt (20–2 μm) and clay (<2 μm). Soil pH was evaluated in a 1:2.5 soil:deionized water suspension after 2 h shaking (Gee and Or, 2002).

Organic C (inorganic C removal by HCl) and total N were determined by dry combustion (Unicube CHNS Analyzer, Elementar, Langenselbold, Hesse, Germany) on BULK (OC, N, C/N), MACRO (OC_M, N_M, C/ N_M), and MICRO (OC_m, N_m, C/ N_m) soil fractions. Some related parameters were also calculated (**Table 4.3**).

Table 4.3: Parameters on OC distribution among size fraction and OC loss at 300 °C.

Parameter	Calculation
$OC_{M/m}$	OC_M/OC_m
MACRO LOSS	MACRO at RT - MACRO at 300 °C
Norm MACRO LOSS	MACRO LOSS / MACRO at RT ×100 (%)
OC LOSS	OC at RT - OC at 300 °C
Norm OC LOSS	OC LOSS / OC at RT ×100 (%)
OC_M LOSS	OC_M at RT - OC_M at 300 °C
Norm OC_M LOSS	OC_M LOSS / OC_M at RT ×100 (%)
OC_m LOSS	OC_m at RT – OC_m at 300 °C
Norm OC_m LOSS	OC_m LOSS / OC_m at RT ×100 (%)

On BULK samples, total Fe oxides were quantified by Na-Dithionite-citrate-bicarbonate (DCB) extraction (Mehra and Jackson, 1958). Ammonium oxalate (OXA) solution in the dark (Schwertmann, 1964) was employed to assess the contribution of poorly crystalline Fe oxides, and the organo-mineral complexes (Fe-OM pool) were isolated with a sodium pyrophosphate (PYRO) solution (Loeppert R.H., 1996). Fe contents in the solutions were determined by AAS (Thermo Scientific, iCE 3000 series). The different pools are addressed as Fe_{DCB}, Fe_{OXA} and Fe_{PYRO}, and Fe_{OXA}/Fe_{DCB} and Fe_{PYRO}/Fe_{DCB} were derived.
Selected samples, embodying the variability of the whole dataset in terms of climate, vegetation cover, lithology, were characterized more deeply in terms of OM composition. Belonging of the samples to specific soil orders was not considered, as the focus was posed on OM in these horizons.

4.2.4 Thermal analysis and analytical pyrolysis

Samples nr. 8 and 22 (HEL), 24 (MED) and 26 (TRO) and 14 (SAV) were characterized by a thermogravimetric analyzer coupled with a simultaneous differential scanning calorimetry (TGA-DSC 3+, Mettler Toledo, Greifensee, Switzerland). Small amounts (~25 mg) of finely ground soil samples were placed in alumina crucibles and heated in an oxidizing atmosphere (air flow rate of 100 mL min^{-1}) from 30 to 900 °C, with a ramp of 10 ◦C min^{-1}.The Ts corresponding to 50 % of mass loss (TG50) and energy release (DSC50) were calculated by integrating the DSC curves in the exothermic region.

Samples nr. 8, 11, 13 and 22 (HEL), 7 (TEM), 24 and 25 (MED), 26 (TRO), 14 and 20 (SAV) were subjected to analytical pyrolysis followed by gas chromatography mass spectrometry (Py-GC/MS). The Py-GC/MS analysis was performed following existing protocols (Jiménez-Morillo et al., 2016) with a double-shot pyrolyzer (Frontier Laboratories, model 3030, Fukushima, Japan) attached to a GC system (Shimadzu model GC2010). Finely ground samples (~20 mg) were placed in deactivated steel pyrolysis capsules (EcoCup, Frontier Laboratories) and introduced into a preheated microfurnace at (500 °C) for 1 min. The pyrolysate was then directly injected into the GC/MS for analysis. The gas chromatograph is equipped with a 30 m capillary column (Phenomenex Zebron-ZB-5HT). The GC oven temperature ramp was 50 °C for 1 min and then to 100 °C at 30 °C min^{-1}, from 100 °C to 300 °C at 10 °C min^{-1}, and at °C 300 °C for 10 min, with a total analysis time of 32 min. The carrier gas was He at a controlled flow of 1 mL min^{-1}. A mass selective detector (Shimadzu GCMS-QP2010 Plus) was used, and mass spectra were acquired at 70 eV ionizing energy. The compound assignment was done by single-ion monitoring (SIM) for the major homologous series, and by comparison with published data reported in the literature or stored in digital NIST 20 (Maryland, USA) and Wiley 7 (Weinheim, Germany) libraries. The *n*-alkane series was characterized by monitoring diagnostic ions (m/z 57 and 85).

4.2.5 Statistical analyses

RStudio (R version 4.0.2) was used for statistical purposes. The same statistical approach described in paragraphs 2.2.3 and 3.2.5 was adopted to perform groups comparisons in the selected T-range (ANOVA and Tukey-HSD, LMM), to compute correlation matrices, and operate and validate a clustering.

4.3 Results

4.3.1 Soil properties at room temperature

Table 4.4: Main soil physical properties of the analyzed samples at RT condition.

ID	Biome	C. Sand (%)	F. Sand (%)	C. Silt (%)	F. Silt (%)	Clay (%)	MACRO (%)
1	TEM	45	30	12	13	0	49.2
2	HEL	56	17	11	11	5	73.2
3	TEM	36	18	11	20	15	82.0
4	TEM	35	19	14	26	6	78.7
5	TEM	35	27	5	16	17	61.5
6	TEM	56	24	8	9	3	64.4
7	TEM	43	20	13	20	4	60.8
8	HEL	37	55	3	2	3	29.0
9	HEL.	21	35	17	18	9	68.6
10	HEL	16	38	15	21	10	67.8
11	HEL	17	20	36	19	8	57.5
12	HEL	5	37	28	21	9	57.5
13	HEL	87	5	3	3	2	91.2
14	SAV	17	78	1	1	3	48.1
15	SAV	74	21	1	2	2	46.9
16	SAV	76	14	4	3	3	55.2
17	SAV	92	5	1	1	1	68.7
18	SAV	65	13	11	7	4	51.9
19	SAV	51	21	11	10	7	55.9
20	SAV	53	26	9	8	4	58.1

21	HEL	57	21	16	4	2	44.4
22	HEL	66	23	8	1	2	35.7
23	MED	25	19	9	28	19	82.3
24	MED	7	20	7	31	35	91.5
25	MED	37	24	9	17	13	87.5
26	TRO	84	10	1	0	5	90.9
27	TRO	74	12	1	4	9	91.2
28	HEL	54	29	9	6	2	59.7
29	HEL	52	31	10	5	2	55.8
30	MED	60	19	9	7	5	85.1

Tropical forest samples (**Table 4.4**) presented the highest amount of coarse sand (mean=79 %, st. dev=7 %), while extremely low values were found in Mediterranean environments (mean=32 %, st. dev=22 %). Fine sand contents were mostly homogeneous (ca. 20-30 %), but in Tropical forest soils (mean=11 %, st. dev=1 %). Overall, sand dominated in Tropical and Savannah environments, and was less abundant in Mediterranean forest soils ($p<0.05$). Coarse silt was higher in High elevations/latitudes ecosystems and Temperate forests (mean values of 14 % and 10 %), while Tropical forest lacked this fraction (ca. 1 %). Fine silt was significantly more abundant in Mediterranean and Temperate forests respect to Savannah and Tropical ecosystems (over 17 % vs. less than 4 %, $p<0.01$). Silt dominated in Mediterranean, Temperate forests and High elevation/latitudes soils, and was abundant in Savannah and Tropical environments. Clay contents were significantly higher ($p<0.01$) in Mediterranean environments (mean=17 %) respect to High elevations/latitudes ecosystems and Savannah (mean values of 4 and 3 %).

The MACRO fraction significantly dominated ($p<0.001$) in Tropical (mean=91.0 %, st. dev=0.2 %) and Mediterranean environments (mean=86.6 %, st. dev=3.9 %), while it was less abundant in Savannah (mean=55.0 %, st. dev=7.3 %) and High elevations/latitudes ecosystems (mean=58.2 %, st. dev=17.5 %).

Table 4.5: Main soil chemical properties of the analyzed samples at RT condition.

ID	Biome	pH	OC ($g\ kg^{-1}$)	N ($g\ kg^{-1}$)	C/N	OC_M ($g\ kg^{-1}$)	$OC_{M/m}$	Fe_{DCB} ($g\ kg^{-1}$)	Fe_{OXA} ($g\ kg^{-1}$)	Fe_{PYRO} ($g\ kg^{-1}$)
1	TEM	4.6	18.3	1.1	16.6	14.5	0.67	7.4	3.5	3.9
2	HEL	7.2	94.5	4.9	19.3	77.9	1.04	7.4	2.6	1.4
3	TEM	4.1	52.1	3.6	14.5	48.8	0.93	17.5	5.2	9.2
4	TEM	7.7	64.3	5.3	12.1	68.2	1.07	9.4	1.9	0.8
5	TEM	7.4	56.3	4.8	11.7	56.1	1.12	17.8	1.4	1.7
6	TEM	6.4	107.7	8.9	12.1	119.2	1.13	14.5	6.0	1.4
7	TEM	6.5	57.0	5.6	10.2	45.7	0.79	21.3	6.1	0.6
8	HEL	4.0	10.3	0.8	12.9	14.2	1.61	1.7	1.1	1.1
9	HEL.	4.6	7.2	0.6	12.0	9.7	1.90	4.9	3.2	1.9
10	HEL	4.3	9.9	0.3	33.0	10.0	1.30	1.0	0.7	0.9
11	HEL	4.0	51.3	3.5	14.7	59.3	1.48	9.1	5.9	4.4
12	HEL	3.8	16.6	0.9	18.4	18.4	1.64	2.2	1.3	1.1
13	HEL	3.9	59.8	3.1	19.3	48.8	0.80	1.9	1.2	1.1
14	SAV	6.8	9.7	1.0	9.7	11.1	0.97	3.1	0.1	0.5
15	SAV	6.4	4.7	0.6	7.8	4.1	0.84	3.9	0.1	0.6
16	SAV	6.1	5.2	0.7	7.4	5.4	0.86	2.6	0.3	0.9
17	SAV	6.4	2.5	0.2	12.5	4.2	0.95	0.5	0.1	0.2
18	SAV	6.6	7.7	0.8	9.6	8.0	0.90	3.1	0.2	0.1
19	SAV	6.2	9.4	0.8	11.8	6.1	0.72	6.1	0.2	0.2
20	SAV	6.5	5.7	0.6	9.5	6.6	0.92	4.2	0.2	0.2
21	HEL	6.2	63.5	5.5	11.6	33.2	0.55	9.3	2.4	0.7
22	HEL	5.6	55.0	4.2	13.1	86.4	2.13	2.9	1.5	0.7
23	MED	8.0	48.9	2.8	17.5	38.4	0.86	4.8	0.4	0.4
24	MED	8.1	40.4	2.6	15.5	37.5	1.08	22.8	0.7	0.9
25	MED	8.4	81.6	5.0	16.3	72.5	1.52	2.6	0.7	1.3
26	TRO	5.5	21.6	1.7	12.7	17.4	0.66	4.9	0.4	2.8

27	TRO	5.6	19.4	1.5	12.9	21.8	0.72	18.8	0.9	2.4
28	HEL	5.9	67.7	4.0	16.9	81.3	1.68	2.3	0.9	0.4
29	HEL	5.7	44.7	2.8	16.0	44.5	1.18	2.2	0.8	0.3
30	MED	4.5	162.7	8.9	18.3	168.6	1.15	3.9	1.8	1.6

Soil pH (**Table 4.5**). was higher in Mediterranean than in High elevations/latitudes environments (mean= 7.2 vs. 5.0, $p<0.05$), while OC was significantly more abundant ($p<0.001$) in Mediterranean (mean=83.4 g kg^{-1}, st. dev= 55.8 g kg^{-1}), Temperate (mean=59.3 g kg^{-1}, st. dev=28.7 g kg^{-1}) and High elevations/latitudes environments (mean=43.7 g kg^{-1}, st. dev=28.8 g kg^{-1}) respect to Savannah samples (mean=6.4 g kg^{-1}, st. dev=2.6 g kg^{-1}). Total N showed an analogue and significant ($p<0.001$) distribution, while C/N only differed ($p<0.05$) from High elevations/latitudes environments to Savannah soils.

In general, OC_M appeared significantly lower in Savannah ecosystems (mean=6.5 g kg^{-1}, st. dev=2.4 g kg^{-1}) respect to the other samples ($p<0.01$). $OC_{M/m}$ was significantly lower in Savannah and Tropical environments than in High elevations/latitudes ecosystems (less than 0.88 vs. over 1.39, $p<0.05$).

Fe_{DCB} accounted for an average of 7.1 g kg^{-1} (st. dev=6.5 g kg^{-1}), and was significantly lower ($p<0.01$) in Savannah and High elevations/latitudes respect to Temperate forest soils (below 4 vs. over 14 g kg^{-1}). Fe_{OXA} was highly variable (from 0.1 to 6.1 g kg^{-1}), and presented a significant decreasing trend from Temperate to Mediterranean to Savannah ecosystems (three distinct levels of significance, $p<0.001$). Fe_{PYRO} was significantly lower in Savannah soils (mean=0.4 g kg^{-1}, st. dev=0.3 g kg^{-1}) respect to the other biomes ($p<0.001$). Fe_{OXA}/Fe_{DCB} significantly varied among the samples ($p<0.001$), peaking in High elevations/latitudes environments (mean=52.2 %, st. dev=14.9 %), followed by Temperate forest soils (mean=29.0 %, st. dev=14.2 %) and Savannah (mean=6.1 %, st. dev=3.4%). Fe_{PYRO}/Fe_{DCB} varied between 2.9 to 66.2 %, but without any statistically significant difference in mean groups.

4.3.2 Heat-induced changes in soil properties

WR, AS and abundance of RA were highly variable among the samples (**Figure 4.2**).

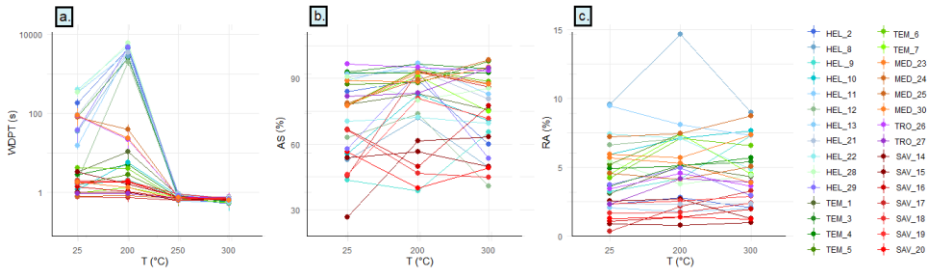

Figure 4.2: Average and standard deviation values for a) WDPT (s) (Y axis in log scale), b) AS (%) and c) RA. Colors assigned according to biome of belonging.

In general, most of the High elevations/latitudes environments soils were clearly separated from the others, with a high WR at RT, and development of a greater WR with heating to 200 °C (**Figure 4.2a**). The WR behaviour of the other soils was less intelligible, if not for the Savannah soils, with low and mostly unchanged WDPT values. The AS experienced a full range of variations: in some samples it remained unaltered, while in others it increased at 200°C or at 300°, and in others it decreased (**Figure 4.2b**). No demarcation by biome of belonging could be appreciated in AS. Heat-induced variations in RA (**Figure 4.2c**) were less evident than those in WR and AS. Still, Savannah soils were clearly separated from the others, with low and (mostly) constant values.

As no differentiation emerged, that would univocally identify samples belonging to a certain biome/soil type/vegetation cover as displaying a certain behaviour or tendency in WR and aggregation, the soils were thus clustered according to WDPT, AS and RA values (at RT, 200 and 300 °C) (**Figure 4.3a**). The agreement between biome of belonging and cluster division is displayed in **Figure 4.3b**.

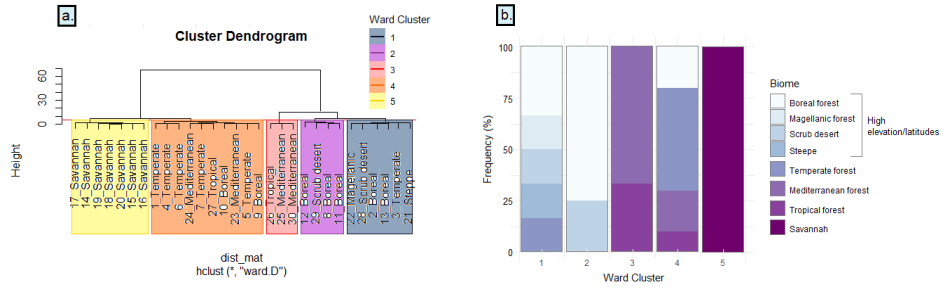

Figure4.3: a) Cluster dendrogram and b) composition of clusters according to soil biome.

Overall, the composition of clusters 1 and 2 was mostly related to High elevations/latitudes ecosystems (90 %), with one sample from Temperate forests (sample 3, developed under chestnut vegetation). Clusters 3 and 4 were for the most part (85 %) composed of Temperate, Mediterranean and Tropical forests soils, with two samples collected in High elevations/latitudes ecosystems

(sample 9 and 10, with very low WR values and OC contents). All Savannah soils were isolated in cluster 5.

As divided in clusters, heat-induced trends in WR, AS and RA are visible in **Figure 4.4**.

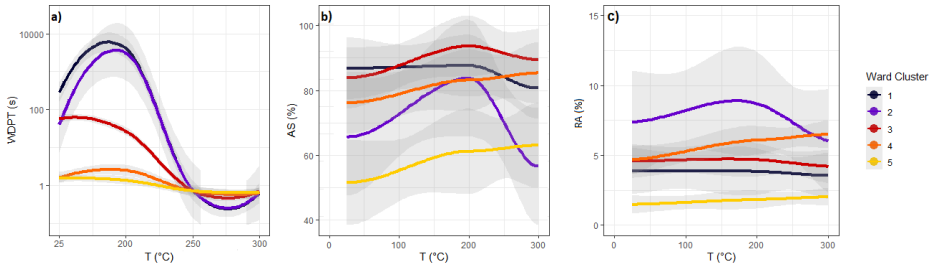

Figure 4.4: Evolution of a) WDPT (s), b) AS (%) and c) RA (%) alongside the selected T-range (25-300 °C). Soils are grouped according to cluster of belonging.

Clusters 1, 2 and 3 comprised samples whose WR (as measured by WDPT, **Figure 4.4a**) was, at RT, significantly greater ($p<0.001$) than soils of clusters 4 and 5 (mean values of more than 85 vs. less than 2 s). Heating T significantly affected WR ($p<0.001$), with an increase in WR at 200 °C for samples in clusters 1 and 2, and a generalized flattening of infiltration times (values lower than 1 s) for Ts of 250 °C or more. At the same time, ar RT, soils in cluster 1 presented significantly higher AS values ($p<0.01$, **Figure 4.4b**) respect to soils of cluster 5 (mean values of 87.0 % vs. 52.9 %). Upon rising Ts (AS significantly affected by T, $p<0.05$), trends were ambiguous for clusters 2 and 3 (increase at 200 °C and decrease at 300 °C), while samples in cluster 4 and 5 showed a heat-induced increase in AS values. Soils of cluster 5 also displayed significantly lower RA values ($p<0.01$, **Figure 4.4c**). The most noticeable change in RA was a non-significant, yet appreciable, increase from 25 °C to 300 °C in cluster 4 and 5.

In terms of variations, WDPT 200/25 was the greatest in cluster 2 ($p<0.001$, **Figure 4.5a**), followed by cluster 1, 4, 5, and 3 (in this last case with an average decrease). WDPT 300/25 and WDPT 300/200 were significantly higher in cluster 4 and 5 ($p<0.001$), and close to 1, signaling that soils in those groups hardly experienced any variations in WR (**Figure 4.5b and 4.5c**).

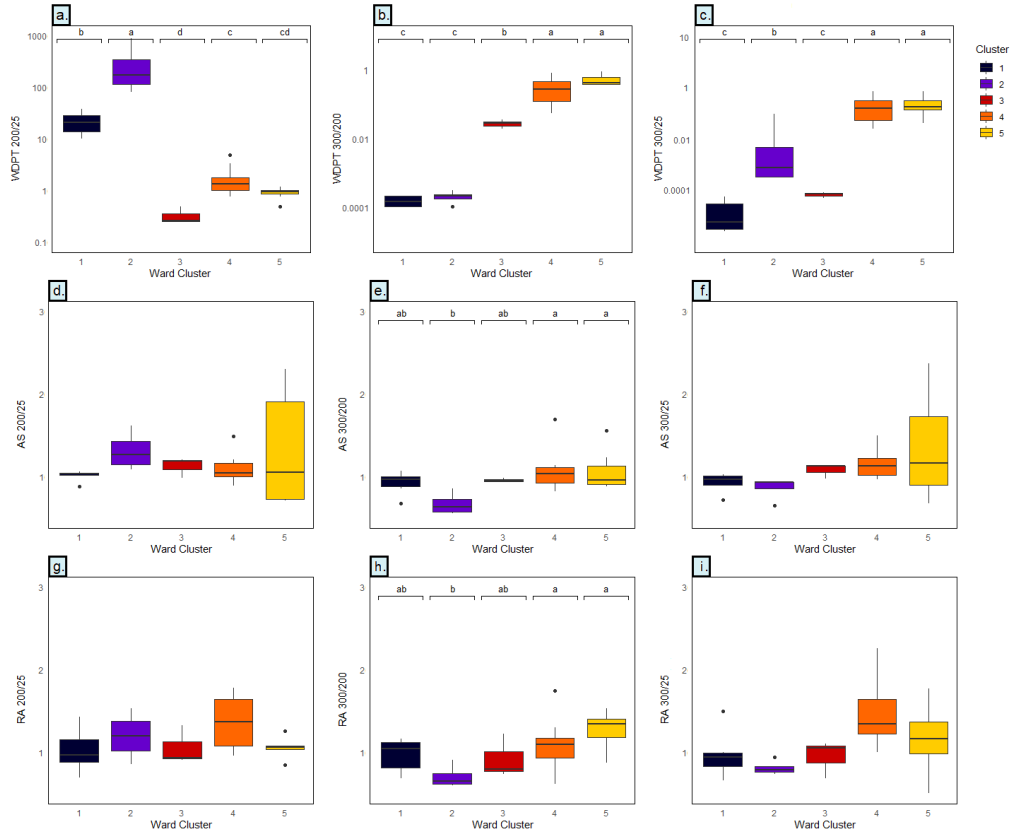

Figure 4.5: Boxplots depicting a) WDPT 200/25, b) WDPT 300/200, c) WDPT 300/25, d) AS 200/25, e) AS 300/200, f) AS 300/25, g) RA 200/25, h) RA 300/200, i) RA 300/25, all expressed as percentages (%).

In terms of variations, cluster 2 presented significantly lower AS 300/200 than cluster 4 and 5 ($p<0.05$, **Figure 4.5e**), indicating AS decrease with heating above 200 °C, while no significant difference emerged for AS 200/25 and AS 300/25 (**Figure 4.5d and 4.5f**). The relatively low contents of aggregates present within soils of cluster 5 (**Figure 4.4c**) may be responsible for the large variance in AS 200/25 and AS 300/25 values. Cluster 2 also had significantly lower RA 300/200 than cluster 4 and 5 ($p<0.05$, **Figure 4.5h**), while no significant differences were found for RA 200/25 and RA 300/25 (**Figure 4.5g and 4.5i**).

The rising-Ts induced several modifications in soil properties (**Figure 4.6**).

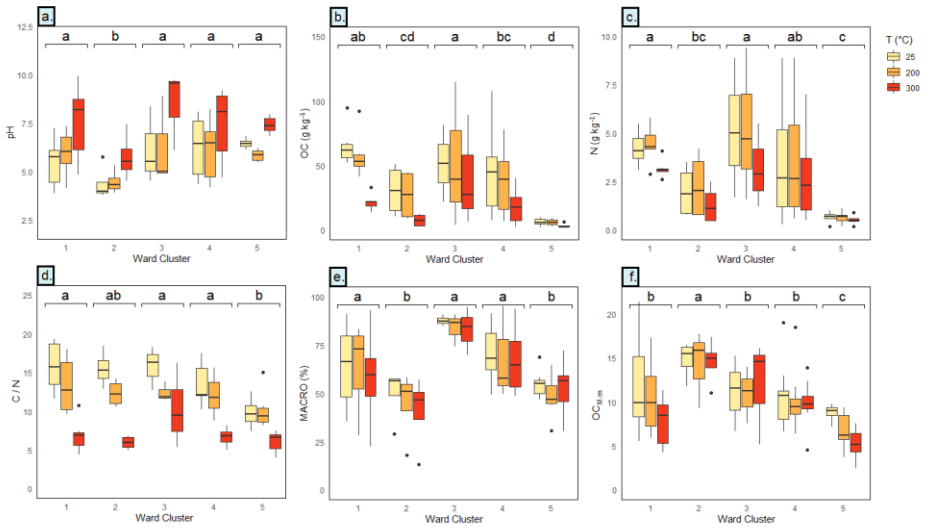

Figure 4.6: Boxplots depicting heat-induced changes in a) pH, b) OC (g kg^{-1}), c) N (g kg^{-1}), d) C/N, e) MACRO (%), f) $OC_{M/m}$, Samples are colored by T.

The pH values were significantly lower ($p<0.001$) for soils of cluster 2 and, in all clusters, the values increased for increasing Ts (**Figure 4.6a**), with significantly higher values at 300 °C ($p<0.001$; no detectable interaction effect, $p>0.05$). OC varied according to cluster of belonging (**Figure 4.6b**, $p<0.001$), and a clear decreasing trend emerged as Ts were rising, with significantly lower values at 300 °C ($p<0.001$; no detectable interaction effect, $p>0.05$). The N contents also varied (**Figure 4.6c**), with clusters 1 and 3 significantly more N-enriched than clusters 2 and 5 ($p<0.001$). No significant difference occurred upon growing Ts ($p>0.05$), but the trend mirrored that of OC. The C/N changed according to heating T (**Figure 4.6d**), with three distinct levels of statistical significance at each of the three tested Ts ($p<0.001$), and cluster ($p<0.01$).

Regarding the soil size fractions, a significantly lower content of MACRO emerged in clusters 2 and 5 respect to the others (**Figure 4.6e** , $p<0.001$). The heat-induced trends lacked any statistical significance ($p>0.05$) and, yet, decreasing mean MACRO values occurred in clusters 1 and 2 in contrast to oscillating/mostly unchanged mean MACRO values in clusters 3, 4 and 5. The $OC_{M/m}$ was significantly higher in cluster 2 ($p<0.001$), and was not significantly altered by increasing Ts (**Figure 4.6f,** $p>0.05$).

At 300 °C, OC LOSS was significantly lower in cluster 5 respect to 1 and 3 (**Figure 4.7a**) and, considering the abundance of starting OC, Norm OC LOSS (**Figure 4.7b**) was significantly greater in case of cluster 2, and lower for cluster 5, with intermediate values in case of other clusters. MACRO LOSS was higher in cluster 2, but did not significantly vary among the clusters (**Figure 4.7c,**

p>0.05). Considering the abundance of starting MACRO in the BULK soil, Norm MACRO LOSS was the greatest in cluster 2 (mean=22.85 %) and lowest in 5 (mean=5.25 %), but without any statistical significance (**Figure 4.7d,** p>0.05).

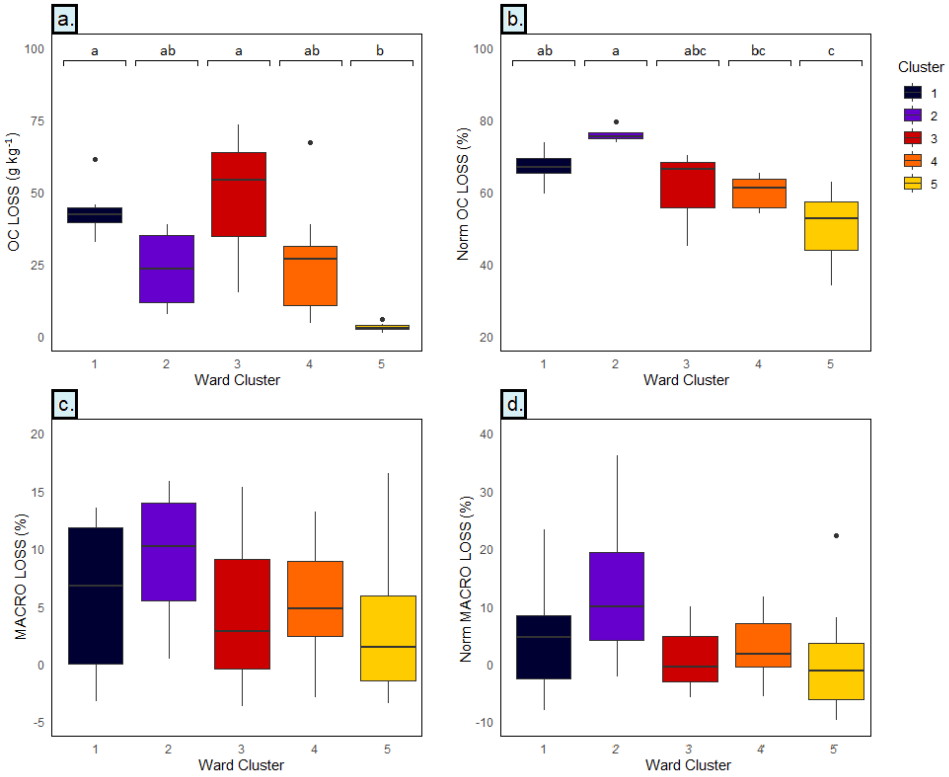

Figure 4.7: Boxplots with a) OC LOSS (g kg^{-1}) and b) Norm OC LOSS (%), c) MACRO LOSS $_{(\%)}$ and d) Norm MACRO LOSS (%) at 300 °C. Samples are colored by cluster of belonging.

At 300 °C, the amount of OC LOSS in MACRO and MICRO was not found to depend upon fraction type (p>0.05), but indeed significantly varied among clusters (**Figure 4.8a,** p<0.001). The lowest absolute values corresponded to cluster 5, which also showed the lowest OC contents. Norm OC LOSS was greater in cluster 2 than in 3 (p<0.001) and, according to fraction type, was significantly higher in MACRO than in MICRO (**Figure 4.8b**, p<0.001); this behavior was particularly evident for clusters 1 and 5.

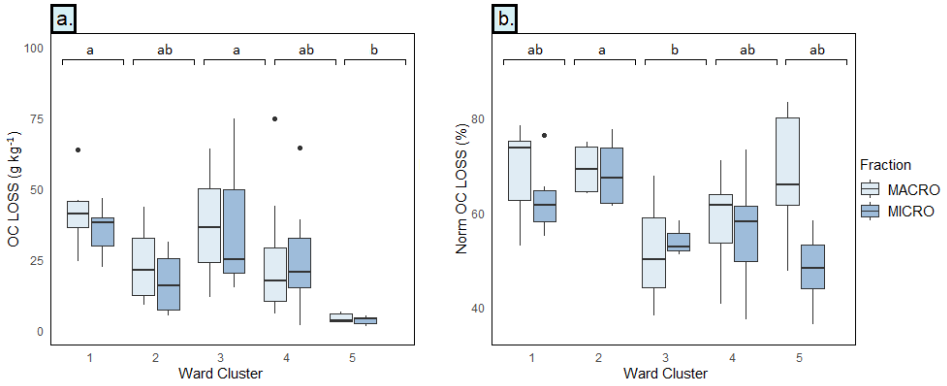

Figure 4.8: Boxplots with a) OC $LOSS_{MACRO}$ and OC $LOSS_{MICRO}$ (g kg^{-1}); b) Norm OC $LOSS_{MACRO}$ and Norm OC $LOSS_{MICRO}$ (%). Samples are colored by size fraction.

In the fractions, C/N varied according to fraction type (higher in MACRO than in MICRO, $p<0.01$), heating T (greater at 200 °C, **Figure 4.9a,** than at 300 °C, **Figure 4.9b,** $p<0.001$) and cluster of belonging ($p<0.001$).

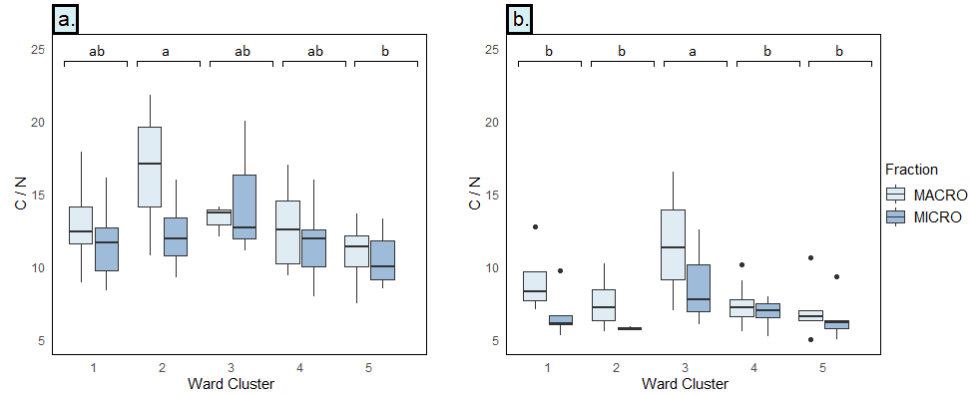

Figure 4.9: Boxplots depicting C/N values in soil fractions at a) 200 °C b) and 300 °C. Samples are colored by size fraction.

Evolution of Fe pools for rising-Ts is visible in **Figure 4.10**.

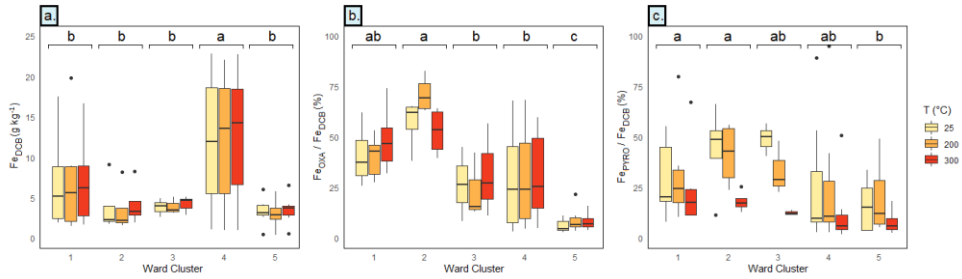

Figure 4.10: Boxplots depicting Fe pools a) Fe_{DCB} (g kg^{-1}), b) Fe_{OXA}:Fe_{DCB} (%) and c) Fe_{OXA}:Fe_{DCB} (%). Samples are colored by T.

Fe_{DCB} was significantly higher ($p<0.001$) in cluster 4, and was not affected by growing Ts (**Figure 4.10a**, $p>0.05$). Fe_{OXA}/Fe_{DCB} was not influenced by increasing Ts (**Figure 4.10b**, $p>0.05$) either, presenting significantly higher mean values in cluster 2 and 1, and extremely low concentrations in cluster 5 ($p<0.001$). The relative abundance of Fe-OM pool, Fe_{PYRO}/Fe_{DCB}, was significantly lower at 300 °C than at lower Ts (**Figure 4.10c**, $p<0.01$), and differed among clusters ($p<0.05$).

4.3.3 Modifications in soil OM composition

Thermal analyses (**Table 4.6**) revealed that, at RT, the highest TG50 values corresponded to cluster 5 and the lowest corresponded to cluster 2, while differences were less marked in DSC50. Higher values, both in TG50 and DSC50, were detected for increasing heating. At 300 °C, the highest absolute TG50 values corresponded to samples of clusters 4 and 5, while DSC50 was higher in cluster 2.

Table 4.6: Thermal indices as determined by TGA-DSC.

		TG50 (°C) Ward Clusters					DSC50 (°C) Ward Clusters				
T (°C)	**Fraction**	**1**	**2**	**3**	**4**	**5**	**1**	**2**	**3**	**4**	**5**
	MICRO	338	316	345	356	367	369	352	365	353	368
25	MACRO	341	328	357	352	364	378	363	371	355	358
	BULK	339	321	347	356	368	374	345	368	355	361
	MICRO	431	347	359	369	383	385	363	374	369	380
200	MACRO	378	328	363	371	385	394	375	374	364	375
	BULK	382	360	366	372	384	395	370	369	363	389
	MICRO	431	407	426	447	442	436	449	397	439	433
300	MACRO	428	431	436	444	445	434	454	397	449	416
	BULK	428	420	441	440	440	436	454	428	422	425
		22	8	26	24	14	22	8	26	24	14
		Samples					Samples				

Analytical pyrolysis revealed the relative abundance of *n*-alkane series in the soil samples (**Figure 4.11**). Increasing T induced the fragmentation of larger compounds. Hardly any compounds appeared above C-29/C-30 above 200 °C, and only series shorter than C-24 were detected at 300 °C.

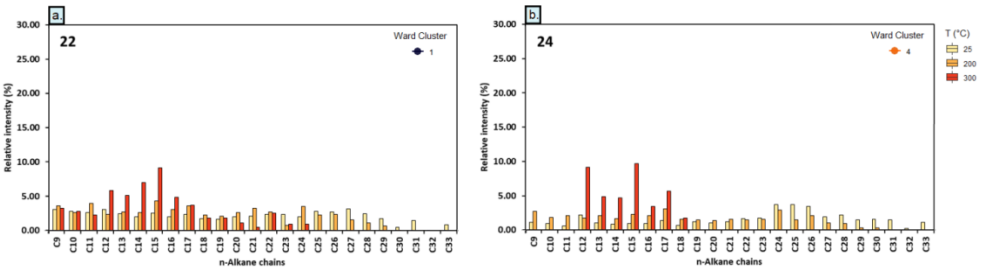

Figure 4.11: Relative abundance of fatty acids as identified in the pyrograms of samples a) 22 and b) 24. Bar colors assigned by T.

The composition of the fatty acids varied among the clusters (**Table 4.7**). At RT, increasing contents of C>20 was detected from clusters 1 to 4. Greater Ts lead to an increase in the relative abundance of short *n*-alkane chains, while a too weak signal was detected in the samples belonging to cluster 5 to perform the evaluation.

Table 4.7: Composition (%) of *n*-alkans in the studied soils, as divided by series length (C</> 20).

		Abundance (%) in Ward Clusters				
T (°C)	**Chains**	**1**	**2**	**3**	**4**	**5**
25	C<20	60.17	58.67	49.72	34.73	-
	C>20	39.83	41.33	50.28	65.27	-
200	C<20	83.72	74.59	63.92	58.57	-
	C>20	16.28	25.41	36.08	41.43	-
300	C<20	84.28	51.41	65.55	87.02	-
	C>20	15.72	48.59	34.45	12.98	-

4.4 Discussion

4.4.1 How do soils from different biomes respond to rising Ts?

Samples belonging to diverse environments were found to differ in several soil properties. Alfisols of Mediterranean forests were characterized by the greatest contents of clay (**Table 4.4**) and Fe_{DCB} (**Table 4.5**). Abundant Fe oxides were also found in Inceptisols of Tropical and Temperate forest soils, and OC contents were extremely low only in Savannah ecosystems, both in Ultisols and Entisols. One of the most striking differences regarded OM composition (**Figure 4.11, Table 4.6**). At RT, a variable abundance of long-chained *n*-alkanes was detected (**Table 4.7**), with soils of High elevation/latitudes presenting a greater content of short-chained fatty acids than samples belonging to other biomes. This differentiation is probably inherited by the vegetation present at each site and, albeit conifers dominated both in Boreal and

Mediterranean forests (**Table 4.1**), the specific OM composition resulting from litter transformations did not originate a similar abundance of alkanes (**Table 4.7**). The soils were also characterized by abundant labile OM structures, as deduced by DSC-derived Ts (**Table 4.6**) in the range of 200-375 °C (Merino et al., 2015). In general, OM was not less labile in either the MACRO or MICRO fraction, but in Savannah soils OM displayed the greatest recalcitrance (high TG50 values) and extremely low C/N values (pointing to a specific turnover).

Upon rising Ts, the samples did not univocally respond to the heating treatment (**Figure 4.2**). From 25 to 200 °C, minor changes were detected in OC content (**Figure 4.6b**) and pH (**Figure 4.6a**). Yet, the occurrence of OM thermal alteration was underlined by the characterization of organic compounds. Significantly lower C/N values were observed in the range 25-200 °C (**Figure 4.6d**), as a consequence of concentration of heat-resistant N-rich organic structures (González-Pérez et al., 2004; Mastrolonardo et al., 2015). The thermal analysis (**Table 4.6**) evidenced a migration to DSC values in the 375-475 °C region, corresponding to recalcitrant compounds (Merino et al., 2015). TG50 and DSC50 values did not clearly discriminate one size fraction from the other (no systematically lower/higher values in either MACRO or MICRO fractions). A similarity in Ts may derive from a homogenization effect, with migration of micro-within-macro to the micro size fraction as a consequence of macroaggregates disaggregation. This shift is expected because fire-induced aggregate breakdown has been observed to cause coexistence of partially oxidized organic compounds with OM structures that were –in a pre-heating condition– occluded within macroaggregates (Mastrolonardo et al., 2015) and incorporation of charred material into multiple soil sieve fractions (Nocentini et al., 2010). Changes in OM composition for Ts up to 200 °C were confirmed also by analytical pyrolysis (**Figure 4.11, Table 4.7**), with shifts towards low-medium molecular weight compounds, i.e. thermal cracking. This phenomenon has already been documented upon soil heating (Badía-Villas et al., 2014). In parallel, the amount of organo-mineral complexes underwent minor and non-significant changes (**Figure 4.10c**), suggesting resistance at this temperature.

At 300 °C, OC contents were significantly lower and pH values significantly higher (**Figure 4.6a and 4.6b**), testifying the base cations release associated to OM oxidation (Merino et al., 2018). Soil OM transformation was not homogeneous across biomes. Savannah soils resulted much more resistant to OM oxidation than High elevation/latitudes ecosystems in terms of OC losses (**Figure 4.7a**), and OC losses proportional to OC contents (Norm OC LOSS, **Figure 4.7b**). This might be due to a different association with the mineral phases or to distinct OM composition (or both). To address the first possible explanation, we should consider that High elevations/latitudes and Savannah ecosystems were not different in terms of clay content or Fe oxides contents (**Table 4.5**), and presented examples of different soil types (Entisols and Ultisols in that Savannah, while Entisols, Alfisols and Spodosols in High elevations/latitudes ecosystems). Therefore, we are prone to hypothesize that, at

least when comparing soils originated in these two biomes, OC losses primarily occurred as a function of initial OM composition.
At 300 °C, TG50 values were above 400 °C in all the samples, in line with presence of aromatic compounds (aromaticity above 40 %) (Merino et al., 2018). Still, it should be clarified whether the thermal evolution lead to similar/dissimilar final products. On one side, the C/N ratio (significantly different at RT, 17.0 vs. 9.8 in High elevations/latitudes environments vs. Savannah soils) underwent a systematic decrease (**Figure 4.6d**), that resulted in non-different final mean values (at 300 °C: 7.3 vs. 6.2 in High elevations/latitudes environments vs. Savannah soils). On the other side, a wide variability in C</>20-alkane contents (**Table 4.7**) was observed at high-T (st.dev.= 11.7 % for RT, st.dev.= 16.8 % for 300 °C). High heat intensities are, in the literature, reported to cause the (almost) complete loss of chromatograph peaks, with possible permanence of C-29-sterols (Badía-Villas et al., 2014). By direct inspection of the fatty acids composition (**Figure 4.11**), we observed a T-induced enrichment in C-12<*n*<C-18 alkanes in a sample (nr. 24) belonging to the Mediterranean environment, while a wider distribution in chain-length (C-9<*n*<C-24) corresponded to the sample (nr. 22) belonging to High elevations/latitudes. This suggests that OM oxidation likely occurred along distinct pathways, originating different products in soils representative of distinct environments.
Heat-induced OC losses have been documented to be not-homogeneously distributed among soil size fractions (Girona-García et al., 2018). At 300 °C, we did not find OC losses to differ in MACRO and MICRO (**Figure 4.8a**), but indeed normalized OC losses were lower in the MICRO than in the MACRO fraction (**Figure 4.8b**). This different degree of OM oxidation might be due to presence of particulate OM in the MACRO fraction (Six et al., 2002), or it could be induced by the stabilization effect exerted by minerals -with less accessible organic compounds- and lower O_2 concentrations in soil micro-pores (Mastrolonardo et al., 2014). The C/N values differed in the fractions (higher in MACRO, **Figure 4.9b**), but no unequivocally higher/lower TG50 and DSC50 values emerged in either MACRO or MICRO at 300 °C (**Table 4.6**). Probably, if differences existed, they were too small and close to the detection limit of the instrument.

The evolution of Fe forms was far less affected than soil organic compounds by rising Ts, with no differentiation among biomes, and only a general marked decrease in the Fe-OM pool (**Figure 4.10c**).

4.4.2 Which factors affect WR at rising Ts?

According to the classification by Bisdom et al. (1993), at RT High elevations/latitudes soils were on average slightly (cluster 2, 5<WDPT<60 s) and strongly water repellent (cluster 1, 60<WDPT<600 s), and became severely (cluster 2, 600<WDPT<3600 s) and extremely (cluster 1, WDPT>3600 s) water repellent at 200 °C (**Figure 4.4a**). Half of Mediterranean and Tropical forest soils (cluster 3) were strongly water repellent at RT and slightly water repellent

at 200 °C. The remaining Mediterranean and Tropical forest soils plus the most part (83 %) of Temperate forest soils (cluster 4), and Savannah soils (cluster 5) were wettable both at 25 and 200 °C.

To compare these data with the literature, we should consider that strongly and extremely WR superficial soil horizons were found in subartic continental climates (boreal forests of Canada) under conifer vegetation, soils that lost WR after wildfire occurrence (Elmes et al., 2019). Unaffected infiltration rates were conversely documented in soils in North-Eastern South Africa (Kruger National Park, with a hot semi-arid climate) after fire occurrence (Strydom et al., 2019), and slightly hydrophobic A horizons (CA in the range of 40-80°) characterized the soils of a humid subtropical region in Brazil (Vogelmann et al., 2010). In Israel (hot-summer Mediterranean climate) the measurement of soil WR in areas with *Pinus halepensis* and shrubs revealed that, despite inter-annual seasonal variability, hydrophobicity was lost as a consequence of recurrent fires (Keesstra et al., 2017).

In our case, regardless of the hydrophobicity displayed up to 200 °C, all soils became wettable above this threshold. The tested heating treatment seems therefore sufficient to cause WR loss in strikingly different soils, which is not what has always emerged in the literature. A longer heating time-period (ca. 150 minutes above 250 °C) has been found to induce a drastic decrease in hydrophobicity in surface mollic horizons (from NW Spain) that were initially very repellent (Badía-Villas et al., 2014), while heating at 300 °C (for 10 minutes) a topsoil developed under Eucalypt forest cover was documented to increase WR (Atanassova and Doerr, 2011).

The most relevant variables influencing WR at the three selected Ts are displayed in **Figure 4.12**.

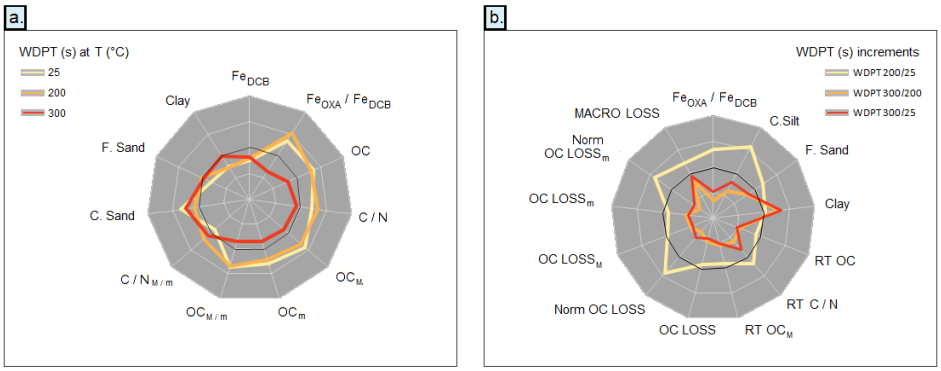

Figure 4.12: Radarplots with correlation coefficients between selected variables and a) WDPT (s) and b) WDPT increments, at 25-200-300 °C. Black solid line for R=0, grid pace=0.5.

Soil WR as measured by WDPT (**Figure 4.12a**) showed a positive correlation with the degree of Fe oxides crystalline disorder (Fe_{OXA}:Fe_{DCB}), a relationship

which became stronger shifting from RT (R=0.340, p=0.06) to 200 °C (R=0.517, p<0.01). At the same time, WR variations (**Figure 4.12b**) were negatively related to this parameter from 200 to 300 °C (R=-0.656, p<0.001) and also from RT to 300 °C (R=-0.656, p<0.001). This underlines that, despite abundance of such a Fe pool might favor WR build-up, soils with greater proportions of poorly crystalline Fe oxides (i.e. High elevation/latitudes ecosystems) were the ones experiencing the greatest WR loss. Availability of surfaces seems therefore a WR leading factor, but it's not predisposing for the establishment of strong enough bonds.
Regarding soil texture, WDPT values were positively related to coarse sand contents at RT (R=0.353, p=0.06), and WR increments from RT to 200 °C were higher where coarse silt was abundant (R=0.580, p<0.001). Variations up to 300 °C were negatively related to coarse silt contents (R=-0.412, p<0.05 for WDPT 300/200 vs. coarse silt) and weakly positively related to clay contents (R=0.327, p=0.08 for WDPT 300/25 vs. clay), implying WR build-up was favored by dominance of coarse silt over clay.

Literature often reports cases of positive relationship between OC contents and WR (Girona-García et al., 2018), with heat-induced OM loss triggering a decrease in WR (Jordán et al., 2011). In this study, a weak positive relationship between WDPT and OC emerged at RT (R=0.364, p<0.05), stronger when considering only the OC present in the MACRO fraction (R=0.419, p<0.05). Yet, soils of Temperate, Mediterranean and Tropical environments (cluster 3 and 4) presented the same RT OC content as High elevation/latitudes ecosystems (cluster 1) and did not display WR build-up (no correlation between WDPT 200/25 and RT OC). In the literature, other Brazilian soils (located in similar tropical climates) have displayed only weak relationships with OM content (Vogelmann et al., 2010), as did some soils developed in Mediterranean ecosystems (Zema et al., 2021). In this case, soils of cluster 4 were, for once, characterized by the greatest content of clay (ca. 11 %) and Fe oxides (average over 13 g kg^{-1}), hinting at the relevant role played by organo-mineral associations (other than just OM loads) in boosting WR.

OC losses were greater for soils that developed and lost WR (R=-0.533 and p<0.01 for WDPT300/200 vs. OC LOSS, R=-0.640 and p<0.001 for WDPT300/200 vs. Norm OC LOSS), suggesting that OM presence favored WR occurrence, but OM itself was not intimately stabilized onto the mineral phase.
To motivate the small OC losses of Savannah soils (that did not present nor developed WR, and whose OM was recalcitrant since RT), we should consider that a great hydrophobic character of the OM would modulate a distinct association with the mineral phase, with hydrophobic interaction prevailing over electrostatic interaction, the latter one of which is highly sensitive to increasing pH (Vindedahl et al., 2016).
In addition to OC contents, OM quality is also involved in determining WR extent. OM derived from conifer vegetation typical of Boreal forests was found to possess a specific abundance of *n*-alkanes, with chain length inversely related

to soil hydrophobicity (**Table 4.7**, C>20 increasing from cluster 1 to 4). Composition of *n*-alkanes is, in Piceoideae (*Picea abies*), similar but not totally identical to that of Pineoideae (*Pinus sylvestris*) (Maffei et al., 2004) and, while *Pinus pinea* has been found to promote soil WR -more than other vegetation types, eucalypts and holm oaks, typical of similar environments- (Zavala et al., 2014), other Mediterranean pines (*Pinus nigra*) have been found to trigger little soil WR (Zema et al., 2021).
All in all, this evidence leads to hypothesize that chains shorter than C-20 might be fundamental in ruling WR formation and, while series of C-5<*n*<C-10 alkanes are known to bind weakly with mineral surfaces (translating into a wettable matrix), the affinity of palmitic acid (C-16) for quartz surfaces has been established, with induction of extreme soil hydrophobicity (Uddin et al., 2017). We should then consider that, despite heating at 300 °C did not negatively affect the pool of C-10<*n*<C-16 alkanes, the consistent decrease in OC was likely sufficient to induce WR loss.

4.4.3 Which factors affect aggregate composition and stability at rising T?

A steady (but minor) decrease in the abundance of MACRO (i.e. the size fraction between 2 mm and 250 µm, subjected to aggregation measurements) was detected in most of the studied soils (**Figure 4.6e**). Similarly, increase in micro-aggregates has been documented after high-severity fire (Andreu et al., 2001; Varela et al., 2010), or in the 0.25-0.5 mm fraction (0-1 cm topsoil) after prescribed burning application (Girona-García et al., 2018). The increase in MICRO particles could be considered as a predisposing factor for soil erosion (Fox et al., 2007).

In general, results on soil aggregation (**Figure 4.4b and 4.4c**) showed less marked variations than WR (**Figure 4.4a**) in the selected T-range. A positive correlation has been often observed between WR and AS in either unburnt (Benito et al., 2003; Chenu et al., 2000) or burnt soils (Arcenegui et al., 2008; Jordán et al., 2011; Mataix-Solera and Doerr, 2004). Here, WR was not found to univocally correlate to AS ($R<0.400$ and $p>0.05$ at all the selected Ts). Still, above 200 °C WR variations were positively related to AS variations ($R=0.404$ and $p<0.05$ for WDPT 300/200 vs. AS 300/200, $R=0.452$ and $p<0.05$ for WDPT 300/200 vs. RA 300/200), implying that those soils which lost WR for Ts>200 °C were also negatively affected in terms of aggregation.

This variable behaviour is not anomalous, as some studies have deemed soil structure to be unaffected with heating Ts below 220 °C (Soto et al., 1991), while according to others aggregation can be lost even below 200 °C for rapid water-vapor ejection from aggregates (Albalasmeh et al., 2013).

The most evident (and detectable) heat-induced trend here observed was a decrease in AS (**Figure 4.5e**) and RA (**Figure 4.5h**) for some High elevations/latitudes soils (cluster 2). In the literature, lower AS values have been documented in alpine soils after fire occurrence (Vacchiano et al., 2014) and, in

subalpine climates, the presence of unaltered AS values in burnt vs. prescribed-fire-affected soil samples has been interpreted as resulting from inorganic cementing agents (since OM decreased with fire occurrence) (Girona-García et al., 2018).
The only soils that clearly isolated from the others, with a strikingly different behavior (low AS and low RA, unaltered by T), were Savannah samples (cluster 5).

The most relevant variables influencing AS at the three selected Ts are displayed in **Figure 4.13**.

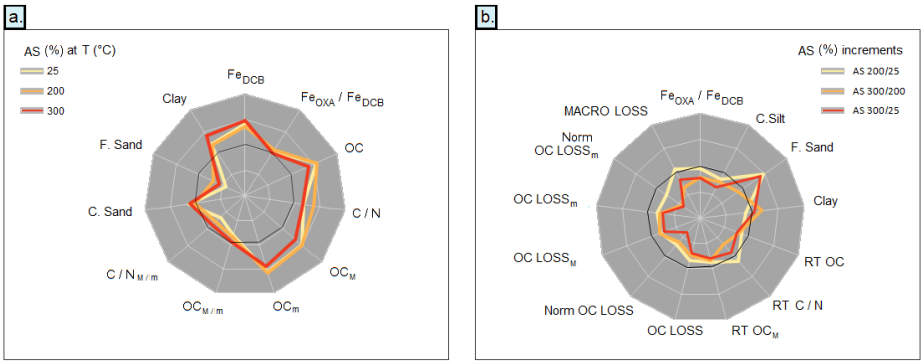

Figur4.13: Radarplots with correlation coefficients between selected variables and a) AS (%) and b) AS increments, at 25-200-300 °C. Black solid line for R=0, grid pace=0.5.

Soil AS was tightly related to Fe oxides abundance (**Figure 4.13a,** R>0.400 and p<0.05 for all Ts), while AS variations were not directly influenced by Fe_{DCB} contents (**Figure 4.13b,** -0.200<R<0.100 and p>0.05 for all Ts). Still, the group of soils with the highest Fe_{DCB} contents (**Figure 4.10a,** cluster 4) -comprising Mediterranean, Tropical and Temperate forest samples- showed an increase in the proportion of resistant aggregates with heating (RA 300/25, **Figure 4.5i**). In such environments (especially in Mediterranean ones) a greater aggregation has been observed both after heating treatments (Guerrero et al., 2001) and direct fire occurrence (Arcenegui et al., 2008; Ubeda and Bernia, 2005). Therefore, despite these soils presented the same OM content as cluster 1 and 2 (**Figure 4.6d**) and experienced an analogue T-induced OC loss (**Figure 4.7a**), the cementing effect of crystalline and poorly-ordered Fe oxides that has vastly been established (Barthès et al., 2008) seems more pronounced. The different Fe oxides crystalline degree in High elevations/latitudes samples (cluster 1 and 2) vs. more developed soils (cluster 4 and 5) (**Figure 4.7b**) was not related nor to overall AS values (**Figure 4.13a,** R ca. 0 and p<0.05 for all Ts) nor to AS variations (**Figure 4.13b,** -0.250<R<0 and p>0.05).

AS was found to correlate positively and significantly with abundance of MACRO, a correlation that grew stronger for rising Ts (from R=0.475 to R=0.664 at 300 °C, p<0.01). Greater fine sand contents triggered a weaker

aggregation (**Figure 4.13a**), with a significant effect at 25 °C and 300 °C ($R<-0.400$ and $p<0.001$). Greater clay contents exerted an opposite role at all Ts ($R>0.400$ and $p<0.05$), in line with evidences reported in the literature (Thomaz, 2021).

OC content was positively and significantly related to AS at all Ts ($R>0.500$ and $p<0.01$ at RT and 200 °C, $R<0.400$ at 300 °C), regardless of the distribution among size fractions ($OC_{M/m}$) (**Figure 4.13a**). Heating-induced loss of OM has been reported to cause a decrease in AS (Mataix-Solera et al., 2002; Soto et al., 1991). In our case, RT-relative OC losses (Norm OC LOSS) were inversely related to AS increments from RT to 300 °C ($R=-0.626$ and $p<0.001$), underlining the contribution of organic compounds in determining soil structure up to 200 °C. this phenomenon was not always visible, possibly as a result of the starting OM composition. Indeed, the oscillating AS of High elevations/latitudes soils of cluster 2 (higher at 200 °C, lower at 300 °C, **Figure 4.4b**) might be motivated with the condensation of hydrophobic organic compounds on the surface of aggregates (in line with the WR tendencies of those samples, **Figure 4.4a**), increasing their resistance (Fox et al., 2007; Terefe et al., 2008). This did not happen in all the samples, that experienced a lower T-induced WR build-up or with a different organo-mineral composition.

CHAPTER 5

Conclusions

Chapter 2:

In alpine soils, OM quantity and quality were the main drivers of hydrophobicity at RT condition. Upon heating, the samples displayed extremely different wettable behaviors, with or without T-induced WR build-up (maximized at 200 °C). This happened mainly in relation to content and composition of OM, particle size distribution and abundance of serpentine and Fe oxides. Regardless of the initial presence of hydrophobicity, WR was dramatically lost above 200 °C. This phenomenon was mainly attributed to heat-induced OM de-sorption from mineral particles, with increase in the negative surface charge of mineral surfaces linked to a systematic increase in pH. The deriving OM-free surfaces of soil particles would eventually interact with water molecules, leading to a super-hydrophilic behavior in soil. Possibly because of a different OM retention on mineral phases, alpine soils experienced the disruption of repellent organic coatings at relatively low Ts (lower than thresholds generally reported in the literature).

Chapter 3:

The thermal transformation of soil Fe species was found to be primarily directed towards oxidative processes. Yet, it is possible that high OM loads, especially when coupled with a dominant aromatic character, could provide the proper onset for reducing conditions.

The conversion of soil Fe phases can considerably impact OC dynamics and the fate of other elements, thereby affecting ecosystems as a whole. We observed that, in alpine soils, Ts up to 300 °C seem not to promote the formation of Fe oxides with a greater crystalline order, notwithstanding the pre-existing differences in native Fe forms and soil OM. Crystalline Fe oxides are expected to associate more permanently with OM than poorly ordered Fe phases which, still, are able to provide stabilization for a consistent OM amount by their high surface area and reactivity. The structural heat-induced changes borne by mineral phases (synthesis of defect-rich Fe forms) and OM (enrichment in condensed and aromatic compounds, at least for PINE samples) could have potentially promoted the stabilization of the remaining OM. Nonetheless, OM was observed to be highly dispersible at the high pH values resulting at 300 °C, such that thermally altered OC might be weakly retained on mineral phases in an after-fire natural scenario.

Chapter 4:

Up to 300 °C, the thermal evolution of topsoils belonging to a wide variety of natural environments followed different pathways. T-induced WR build-up occurred only for some of the analyzed samples (and was maximized at 200

°C), mainly in case of soils belonging to High elevation/latitudes ecosystems. Soils belonging to Temperate, Mediterranean and Tropical forest soils did not experience increase in WR (possibly due to a larger number of surfaces available for bonding both with OM and water molecules), and Savannah soils were always wettable, at RT condition as well as up to 300 °C. Tendencies in aggregation were not as distinct between biomes, with only Savannah soils clearly separated from the others (few RA and no AS loss upon rising Ts).
Soil WR was influenced, although not proportionally, to abundance of clay, sand, poorly crystalline Fe oxides and OM. The role of conifers in triggering WR also emerged, but was not strictly associated to WR formation (distinct abundance of *n*-alkanes series in Boreal vs. Mediterranean forests). OM transformations occurred already when shifting from 25 to 200 °C, and then from 200 to 300 °C, with a clear increase in OM recalcitrance and greater TGA/DSC-derived values (taking distinct pathways in soils belonging to different biomes). Soils of savannah environments experienced the lowest OC losses, possibly as a different starting OM composition also dictated specific interactions with the mineral phase, leading to not-homogeneous OC losses among samples.

REFERENCES

Abney, R.B., Jin, L., Berhe, A.A., 2019. Soil properties and combustion temperature: Controls on the decomposition rate of pyrogenic organic matter. Catena 182, 104127.

Albalasmeh, A.A., Berli, M., Shafer, D.S., Ghezzehei, T.A., 2013. Degradation of moist soil aggregates by rapid temperature rise under low intensity fire. Plant and Soil 362, 335–344.

Amézketa, E., 1999. Soil aggregate stability: a review. Journal of sustainable agriculture 14, 83–151.

Andreu, V., Imeson, A.C., Rubio, J.L., 2001. Temporal changes in soil aggregates and water erosion after a wildfire in a Mediterranean pine forest. Catena 44, 69–84.

Aquilanti, G., Giorgetti, M., Dominko, R., Stievano, L., Arčon, I., Novello, N., Olivi, L., 2017. Operando characterization of batteries using x-ray absorption spectroscopy: advances at the beamline XAFS at synchrotron Elettra. Journal of Physics D: Applied Physics 50, 74001.

Araya, S.N., Fogel, M.L., Berhe, A.A., 2017. Thermal alteration of soil organic matter properties: a systematic study to infer response of Sierra Nevada climosequence soils to forest fires. Soil 3, 31.

Araya, S.N., Meding, M., Berhe, A.A., 2016. Thermal alteration of soil physico-chemical properties: a systematic study to infer response of Sierra Nevada climosequence soils to forest fires. Soil 2, 351–366.

Arcenegui, V., Mataix-Solera, J., Guerrero, C., Zornoza, R., Mataix-Beneyto, J., García-Orenes, F., 2008. Immediate effects of wildfires on water repellency and aggregate stability in Mediterranean calcareous soils. Catena 74, 219–226.

Atanassova, I., Doerr, S.H., 2011. Changes in soil organic compound composition associated with heat-induced increases in soil water repellency. European Journal of Soil Science 62, 516–532.

Bachmann, J., Horton, R., Van Der Ploeg, R.R., Woche, S., 2000. Modified sessile drop method for assessing initial soil--water contact angle of sandy soil. Soil Science Society of America Journal 64, 564–567.

Badía-Villas, D., González-Pérez, J.A., Aznar, J.M., Arjona-Gracia, B., Martí-Dalmau, C., 2014. Changes in water repellency, aggregation and organic matter of a mollic horizon burned in laboratory: Soil depth affected by fire. Geoderma 213, 400–407.

Badía, D., Aguirre, J.A., Martí, C., Márquez, M.A., 2013. Sieving effect on the intensity and persistence of water repellency at different soil depths and soil types from NE-Spain. Catena 108, 44–49.

Badía, D., Martí, C., 2003. Plant ash and heat intensity effects on chemical and physical properties of two contrasting soils. Arid Land Research and Management 17, 23–41.

Baldock, J.A., Smernik, R.J., 2002. Chemical composition and bioavailability of thermally altered Pinus resinosa (Red pine) wood. Organic

Geochemistry 33, 1093–1109.
Barthès, B.G., Kouakoua, E., Larré-Larrouy, M.-C., Razafimbelo, T.M., de Luca, E.F., Azontonde, A., Neves, C.S.V.J., de Freitas, P.L., Feller, C.L., 2008. Texture and sesquioxide effects on water-stable aggregates and organic matter in some tropical soils. Geoderma 143, 14–25.
Beatty, S.M., Smith, J.E., 2010. Fractional wettability and contact angle dynamics in burned water repellent soils. Journal of Hydrology 391, 97–108.
Benito, E., Santiago, J.L., De Blas, E., Varela, M.E., 2003. Deforestation of water-repellent soils in Galicia (NW Spain): effects on surface runoff and erosion under simulated rainfall. Earth Surface Processes and Landforms: The Journal of the British Geomorphological Research Group 28, 145–155.
Bilardello D., Jackson, M., 2013. What do the mumpsies do? IRM Q 11–15.
Bisdom, E.B.A., Dekker, L.W., Schoute, J.F.T., 1993. Water repellency of sieve fractions from sandy soils and relationships with organic material and soil structure, in: Soil Structure/Soil Biota Interrelationships. Elsevier, pp. 105–118.
Boix-Fayos, C., Calvo-Cases, A., Imeson, A.C., Soriano-Soto, M.D., 2001. Influence of soil properties on the aggregation of some Mediterranean soils and the use of aggregate size and stability as land degradation indicators. Catena 44, 47–67.
Bonanomi, G., Idbella, M., Abd-ElGawad, A.M., Motti, R., Ippolito, F., Santorufo, L., Adamo, P., Agrelli, D., De Marco, A., Maisto, G., others, 2022. Impact of prescribed burning, mowing and abandonment on a Mediterranean grassland: A 5-year multi-kingdom comparison. Science of The Total Environment 834, 155442.
Bonifacio, E., Falsone, G., Piazza, S., 2010. Linking Ni and Cr concentrations to soil mineralogy: does it help to assess metal contamination when the natural background is high? Journal of Soils and Sediments 10, 1475–1486.
Bora, D.K., Braun, A., Erat, S., Safonova, O., Graule, T., Constable, E.C., 2012. Evolution of structural properties of iron oxide nano particles during temperature treatment from 250 C--900 C: X-ray diffraction and Fe K-shell pre-edge X-ray absorption study. Current applied physics 12, 817–825.
Borggaard, O.K., 1985. Organic matter and silicon in relation to the crystallinity of soil iron oxides. Acta Agriculturae Scandinavica 35, 398–406.
Bovio, G., 2011. Forest fires and systemic silviculture. L'Italia Forestale e Montana 66, 239–243.
Bowker, M.A., Belnap, J., Rosentreter, R., Graham, B., 2004. Wildfire-resistant biological soil crusts and fire-induced loss of soil stability in Palouse prairies, USA. Applied Soil Ecology 26, 41–52.
Bowman, D.M.J.S., Balch, J.K., Artaxo, P., Bond, W.J., Carlson, J.M., Cochrane, M.A., D'Antonio, C.M., DeFries, R.S., Doyle, J.C., Harrison, S.P., others, 2009. Fire in the Earth system. science 324, 481–484.

Brown, G., 1980. Associated minerals, in: Brindley, G. W. & Brown, G. (Eds.) Crystal structures of clay minerals and their X-ray identification. London Mineralogical Society, pp. 361–410.

Burton, E.D., Choppala, G., Karimian, N., Johnston, S.G., 2019. A new pathway for hexavalent chromium formation in soil: Fire-induced alteration of iron oxides. Environmental Pollution 247, 618–625.

Caballero, R., Fernandez-Gonzalez, F., Badia, R.P., Molle, G., Roggero, P.P., Bagella, S., Papanastasis, V.P., Fotiadis, G., Sidiropoulou, A., Ispikoudis, I., others, 2011. Grazing systems and biodiversity in Mediterranean areas: Spain, Italy and Greece. Pastos 39, 9–154.

Campbell, A.S., Schwertmann, U., 1984. Iron oxide mineralogy of placic horizons. Journal of Soil Science 35, 569–582.

Campo, J., Gimeno-García, E., Andreu, V., González-Pelayo, O., Rubio, J.L., 2008. Aggregation of under canopy and bare soils in a Mediterranean environment affected by different fire intensities. Catena 74, 212–218.

Capra, G.F., Tidu, S., Lovreglio, R., Certini, G., Salis, M., Bacciu, V., Ganga, A., Filzmoser, P., 2018. The impact of wildland fires on calcareous Mediterranean pedosystems (Sardinia, Italy)--An integrated multiple approach. Science of the total environment 624, 1152–1162.

Carter-Stiglitz, B., Moskowitz, B., Solheid, P., Berquo, T.S., Jackson, M., Kosterov, A., 2006. Low-temperature magnetic behavior of multidomain titanomagnetites: TM0. TM16, and TM35, J Geophys Res: Solid Earth 111.

Certini, G., 2005. Effects of fire on properties of forest soils: a review. Oecologia 143, 1–10.

Certini, G., Ugolini, F.C., 2010. BASI DI PEDOLOGIA. Cos'è il suolo, come si forma, come va descritto e classificato. Certini G., and FC Ugolini. Edagricole, Edizioni Agricole Il Sole 24 Ore, Bologna, pp. 196. ISBN 978-88-506-5286-0.

Chassé, A.W., Ohno, T., Higgins, S.R., Amirbahman, A., Yildirim, N., Parr, T.B., 2015. Chemical force spectroscopy evidence supporting the layer-by-layer model of organic matter binding to iron (oxy) hydroxide mineral surfaces. Environmental science & technology 49, 9733–9741.

Chenu, C., Le Bissonnais, Y., Arrouays, D., 2000. Organic matter influence on clay wettability and soil aggregate stability. Soil Science Society of America Journal 64, 1479–1486.

Chiappone, A., Marello, S., Scavia, C., Setti, M., 2004. Clay mineral characterization through the methylene blue test: comparison with other experimental techniques and applications of the method. Canadian Geotechnical Journal 41, 1168–1178.

Clement, B.M., Javier, J., Sah, J.P., Ross, M.S., 2011. The effects of wildfires on the magnetic properties of soils in the Everglades. Earth Surface Processes and Landforms 36, 460–466.

Coey, J.M.D., 1988. Magnetic properties of iron in soil iron oxides and clay minerals, in: Iron in Soils and Clay Minerals. Springer, pp. 397–466.

Cornell, R.M., Schwertmann, U., 2003. The iron oxides : structure, properties,

reactions, occurrences, and uses, second ed. Wiley-VCH, Weinheim.
Cudennec, Y., Lecerf, A., 2005. Topotactic transformations of goethite and lepidocrocite into hematite and maghemite. Solid State Sciences 7, 520–529.
D'Amico, M.E., Bonifacio, E., Zanini, E., 2014. Relationships between serpentine soils and vegetation in a xeric inner-Alpine environment. Plant and soil 376, 111–128.
de Blas, E., Rodríguez-Alleres, M., Almendros, G., 2010. Speciation of lipid and humic fractions in soils under pine and eucalyptus forest in northwest Spain and its effect on water repellency. Geoderma 155, 242–248.
De Faria, D.L.A., Venâncio Silva, S., De Oliveira, M.T., 1997. Raman microspectroscopy of some iron oxides and oxyhydroxides. Journal of Raman spectroscopy 28, 873–878.
De Grave, E., Barrero, C.A., Da Costa, G.M., Vandenberghe, R.E., Van San, E., 2002. Mössbauer spectra of α- and γ-polymorphs of FeOOH and Fe2O3 : effects of poor crystallinity and of Al-for-Fe substitution. Clay minerals 37, 591–606.
De Marco, A., Napoletano, P., Panico, S.C., Memoli, V., Santorufo, L., Ruggiero, A.G., Colombo, C., Barile, R., Maisto, G., 2023. Combined effect of black locust invasion and fire on soils of Mediterranean shrublands and pine forests. CATENA 220, 106656.
DeBano, L. F., 2000. The role of fire and soil heating on water repellency in wildland environments: a review. Journal of hydrology 231, 195–206.
DeBano, L F, 2000. Water repellency in soils: a historical overview. Journal of Hydrology 231, 4–32.
DeBano, L.F., 1991. The effect of fire on soil properties, in: Proceedings Management and Productivity of Western-Montane. Forest Soils. pp. 151–155.
DeBano, L.F., Neary, D.G., Ffolliott, P.F., 1998. Fire effects on ecosystems. John Wiley & Sons, New York.
DeLuca, T.H., Gundale, M.J., Brimmer, R.J., Gao, S., 2020. Pyrogenic carbon generation from fire and forest restoration treatments. Frontiers in Forests and Global Change 3, 24.
Diehl, D., 2013. Soil water repellency: Dynamics of heterogeneous surfaces. Colloids and Surfaces A: Physicochemical and Engineering Aspects 432, 8–18.
Diehl, D., Bayer, J. V, Woche, S.K., Bryant, R., Doerr, S.H., Schaumann, G.E., 2010. Reaction of soil water repellency to artificially induced changes in soil pH. Geoderma 158, 375–384.
Diehl, D., Schaumann, G.E., 2007. The nature of wetting on urban soil samples: wetting kinetics and evaporation assessed from sessile drop shape. Hydrological Processes: An International Journal 21, 2255–2265.
Dionísio, A., Braga, M.A.S., Waerenborgh, J.C., 2009. Clay minerals and iron oxides-oxyhydroxides as fingerprints of firing effects in a limestone monument. Applied Clay Science 42, 629–638.
Dixon, J.B., Weed, S.B., Parpitt, R.L., 1990. Minerals in soil environments. Soil

Science 150, 562.
Doerr, S.H., 1998. On standardizing the ‘water drop penetration time’and the ‘molarity of an ethanol droplet’techniques to classify soil hydrophobicity: a case study using medium textured soils. Earth Surface Processes and Landforms: The Journal of the British Geomorphological Group 23, 663–668.
Doerr, S.H., Llewellyn, C.T., Douglas, P., Morley, C.P., Mainwaring, K.A., Haskins, C., Johnsey, L., Ritsema, C.J., Stagnitti, F., Allinson, G., others, 2005. Extraction of compounds associated with water repellency in sandy soils of different origin. Soil Research 43, 225–237.
Doerr, S.H., Shakesby, R.A., Walsh, R.P.D., 2000. Soil water repellency : its causes, characteristics and hydro-geomorphological significance. Earth-Science Reviews 51, 33-65.
Doerr, S.H., Shakesby, R.A., Walsh, R.P.D., 1996. Soil hydrophobicity variations with depth and particle size fraction in burned and unburned Eucalyptus globulus and Pinus pinaster forest terrain in the Agueda Basin, Portugal. Catena 27, 25–47.
Dong, C., 1999. PowderX: Windows-95-based program for powder X-ray diffraction data processing. Journal of Applied Crystallography 32, 838.
Duval, J.F.L., Wilkinson, K.J., van Leeuwen, H.P., Buffle, J., 2005. Humic substances are soft and permeable: evidence from their electrophoretic mobilities. Environmental science & technology 39, 6435–6445.
Ellerbrock, R.H., Gerke, H.H., 2004. Characterizing organic matter of soil aggregate coatings and biopores by Fourier transform infrared spectroscopy. European Journal of Soil Science 55, 219–228.
Elmes, M.C., Thompson, D.K., Price, J.S., 2019. Changes to the hydrophysical properties of upland and riparian soils in a burned fen watershed in the Athabasca Oil Sands Region, northern Alberta, Canada. Catena 181, 104077.
Espinosa, A., Serrano, A., Llavona, A., De La Morena, J.J., Abuin, M., Figuerola, A., Pellegrino, T., Fernández, J.F., Garcia-Hernandez, M., Castro, G.R., Garcia, M.A., 2011. On the discrimination between magnetite and maghemite by XANES measurements in fluorescence mode. Measurement Science and Technology 23, 15602.
Evans, M., Heller, F., 2003. Environmental magnetism: principles and applications of enviromagnetics. Elsevier.
Falsone, G., Celi, L., Stanchi, S., Bonifacio, E., 2016. Relative importance of mineralogy and organic matter characteristics on macroaggregate and colloid dynamics in Mg-silicate dominated soils. Land Degradation & Development 27, 1700–1708.
Fedotov, G.N., Tret’yakov, Y.D., Dobrovol’skii, G. V, Putlyaev, V.I., Pakhomov, E.I., Fan’kovskaya, A.A., Pochatkova, T.N., 2006. Water resistance of soil aggregates and gel structures, in: Doklady Chemistry. pp. 215–218.
Fernández-García, V., Miesel, J., Baeza, M.J., Marcos, E., Calvo, L., 2019. Wildfire effects on soil properties in fire-prone pine ecosystems:

Indicators of burn severity legacy over the medium term after fire. Applied Soil Ecology 135, 147–156.
Ferreira, A.J.D., Coelho, C.O.A., Boulet, A.K., Leighton-Boyce, G., Keizer, J.J., Ritsema, C.J., 2005. Influence of burning intensity on water repellency and hydrological processes at forest and shrub sites in Portugal. Soil Research 43, 327–336.
Fox, D.M., Darboux, F., Carrega, P., 2007. Effects of fire-induced water repellency on soil aggregate stability, splash erosion, and saturated hydraulic conductivity for different size fractions. Hydrological Processes: An International Journal 21, 2377–2384.
García-Corona, R., Benito, E., De Blas, E., Varela, M.E., 2004. Effects of heating on some soil physical properties related to its hydrological behaviour in two north-western Spanish soils. International Journal of Wildland Fire 13, 195–199.
Gee, G.W., Bauder, J.W., 1986. Particle-size analysis. Methods of soil analysis: Part 1 Physical and mineralogical methods 5, 383–411.
Gee, G.W., Or, D., 2002. 2.4 Particle-size analysis. Methods of soil analysis: Part 4 physical methods 5, 255–293.
Giannetta, B., de Souza, D.O., Aquilanti, G., Celi, L., Said-Pullicino, D., 2022. Redox-driven changes in organic C stabilization and Fe mineral transformations in temperate hydromorphic soils. Geoderma 406, 115532.
Giannetta, B., Siebecker, M.G., Zaccone, C., Plaza, C., Rovira, P., Vischetti, C., Sparks, D.L., 2020. Iron (III) fate after complexation with soil organic matter in fine silt and clay fractions: An EXAFS spectroscopic approach. Soil and Tillage Research 200, 104617.
Gimeno-García, E., Andreu, V., Rubio, J.L., 2004. Spatial patterns of soil temperatures during experimental fires. Geoderma 118, 17–38.
Giovannini, G., Lucchesi, S., 1997. Modifications induced in soil physico-chemical parameters by experimental fires at different intensities. Soil Science 162, 479–486.
Giovannini, G., Lucchesi, S., Giachetti, M., 1988. Effect of heating on some physical and chemical parameters related to soil aggregation and erodibility. Soil Science 146, 255–261.
Girona-García, A., Ortiz-Perpiñá, O., Badía-Villas, D., Martí-Dalmau, C., 2018. Effects of prescribed burning on soil organic C, aggregate stability and water repellency in a subalpine shrubland: Variations among sieve fractions and depths. Catena 166, 68–77.
Glaser, B., Lehmann, J., Zech, W., 2002. Ameliorating physical and chemical properties of highly weathered soils in the tropics with charcoal--a review. Biology and fertility of soils 35, 219–230.
Glasspool, I.J., Scott, A.C., Waltham, D., Pronina, N.V., Shao, L., 2015. The impact of fire on the Late Paleozoic Earth system. Frontiers in Plant Science 6, 756.
González-Pérez, J.A., González-Vila, F.J., Almendros, G., Knicker, H., 2004. The effect of fire on soil organic matter—a review. Environment international 30, 855–870.

González-Pérez, J.A., González-Vila, F.J., González-Vázquez, R., Arias, M.E., Rodríguez, J., Knicker, H., 2008. Use of multiple biogeochemical parameters to monitor the recovery of soils after forest fires. Organic Geochemistry 39, 940–944.

Graber, E.R., Tagger, S., Wallach, R., 2009. Role of divalent fatty acid salts in soil water repellency. Soil Science Society of America Journal 73, 541–549.

Greene, D.F., Hesketh, M., Pounden, E., 2010. Emergence of morel (Morchella) and pixie cup (Geopyxis carbonaria) ascocarps in response to the intensity of forest floor combustion during a wildfire. Mycologia 102, 766–773.

Gualtieri, A.F., Venturelli, P., 1999. In situ study of the goethite-hematite phase transformation by real time synchrotron powder diffraction. American Mineralogist 84, 895–904.

Guerrero, C., Mataix-Solera, J., Navarro-Pedreño, J., García-Orenes, F., Gómez, I., 2001. Different patterns of aggregate stability in burned and restored soils. Arid Land Research and Management 15, 163–171.

Hall, S.J., Berhe, A.A., Thompson, A., 2018. Order from disorder: do soil organic matter composition and turnover co-vary with iron phase crystallinity? Biogeochemistry 140, 93–110.

Harper, R.J., McKissock, I., Gilkes, R.J., Carter, D.J., Blackwell, P.S., 2000. A multivariate framework for interpreting the effects of soil properties, soil management and landuse on water repellency. Journal of Hydrology 231, 371–383.

Hartford, R.A., Frandsen, W.H., 1992. When it's hot, it's hot... or maybe it's not!(Surface flaming may not portend extensive soil heating). International Journal of Wildland Fire 2, 139–144.

Hilscher, A., Heister, K., Siewert, C., Knicker, H., 2009. Mineralisation and structural changes during the initial phase of microbial degradation of pyrogenic plant residues in soil. Organic Geochemistry 40, 332–342.

Humphreys, F.R., 1981. Effects of fire on soil chemical, structural and hydrological properties. Fire and Australian Biota.

Hyeon, T., Lee, S.S., Park, J., Chung, Y., Na, H. Bin, 2001. Synthesis of highly crystalline and monodisperse maghemite nanocrystallites without a size-selection process. Journal of the American Chemical Society 123, 12798–12801.

IPLA, 2001. Piano Forestale Territoriale. Area forestale: Val Chisone e Germanasca. Regione Piemonte.

IPLA, 2000. Piano Forestale Territoriale. Area forestale: Alta Valle Susa. Regione Piemonte.

IUSS Working Group WRB, 2014. World reference base for soil resources, 2014. International soil classification system for naming soils and creating legends for soil maps. FAO. World Soil Resources Reports No, Rome, p. 106.

Jackson, M., Solheid, P., 2010. On the quantitative analysis and evaluation of magnetic hysteresis data. Geochemistry, Geophysics, Geosystems 11.

Jambor, J.L., Dutrizac, J.E., 1998. Occurrence and constitution of natural and

synthetic ferrihydrite, a widespread iron oxyhydroxide. Chemical reviews 98, 2549–2586.
Janzen, C., Tobin-Janzen, T., 2008. Microbial communities in fire-affected soils, in: Microbiology of Extreme Soils. Springer, pp. 299–316.
Jeleńska, M., Hasso-Agopsowicz, A., Kopcewicz, B., 2010. Thermally induced transformation of magnetic minerals in soil based on rock magnetic study and Mössbauer analysis. Physics of the Earth and Planetary Interiors 179, 164–177.
Jiménez-Morillo, N.T., González-Pérez, J.A., Jordán, A., Zavala, L.M., de la Rosa, J.M., Jiménez-González, M.A., González-Vila, F.J., 2016. Organic matter fractions controlling soil water repellency in sandy soils from the Doñana National Park (Southwestern Spain). Land Degradation \& Development 27, 1413–1423.
Johnson, D.W., Curtis, P.S., 2001. Effects of forest management on soil C and N storage: meta analysis. Forest ecology and management 140, 227–238.
Johnston, S.G., Bennett, W.W., Burton, E.D., Hockmann, K., Dawson, N., Karimian, N., 2018. Rapid arsenic (V)-reduction by fire in schwertmannite-rich soil enhances arsenic mobilisation. Geochimica et Cosmochimica Acta 227, 1–18.
Johnston, S.G., Karimian, N., Burton, E.D., 2019. Fire promotes arsenic mobilization and rapid arsenic (III) formation in soil via thermal alteration of arsenic-bearing iron oxides. Frontiers in Earth Science 7, 139.
Jolly, W.M., Cochrane, M.A., Freeborn, P.H., Holden, Z.A., Brown, T.J., Williamson, G.J., Bowman, D.M.J.S., 2015. Climate-induced variations in global wildfire danger from 1979 to 2013. Nature communications 6, 1–11.
Jordán, A., Zavala, L.M., Mataix-Solera, J., Nava, A.L., Alanís, N., 2011. Effect of fire severity on water repellency and aggregate stability on Mexican volcanic soils. Catena 84, 136–147.
Jordanova, N., Jordanova, D., Barrón, V., 2019. Wildfire severity: Environmental effects revealed by soil magnetic properties. Land Degradation & Development 30, 2226–2242.
Jozwiak, W.K., Kaczmarek, E., Maniecki, T.P., Ignaczak, W., Maniukiewicz, W., 2007. Reduction behavior of iron oxides in hydrogen and carbon monoxide atmospheres. Applied Catalysis A: General 326, 17–27.
Kaiser, K., Guggenberger, G., 2007. Sorptive stabilization of organic matter by microporous goethite: sorption into small pores vs. surface complexation. European Journal of Soil Science 58, 45–59.
Kaiser, K., Guggenberger, G., 2003. Mineral surfaces and soil organic matter. European Journal of Soil Science 54, 219–236.
Kavdır, Y., Ekinci, H., Yüksel, O., Mermut, A.R., 2005. Soil aggregate stability and 13C CP/MAS-NMR assessment of organic matter in soils influenced by forest wildfires in Canakkale, Turkey. Geoderma 129, 219–229.
Kawai, J., 2010. Chapter 5 - Application of Extended X-Ray Emission Fine Structure Spectroscopy in Soil and Sediments, in: Singh, B., Gräfe, M. (Eds.), Synchrotron-Based Techniques in Soils and Sediments,

Developments in Soil Science. Elsevier, pp. 131–146. https://doi.org/https://doi.org/10.1016/S0166-2481(10)34005-0
Keeley, J.E., Bond, W.J., Bradstock, R.A., Pausas, J.G., Rundel, P.W., 2011. Fire in Mediterranean ecosystems: ecology, evolution and management. Cambridge University Press.
Keesstra, S., Wittenberg, L., Maroulis, J., Sambalino, F., Malkinson, D., Cerdà, A., Pereira, P., 2017. The influence of fire history, plant species and post-fire management on soil water repellency in a Mediterranean catchment: the Mount Carmel range, Israel. Catena 149, 857–866.
Kemper, W.D., Koch, E.J., 1966. Aggregate stability of soils from Western United States and Canada: Measurement procedure, correlations with soil constituents. Agricultural Research Service, US Department of Agriculture.
Kipfer, T., Moser, B., Egli, S., Wohlgemuth, T., Ghazoul, J., 2011. Ectomycorrhiza succession patterns in Pinus sylvestris forests after stand-replacing fire in the Central Alps. Oecologia 167, 219–228.
Knicker, H., 2011. Pyrogenic organic matter in soil: Its origin and occurrence, its chemistry and survival in soil environments. Quaternary International 243, 251–263.
Knicker, H., 2007. How does fire affect the nature and stability of soil organic nitrogen and carbon? A review. Biogeochemistry 85, 91–118.
Knicker, H., Almendros, G., González-Vila, F.J., González-Pérez, J.A., Polvillo, O., 2006. Characteristic alterations of quantity and quality of soil organic matter caused by forest fires in continental Mediterranean ecosystems: a solid-state 13C NMR study. European Journal of Soil Science 57, 558–569.
Knicker, H., Hilscher, A., González-Vila, F.J., Almendros, G., 2008. A new conceptual model for the structural properties of char produced during vegetation fires. Organic Geochemistry 39, 935–939.
Koch, C.B., Borggaard, O.K., Gafur, A., 2005. Formation of iron oxides in soils developed under natural fires and slash-and-burn based agriculture in a monsoonal climate (Chittagong Hill Tracts, Bangladesh). Hyperfine interactions 166, 579–584.
Kögel-Knabner, I., Guggenberger, G., Kleber, M., Kandeler, E., Kalbitz, K., Scheu, S., Eusterhues, K., Leinweber, P., 2008. Organo-mineral associations in temperate soils: Integrating biology, mineralogy, and organic matter chemistry. Journal of Plant Nutrition and Soil Science 171, 61–82.
Komac, B., Kéfi, S., Nuche, P., Escós, J., Alados, C.L., 2013. Modeling shrub encroachment in subalpine grasslands under different environmental and management scenarios. Journal of Environmental Management 121, 160–169.
Kottek, M., Grieser, J., Beck, C., Rudolf, B., Rubel, F., 2006. World map of the Köppen-Geiger climate classification updated.
LaGrow, A.P., Besenhard, M.O., Hodzic, A., Sergides, A., Bogart, L.K., Gavriilidis, A., Thanh, N.T.K., 2019. Unravelling the growth mechanism

of the co-precipitation of iron oxide nanoparticles with the aid of synchrotron X-Ray diffraction in solution. Nanoscale 11, 6620–6628.
Lanzl, C.A., Baltrusaitis, J., Cwiertny, D.M., 2012. Dissolution of hematite nanoparticle aggregates: influence of primary particle size, dissolution mechanism, and solution pH. Langmuir 28, 15797–15808.
Legros, J.P., 1992. Soils of Alpine mountains, in: Developments in Earth Surface Processes. Elsevier, pp. 155–181.
Letey, J., 1969. Measurement of contact angle, water drop penetration time, and critical surface tension. Proceedings of the Symposium on Water-Repellent Soils 43–47.
Liu, Q., Roberts, A.P., Larrasoaña, J.C., Banerjee, S.K., Guyodo, Y., Tauxe, L., Oldfield, F., 2012. Environmental magnetism: principles and applications. Reviews of Geophysics 50.
Liu, W-J., Li, W-W., Jiang, H., Yu, H-Q., 2017. Fates of chemical elements in biomass during its pyrolysis. Chemical Reviews 117, 6367–6398.
Llovet, J., Ruiz-Valera, M., Josa, R., Vallejo, V.R., 2009. Soil responses to fire in Mediterranean forest landscapes in relation to the previous stage of land abandonment. International Journal of Wildland Fire 18, 222–232.
Loeppert R.H., I.W.P., 1996. Iron - Methods of soil analysis, part 3: Chemical methods. Madison, WI, USA.
Löhr, S.C., Murphy, D.T., Nothdurft, L.D., Bolhar, R., Piazolo, S., Siegel, C., 2017. Maghemite soil nodules reveal the impact of fire on mineralogical and geochemical differentiation at the Earth's surface. Geochimica et Cosmochimica Acta 200, 25–41.
Lozano, E., Jiménez-Pinilla, P., Mataix-Solera, J., Arcenegui, V., Bárcenas, G.M., González-Pérez, J.A., García-Orenes, F., Torres, M.P., Mataix-Beneyto, J., 2013. Biological and chemical factors controlling the patchy distribution of soil water repellency among plant species in a Mediterranean semiarid forest. Geoderma 207, 212–220.
Maffei, M., Badino, S., Bossi, S., others, 2004. Chemotaxonomic significance of leaf wax n-alkanes in the Pinales (Coniferales). J Biol Res 1, 3–19.
Malkinson, D., Wittenberg, L., 2011. Geomorphology Post fi re induced soil water repellency — Modeling short and long-term processes. Geomorphology 125, 186–192. https://doi.org/10.1016/j.geomorph.2010.09.014
Mantero, G., Morresi, D., Marzano, R., Motta, R., Mladenoff, D.J., Garbarino, M., 2020. The influence of land abandonment on forest disturbance regimes: a global review. Landscape Ecology 35, 2723–2744.
Mao, J., Nierop, K.G.J., Damsté, J.S.S., Dekker, S.C., 2014. Roots induce stronger soil water repellency than leaf waxes. Geoderma 232, 328–340.
Martínez, C.E., Bazilevskaya, K.A., Lanzirotti, A., 2006. Zinc coordination to multiple ligand atoms in organic-rich surface soils. Environmental science \& technology 40, 5688–5695.
Mastrolonardo, G., Certini, G., Krebs, R., Forte, C., Egli, M., 2013. Effects of fire on soil organic matter quality along an altitudinal sequence on Mt. Etna, Sicily. Catena 110, 133–145.

Mastrolonardo, G., Francioso, O., Di Foggia, M., Bonora, S., Rumpel, C., Certini, G., 2014. Application of thermal and spectroscopic techniques to assess fire-induced changes to soil organic matter in a Mediterranean forest. Journal of Geochemical Exploration 143, 174–182.

Mastrolonardo, G., Rumpel, C., Forte, C., Doerr, S.H., Certini, G., 2015. Abundance and composition of free and aggregate-occluded carbohydrates and lignin in two forest soils as affected by wildfires of different severity. Geoderma 245, 40–51.

Mataix-Solera, J., Arcenegui, V., Guerrero, C., Jordán, M.M., Dlapa, P., Tessler, N., Wittenberg, L., 2008. Can terra rossa become water repellent by burning? A laboratory approach. Geoderma 147, 178–184.

Mataix-Solera, J., Cerdà, A., 2009. 1.1Incendios forestales en España. Ecosistemas terrestres y suelos. Efectos de los incendios forestales sobre los suelos en España, 25-53.

Mataix-Solera, J., Cerdà, A., Arcenegui, V., Jordán, A., Zavala, L.M., 2011. Fire effects on soil aggregation: a review. Earth-Science Reviews 109, 44–60.

Mataix-Solera, J., Doerr, S.H., 2004. Hydrophobicity and aggregate stability in calcareous topsoils from fire-affected pine forests in southeastern Spain. Geoderma 118, 77–88.

Mataix-Solera, J., Gómez, I., Navarro-Pedreño, J., Guerrero, C., Moral, R., 2002. Soil organic matter and aggregates affected by wildfire in a Pinus halepensis forest in a Mediterranean environment. International Journal of Wildland Fire 11, 107–114.

Mayer, L.M., Xing, B., 2001. Organic matter--surface area relationships in acid soils. Soil Science Society of America Journal 65, 250–258.

Mehra, O.P., Jackson, M.L., 1958. Iron oxide removal from soils and clays by a dithionite--citrate system buffered with sodium bicarbonate, in: Clays and Clay Minerals. Elsevier, pp. 317–327.

Merino, A., Chávez-Vergara, B., Salgado, J., Fonturbel, M.T., García-Oliva, F., Vega, J.A., 2015. Variability in the composition of charred litter generated by wildfire in different ecosystems. Catena 133, 52–63.

Merino, A., Fonturbel, M.T., Fernández, C., Chávez-Vergara, B., García-Oliva, F., Vega, J.A., 2018. Inferring changes in soil organic matter in post-wildfire soil burn severity levels in a temperate climate. Science of the Total Environment 627, 622–632.

Mobilio, S., 2015. Introduction to Matter Radiation Interaction, in: Synchrotron Radiation. Springer, pp. 107–143.

Moody, J.A., Shakesby, R.A., Robichaud, P.R., Cannon, S.H., Martin, D.A., 2013. Current research issues related to post-wildfire runoff and erosion processes. Earth-Science Reviews 122, 10–37.

Moore, D.M., Reynolds Jr., R.C., 1989. X-Ray Diffraction and the Identification and Analysis of Clay Minerals 400.

Murphy, E.M., Zachara, J.M., Smith, S.C., 1990. Influence of mineral-bound humic substances on the sorption of hydrophobic organic compounds. Environmental Science & Technology 24, 1507–1516.

Neary, D.G., Klopatek, C.C., DeBano, L.F., Ffolliott, P.F., 1999. Fire effects on belowground sustainability: a review and synthesis. Forest ecology and management 122, 51–71.

Negri, S., Stanchi, S., Celi, L., Bonifacio, E., 2021. Simulating wildfires with lab-heating experiments: Drivers and mechanisms of water repellency in alpine soils. Geoderma 402, 115357.

Nelson, R.E., 1982. Carbonate and gypsum. Methods of soil analysis 181–198.

Newcomb, C.J., Qafoku, N.P., Grate, J.W., Bailey, V.L., De Yoreo, J.J., 2017. Developing a molecular picture of soil organic matter--mineral interactions by quantifying organo--mineral binding. Nature communications 8, 1–8.

Nocentini, C., Certini, G., Knicker, H., Francioso, O., Rumpel, C., 2010. Nature and reactivity of charcoal produced and added to soil during wildfire are particle-size dependent. Organic Geochemistry 41, 682–689.

Norouzi, M., Ramezanpour, H., 2013. Effect of fire on chemical forms of iron and manganese in forest soils of Iran. Environmental Forensics 14, 169–177.

O'Day, P.A., Rivera Jr, N., Root, R., Carroll, S.A., 2004. X-ray absorption spectroscopic study of Fe reference compounds for the analysis of natural sediments. American Mineralogist 89, 572–585.

O'dea, M.E., 2007. Fungal mitigation of soil erosion following burning in a semi-arid Arizona savanna. Geoderma 138, 79–85.

Ohno, T., Heckman, K.A., Plante, A.F., Fernandez, I.J., Parr, T.B., 2017. 14C mean residence time and its relationship with thermal stability and molecular composition of soil organic matter: A case study of deciduous and coniferous forest types. Geoderma 308, 1–8.

Oldfield, F., Crowther, J., 2007. Establishing fire incidence in temperate soils using magnetic measurements. Palaeogeography, Palaeoclimatology, Palaeoecology 249, 362–369.

Orumaa, A., Agan, A., Anslan, S., Drenkhan, T., Drenkhan, R., Kauer, K., Köster, K., Tedersoo, L., Metslaid, M., 2022. Long-term effects of forest fires on fungal community and soil properties along a hemiboreal Scots pine forest fire chronosequence. Science of The Total Environment 851, 158173.

Oudou, H.C., Hansen, H.C.B., 2002. Sorption of lambda-cyhalothrin, cypermethrin, deltamethrin and fenvalerate to quartz, corundum, kaolinite and montmorillonite. Chemosphere 49, 1285–1294.

Oze, C., Fendorf, S., Bird, D.K., Coleman, R.G., 2004. Chromium geochemistry of serpentine soils. International Geology Review 46, 97–126.

Pachauri, R.K., Meyer, L.A., 2014. Climate Change 2014: Synthesis Report. Contribution of Working Groups I, II and III to the Fifth Assessment Report of the Intergovernmental Panel on Climate Change.

Papierowska, E., Matysiak, W., Szatyłowicz, J., Debaene, G., Urbanek, E., Kalisz, B., Łachacz, A., 2018. Compatibility of methods used for soil water repellency determination for organic and organo-mineral soils. Geoderma 314, 221–231.

Parker, S.D., 1987. Encyclopedia of Science and Technology. McGraw-Hill, New York.
Pellegrini, A.F.A., Harden, J., Georgiou, K., Hemes, K.S., Malhotra, A., Nolan, C.J., Jackson, R.B., 2022. Fire effects on the persistence of soil organic matter and long-term carbon storage. Nature Geoscience 15, 5–13.
Penn, R.L., Erbs, J.J., Gulliver, D.M., 2006. Controlled growth of alpha-FeOOH nanorods by exploiting-oriented aggregation. Journal of Crystal Growth 293, 1–4.
Peuravuori, J., Pihlaja, K., 1997. Molecular size distribution and spectroscopic properties of aquatic humic substances. Analytica Chimica Acta 337, 133–149.
Pickett, S.T.A., White, P.S., 2013. The ecology of natural disturbance and patch dynamics. Elsevier.
Porta Casanellas, J., López-Acevedo Reguerín, M., de Laburu, C., 1994. Edafología para la agricultura y el medio ambiente.
Ravel, B., Newville, M., 2005. ATHENA, ARTEMIS, HEPHAESTUS: data analysis for X-ray absorption spectroscopy using IFEFFIT. Journal of synchrotron radiation 12, 537–541.
Redl, F.X., Black, C.T., Papaefthymiou, G.C., Sandstrom, R.L., Yin, M., Zeng, H., Murray, C.B., O'Brien, S.P., 2004. Magnetic, electronic, and structural characterization of nonstoichiometric iron oxides at the nanoscale. Journal of the American Chemical Society 126, 14583–14599.
Reynard-Callanan, J.R., Pope, G.A., Gorring, M.L., Feng, H., 2010. Effects of high-intensity forest fires on soil clay mineralogy. Physical Geography 31, 407–422.
Rietveld, H.M., 1969. A profile refinement method for nuclear and magnetic structures. Journal of applied Crystallography 2, 65–71.
Rita, A., Camarero, J.J., Nolè, A., Borghetti, M., Brunetti, M., Pergola, N., Serio, C., Vicente-Serrano, S.M., Tramutoli, V., Ripullone, F., 2020. The impact of drought spells on forests depends on site conditions: The case of 2017 summer heat wave in southern Europe. Global change biology 26, 851–863.
Robichaud, P.R., 2000. Fire effects on infiltration rates after prescribed fire in Northern Rocky Mountain forests, USA. Journal of Hydrology 231, 220–229.
Roldán, A., Albaladejo, J., Thornes, J.B., 1996. Aggregate stability changes in a semiarid soil after treatment with different organic amendments. Arid Land Research and Management 10, 139–148.
Rooksby, H.P., 1972. Oxides and hydroxides of aluminum and iron. The x-ray identification and crystal structures of clay minerals.
Santín, C., Doerr, S.H., 2016. Fire effects on soils: the human dimension. Philosophical Transactions of the Royal Society B: Biological Sciences 371, 20150171.
Santín, C., Doerr, S.H., Kane, E.S., Masiello, C.A., Ohlson, M., de la Rosa, J.M., Preston, C.M., Dittmar, T., 2016. Towards a global assessment of pyrogenic carbon from vegetation fires. Global Change Biology 22, 76–

91.
Santos, F., Russell, D., Berhe, A.A., 2016. Thermal alteration of water extractable organic matter in climosequence soils from the Sierra Nevada, California. Journal of Geophysical Research: Biogeosciences 121, 2877–2885.
Sayed, F.N., Polshettiwar, V., 2015. Facile and sustainable synthesis of shaped iron oxide nanoparticles: effect of iron precursor salts on the shapes of iron oxides. Scientific reports 5, 1–14.
Schmidt, M.W.I., Torn, M.S., Abiven, S., Dittmar, T., Guggenberger, G., Janssens, I.A., Kleber, M., Kögel-Knabner, I., Lehmann, J., Manning, D.A.C., Nannipieri, P., Rasse, D.P., Weiner, S., Trumbore, S.E., 2011. Persistence of soil organic matter as an ecosystem property. Nature 478, 49–56.
Schwertmann, U., 1988. Occurrence and formation of iron oxides in various pedoenvironments, in: Iron in Soils and Clay Minerals. Springer, pp. 267–308.
Schwertmann, U., 1964. Differenzierung der Eisenoxide des Bodens durch photochemische Extraktion mit saurer Ammoniumoxalat-Lösung. Zeischrift für Pflanzenernährung, Düngung und Bodenkunde 105–194.
Schwertmann, U., Fechter, H., 1984. The influence of aluminum on iron oxides: XI. Aluminum-substituted maghemite in soils and its formation. Soil Science Society of America Journal 48, 1462–1463.
Scott, D.F., 2000. Soil wettability in forested catchments in South Africa; as measured by different methods and as affected by vegetation cover and soil characteristics. Journal of Hydrology 231, 87–104.
Seaton, F.M., Jones, D.L., Creer, S., George, P.B.L., Smart, S.M., Lebron, I., Barrett, G., Emmett, B.A., Robinson, D.A., 2019. Plant and soil communities are associated with the response of soil water repellency to environmental stress. Science of the total environment 687, 929–938.
Servizio Geologico d'Italia, 2009. Carta geologica d'Italia 1:50000. ISPRA e ARPA Piemonte, Direzione Regionale Servizi Tecnici e di Prevenzione.
Shakesby, R.A., Doerr, S.H., 2006. Wildfire as a hydrological and geomorphological agent. Earth-Science Reviews 74, 269–307.
Sharma, R.K., Wooten, J.B., Baliga, V.L., Lin, X., Chan, W.G., Hajaligol, M.R., 2004. Characterization of chars from pyrolysis of lignin. Fuel 83, 1469–1482.
Simkovic, I., Dlapa, P., Doerr, S.H., Mataix-Solera, J., Sasinkova, V., 2008. Thermal destruction of soil water repellency and associated changes to soil organic matter as observed by FTIR spectroscopy. Catena 74, 205–211.
Singh, N., Abiven, S., Maestrini, B., Bird, J.A., Torn, M.S., Schmidt, M.W.I., 2014. Transformation and stabilization of pyrogenic organic matter in a temperate forest field experiment. Global Change Biology 20, 1629–1642.
Six, J., Feller, C., Denef, K., Ogle, S., de Moraes Sa, J.C., Albrecht, A., 2002. Soil organic matter, biota and aggregation in temperate and tropical soils-Effects of no-tillage. Agronomie 22, 755–775.
Smith, H.G., Sheridan, G.J., Lane, P.N.J., Nyman, P., Haydon, S., 2011.

Wildfire effects on water quality in forest catchments: A review with implications for water supply. Journal of Hydrology 396, 170–192.
Socrates, G., 2004. Infrared and Raman characteristic group frequencies: tables and charts. John Wiley & Sons.
Šolc, R., Gerzabek, M.H., Lischka, H., Tunega, D., 2011. Wettability of kaolinite (001) surfaces—molecular dynamic study. Geoderma 169, 47–54.
Soil Survey Staff, 1999. Soil taxonomy: A basic system of soil classification for making and interpreting soil surveys. 2nd edition. Natural Resources Conservation Service US Department of Agriculture Handbook 436.
Soil Survey Staff, 2014. Kellogg Soil Survey Laboratory Methods Manual. Soil Survey Investigations Report No. 42, Version 5.0. R. Burt and Soil Survey Staff (Ed.). U.S. Department of Agriculture, Natural Resources Conservation Service.
Soto, B., Benito, E., Diaz-Fierros, F., 1991. Heat-induced degradation processes in forest soils. International Journal of Wildland Fire 1, 147–152.
Strydom, T., Riddell, E.S., Rowe, T., Govender, N., Lorentz, S.A., le Roux, P.A.L., Wigley-Coetsee, C., 2019. The effect of experimental fires on soil hydrology and nutrients in an African savanna. Geoderma 345, 114–122.
Teramura, A.H., 1980. Relationships between stand age and water repellency of chaparral soils. Bulletin of the Torrey Botanical Club 42–46.
Terashima, M., Fukushima, M., Tanaka, S., 2004. Influence of pH on the surface activity of humic acid: micelle-like aggregate formation and interfacial adsorption. Colloids and Surfaces A: Physicochemical and Engineering Aspects 247, 77–83.
Terefe, T., Mariscal-Sancho, I., Peregrina, F., Espejo, R., 2008. Influence of heating on various properties of six Mediterranean soils. A laboratory study. Geoderma 143, 273–280.
Thomaz, E.L., 2021. Effects of fire on the aggregate stability of clayey soils: A meta-analysis. Earth-Science Reviews 221, 103802.
Tiberg, F., Brinck, J., Grant, L., 1999. Adsorption and surface-induced self-assembly of surfactants at the solid--aqueous interface. Current opinion in colloid & interface science 4, 411–419.
Till, J.L., Jackson, M.J., Moskowitz, B.M., 2010. Remanence stability and magnetic fabric development in synthetic shear zones deformed at 500 C. Geochemistry, Geophysics, Geosystems 11.
Till, J.L., Moskowitz, B., Poulton, S.W., 2021. Magnetic properties of plant ashes and their influence on magnetic signatures of fire in soils. Frontiers in Earth Science 8.
Till, J.L., Nowaczyk, N., 2018. Authigenic magnetite formation from goethite and hematite and chemical remanent magnetization acquisition. Geophysical Journal International 213, 1818–1831.
Tinebra, I., Alagna, V., Iovino, M., Bagarello, V., 2019. Comparing different application procedures of the water drop penetration time test to assess soil water repellency in a fire affected Sicilian area. Catena 177, 41–48.
Tisdall, J.M., Oades, J.M., 1982. Organic matter and water-stable aggregates in

soils. Journal of soil science 33, 141–163.
Treseder, K.K., Maltz, M.R., Hawkins, B.A., Fierer, N., Stajich, J.E., McGuire, K.L., 2014. Evolutionary histories of soil fungi are reflected in their large-scale biogeography. Ecology Letters 17, 1086–1093.
Ubeda, X., Bernia, S., 2005. The effect of wildfire intensity on soil aggregate stability in the Cadiretes Massif, NE Spain. IAHS PUBLICATION 299, 37.
Uddin, S.M., Daniel, N.R.R., Harper, R.J., Henry, D.J., 2017. Why do biogenic volatile organic compounds (BVOCs) derived from vegetation fire not induce soil water repellency? Biogeochemistry 134, 147–161.
Ulery, A.L., Graham, R.C., Bowen, L.H., 1996. Forest fire effects on soil phyllosilicates in California. Soil Science Society of America Journal 60, 309–315.
Vacchiano, G., Stanchi, S., Marinari, G., Ascoli, D., Zanini, E., Motta, R., 2014. Fire severity, residuals and soil legacies affect regeneration of Scots pine in the Southern Alps. Science of the total environment 472, 778–788.
van Lierop, P., Lindquist, E., Sathyapala, S., Franceschini, G., 2015. Global forest area disturbance from fire, insect pests, diseases and severe weather events. Forest Ecology and Management 352, 78–88.
Varela, M.E., Benito, E., Keizer, J.J., 2010. Effects of wildfire and laboratory heating on soil aggregate stability of pine forests in Galicia: The role of lithology, soil organic matter content and water repellency. Catena 83, 127–134.
Vega, J.A., Fernandez, C., Fonturbel, T., Gonzalez-Prieto, S., Jimenez, E., 2014. Testing the effects of straw mulching and herb seeding on soil erosion after fire in a gorse shrubland. Geoderma 223, 79–87.
Vindedahl, A.M., Strehlau, J.H., Arnold, W.A., Penn, R.L., 2016. Organic matter and iron oxide nanoparticles: aggregation, interactions, and reactivity. Environmental Science: Nano 3, 494–505.
Vogelmann, E.S., Reichert, J.M., Reinert, D.J., Mentges, M.I., Vieira, D.A., de Barros, C.A.P., Fasinmirin, J.T., 2010. Water repellency in soils of humid subtropical climate of Rio Grande do Sul, Brazil. Soil and Tillage research 110, 126–133.
Wandruszka, R. von, Engebreatson, R.R., Yates III, L.M., others, 1999. Humic acid pseudomicelles in dilute aqueous solution: fluorescence and surface tension measurements. Understanding humic substances Advanced methods, properties and applications 79–85.
Weishaar, J.L., Aiken, G.R., Bergamaschi, B.A., Fram, M.S., Fujii, R., Mopper, K., 2003. Evaluation of specific ultraviolet absorbance as an indicator of the chemical composition and reactivity of dissolved organic carbon. Environmental science \& technology 37, 4702–4708.
Whittaker, E.J.W., Zussman, J., 1956. The characterization of serpentine minerals by X-ray diffraction. Mineralogical magazine and journal of the Mineralogical Society 31, 107–126.
Wilson, M.J., 2004. Weathering of the primary rock-forming minerals: processes, products and rates. Clay Minerals 39, 233–266.

Yang, F., Zhao, L., Gao, B., Xu, X., Cao, X., 2016. The interfacial behavior between biochar and soil minerals and its effect on biochar stability. Environmental science \& technology 50, 2264–2271.

Yoder, R.E., 1936. A direct method of aggregate analysis of soils and a study of the physical nature of erosion losses.

Zavala, L.M., García-Moreno, J., Gordillo-Rivero, Á.J., Jordán, A., Mataix-Solera, J., 2014. Natural soil water repellency in different types of Mediterranean woodlands. Geoderma 226, 170–178.

Zavala, L.M., Granged, A.J.P., Jordán, A., Bárcenas-Moreno, G., 2010. Effect of burning temperature on water repellency and aggregate stability in forest soils under laboratory conditions. Geoderma 158, 366–374.

Zema, D.A., Plaza-Alvarez, P.A., Xu, X., Carra, B.G., Lucas-Borja, M.E., 2021. Influence of forest stand age on soil water repellency and hydraulic conductivity in the Mediterranean environment. Science of the Total Environment 753, 142006.

Zhang, Y., Biswas, A., 2017. The effects of forest fire on soil organic matter and nutrients in boreal forests of North America: a review. Adaptive soil management: From theory to practices 465–476.

Zheng, W., Morris, E.K., Lehmann, A., Rillig, M.C., 2016. Interplay of soil water repellency, soil aggregation and organic carbon. A meta-analysis. Geoderma 283, 39–47.

AWKNOLEDGMENTS

I would like to thank all the people who contributed to the development of the present work.

Chapter 2:

Prof. Luisella Celi (University of Torino), Prof. Silvia Stanchi (University of Torino), Prof. Eleonora Bonifacio (University of Torino). I also thank Sara Trevisani, Msc student, for having performed part of the analyses. The research was funded by the University of Torino *Fondo di ricerca locale 2019*.

Chapter 3:

Dr. Beatrice Giannetta (University of Verona), Dr. Jessica Till (Institute for Rock Magnetism, Minneapolis), Dr. Danilo Oliveira de Souza (Elettra Sincrotrone Trieste), Prof. Daniel Said-Pullicino (University of Torino), Prof. Eleonora Bonifacio (University of Torino). I also thank Maria Carmen Valsania (University of Torino) for having given support and guidance during the microscopy analyses, and acknowledge ELETTRA Sincrotrone Trieste for the provision of synchrotron radiation facilities. I thank Giuliana Aquilanti and Luca Olivi (ELETTRA, XAFS beamline) for their support during the synchrotron measurements. This work was funded by the University of Torino in the framework of the project *Alterations of soil physico-chemical properties as a consequence of forest fires* (UNITO S1921 EX-POST).

Chapter 4:

Prof. Victoria Arcenegui (Universidad Miguel Hernández de Elche), Dr. Beatrice Giannetta (University of Verona), Dr. Nicasio T. Jiménez-Morillo (Universidade de Évora), Prof. Claudio Zaccone (University of Verona), Prof. Jorge Mataix-Solera (Universidad Miguel Hernández de Elche), Prof. Eleonora Bonifacio (University of Torino). I thank Ana Perez Ginemo for assistance during AAS measurements and Annapaola Giordano for guidance during HF acid attack procedure and determination of total element concentration with ICP-OES. I would also thank Débora Rodrigues Rocha and Yasmin Tadeu Costa for having supplied the two samples from Brazil.

I sincerely thank the reviewers, Giacomo Certini and Jorge Mataix-Solera, whose papers and books I have been reading for so long before having the chance to meet them in person.

I sincerely thank Eleonora Bonifacio, my academic tutor, for her personal involvement in all the aspects of my research activity. She has always pushed me to think, and think twice, on all that mattered.

I would extend my gratitude to all my colleagues and friends at the lab and at the department, also those people who no longer work here. I am thankful for all the experiences I had the opportunity to undertake, in Italy and abroad, including the Stirling contest with my fellow companions.

At last, I thank my family, my mum and dad, Hervé, and my friends. You were always curious about what I do, and gave me strength and hope when I needed it most.

For this journey has to end, but a new adventure begins.